SF 298 MASTER COPY KEEP THIS COPY FOR REPRODUCTION PURPOSES

REPORT DOCUMENTATION PAGE

Form Approved OMB NO. 0704-0188

1. AGENCY USE ONLY *(Leave blank)*	2. REPORT DATE	3. REPORT TYPE AND DATES COVERED
	May 15, 1997	Final January 1, 1994-March 31,1997

4. TITLE AND SUBTITLE

Crack Propagation by Element-Free Galerkin Methods

5. FUNDING NUMBERS

F49620 -
94-1-0117

6. AUTHOR(S)

Ted Belytschko

AFOSR-TR-97-0369

7. PERFORMING ORGANIZATION NAMES(S) AND ADDRESS(ES)

Department of Civil Engineering
Northwestern University
Evanston, IL 60208

8. PERFORMING ORGANIZATION REPORT NUMBER

9. SPONSORING / MONITORING AGENCY NAME(S) AND ADDRESS(ES)

Air Force Office of Scientific Research
Directorate of Aerospace and Materials Sciences
110 Duncan Ave. , Suite B115
Bolling AFB, DC 20332-8080

NA

10. SPONSORING / MONITORING AGENCY REPORT NUMBER

94-1-0117

11. SUPPLEMENTARY NOTES

The views, opinions and/or findings contained in this report are those of the author(s) and should not be construed as an official Department of the Air Force position, policy or decision, unless so designated by other documentation.

12a. DISTRIBUTION / AVAILABILITY STATEMENT

Approved for public release; distribution unlimited.

12 b. DISTRIBUTION CODE

13. ABSTRACT *(Maximum 200 words)*

The element-free Galerkin (EFG) method is a mesh-free method for solving solid mechanics problems with an approximation based only on nodes. It is developed here for linear elastic fracture problems. Smoothing of mesh-free approximations near nonconvex boundaries is done by three methods: (1) the diffraction method, in which the nodal domain of influence wrapped a short distance arund a boundary, (2) the transparency method, which is described only for cracks, yields continuous approximations by gradually severing the domains of influence near crack tips, and (3) the "see-through" method, or continuous line criterion, which does not enforce a discontinuity or crack if the tip is within the domain of influence. Two methods for enriching EFG approximations for linear elastic fracture problems are described: extrinsic enrichment involves adding the form of the solution to the trial function; for intrinsic enrichment, the EFG basis is expanded to include terms from the near tip crack solution. Several problems are solved to illustrate the effectiveness of EFG crack propagation with smoothing and enrichment.

14. SUBJECT TERMS

19971006 049

15. NUMBER IF PAGES

81

16. PRICE CODE

17. SECURITY CLASSIFICATION OR REPORT	18. SECURITY CLASSIFICATION OF THIS PAGE	19. SECURITY CLASSIFICATION OF ABSTRACT	20. LIMITATION OF ABSTRACT
UNCLASSIFIED	UNCLASSIFIED	UNCLASSIFIED	UL

CRACK PROPAGATION BY ELEMENT-FREE GALERKIN METHODS

Principle Investigator: Ted Belytschko

Final Report

January 1, 1994 - March 31, 1997

Department of Civil Engineering
Northwestern University
Evanston, IL 60208

Air Force Research Grant F49620-94-0117

Preface

This research was conducted under the direction of Professor Ted Belytschko. The following personnel participated in the research effort: Mr. Thomas Black, Mr. Mark Fleming, Mr. Yong Guo, Mr . Sang Ho Lee, and Mr. John Dolbow.

The following papers were published under sponsorship of this contract:

T. Belytschko, and Y.Y. Lu, "Explicit Multi-time Step Integration for First and Second Order Finite Element Semidiscretizations," Computer Methods in Applied Mechanics and Engineering 108, pp. 353-383, 1993.

T. Belytschko and Y.Y. Lu, "Convergence and Stability Analyses of Multi-Time Step Algorithm for Parabolic Systems," Computer Methods in Applied Mechanics and Engineering, 102, 2 pp. 179-198, 1993.

H.H. Harkness and T. Belytschko, "Simple Estimates of Stress Intensity Factors by Crack Path Approximation with Application to Fatigue Reliability," Engineering Fracture Mechanics, 45, 2, pp. 255-260, 1993.

T. Belytschko and I.-S. Yeh, "The Splitting Pinball Method for Contact-Impact Problems," Computer Methods in Applied Mechanics and Engineering, 105, pp. 375-393, 1993.

T. Belytschko and L.P. Bindeman, "Assumed Strain Stabilization of the Eight Node Hexahedral Element," Computer Methods in Applied Mechanics and Engineering, 105, pp. 225-260, 1993.

W. K. Liu and T. Belytschko, "Curvilinear Fatigue Crack Reliability Analysis by Stochastic Boundary Element Method," International Journal for Numerical Methods in Engineering, 36, pp. 3841-3858, 1993.

T. Belytschko, S.-H. Lee, I.-S. Yeh, J. I. Lin, C.-S. Tsay and J.M. Kennedy "Adaptivity in Crashworthiness Calculations," Shock and Vibration,1, No. 2, pp. 97-106, 1993.

T. Belytschko and M. Tabbara, "H-Adaptive Finite Element Methods for Dynamic Problems, with Emphasis on Localization," International Journal for Numerical Methods in Engineering, 36, pp. 4245-4265, 1993.

T. Belytschko and Y.Y. Lu, "A Variationally Coupled FE-BE method for Transient Problems," International Journal for Numerical Method in Engineering, 37, pp. 91-105, 1994.

T. Belytschko, Y.Y. Lu and L. Gu, "Element-Free Galerkin Methods," International Journal for Numerical Methods in Engineering, 37, pp. 229-256, 1994.

T. Blacker and T. Belytschko, "Superconvergent Patch Recovery with Equilibrium and Conjoint Interpolant Enhancements," International Journal of Numerical Methods in Engineering, 37, pp. 517-536, 1994.

L. Gu and T. Belytschko, "A Numerical Study of Stress Singularities in a Two-Material Wedge," International Journal of Solids Structures,31, No. 6, pp. 865-889, 1994.

Y.Y. Lu, T. Belytschko and L. Gu, "A New Implementation of the Element Free Galerkin Method," Computer Methods in Applied Mechanics and Engineering, 113, pp. 397-414, 1994.

T. Belytschko and I. Leviathan, "Physical Stabilization of the 4-node Shell Element with One Point Quadrature," Computer Methods in Applied Mechanics and Engineering, 113, pp. 321-350, 1994.

T. Belytschko and T. Blacker, "Enhanced Derivative Recovery Through Least Square Residual Penalty," Applied Numerical Mathematics, 14, pp. 55-68, 1994.

T. Belytschko, L. Gu and Y.Y. Lu, "Fracture and Crack Growth by Element Free Galerkin Methods," Modelling Simul. Mter. Sci. Eng., 2 , pp. 519-534, 1994.

T. Belytschko and I. Leviathan, "Projection Schemes for One-Point Quadrature Shell Elements," Computer Methods in Applied Mechanics and Engineering,115, pp. 277-286, 1994.

M. Tabbara, T. Blacker and T. Belytschko, "Finite Element Derivative Recovery by Moving Least Square Interpolants," Computer Methods in Applied Mechanics and Engineering, 117, pp. 211-223, 1994.

S. Beissel and T. Belytschko, "On Patterns of Deformation in Phase Transformation and Luders Bands," International Journal of Solids Structures, Vol. 33, No. 12, 1689-1707 (1996).

W.-K. Liu, Y. Chen, S. Jun, J.S. Chen and T. Belytschko, C. Pan, R.A. Uras, C.T. Chang, "Overview and Applications of the Reproducing Kernel Particle Methods," Archives of Computational Methods in Engineering, Vol 3, No. 1, 3-80 (1996).

Y. Krongauz and T. Belytschko, "Enforcement of Essential Boundary Conditions in Meshless Approximations Using Finite Elements," Computer Methods in Applied Mechanics and Engineering, Vol. 131, No. 1-2, 133-145 (1996).

W. -K. Liu, Y. Chen, C.T. Chang and T. Belytschko, "Advances in Multiple Scale Kernel Particle Methods," Computational Mechanics, Vol. 18, No. 2, 73-111 (1996).

D. Organ, M. Fleming, T. Terry, and T. Belytschko, "Continuous Meshless Approximations for Nonconvex Bodies by Diffraction and Transparency," Computational Mechanics, Vol. 18, No. 3, pp 225-235 (1996).

T. Belytschko, Y. Krongauz, M. Fleming, D. Organ, and W.K. Liu, "Smoothing and Accelerated Computations in the Element Free Galerkin Method," Journal of Computational and Applied Mathematics, Vol. 74, 111-126 (1996).

T. Belytschko, Y. Krongauz, D. Organ, M. Fleming, and P. Krysl, "Meshless Methods: An Overview and Recent Developments," Computer Methods in Applied Mechanics and Engineering, Vol. 139, 3-47 (1996).

S. Beissel and T. Belytschko, "Nodal Integration of the Element - Free Galerkin Method," Computer Methods in Applied Mechanics and Engineering. 139, 49-74 (1996).

M. Fleming, Y.A. Chu, B. Moran, and T. Belytschko, "Enriched Element-Free Galerkin Methods for Crack Tip Fields", International Journal for Numerical Methods in Engineering, Vol. 40, pp 1483-1504 (1997).

Professor Ted Belytschko served in the following offices and received the following awards during the past year:

President, U.S. Association for Computational Mechanics.

1994 Computational Mechanics award from the Japanese Society of Mechanical Engineering.

Honorary Doctorate, University of Liege, 1997.

ICES Gold Medal, International Conference on Computational Engineering and Science, 1997.

Abstract

The element-free Galerkin (EFG) method is a mesh-free method for solving solid mechanics problems with an approximation based only on nodes. It is developed here for linear elastic fracture problems. Smoothing of mesh-free approximations near nonconvex boundaries is done by three methds: (1) the diffraction method, in which the nodal domain of influence wrapped a short distance around a boundary, (2) the transparency method, which is described only for cracks, yields continuous approximations by gradually severing the domains of influence near crack tips, and (3) the "see-through" method, or continuous line criterion, which does not enforce a discontinuity or crack if the tip is within the domain of influence. Two methods for enriching EFG approximations for linear elastic fracture problems are described: extrinsic enrichment involves adding the form of the solution to the trial function; for intrinsic enrichment, the EFG basis is expanded to include terms from the near tip crack solution. Several problems are solved to illustrate the effectiveness of EFG crack propagation with smoothing and enrichment.

1 Introduction

The element-free Galerkin (EFG) method is a recently developed computational tool which has been used extensively for computing arbitrary crack paths. EFG uses a Galerkin scheme for approximating the solution to partial differential equations with an approximant written in terms of a set of nodes and the surfaces of the model. This class of methods is often called meshless, gridless or particle methods because of the absence of any predefined nodal connectivity.

Meshless methods have been in existence since the late 1970's. Lucy (1977) introduced a particle method called smoothed particle hydrodynamics (SPH) for modeling astrophysical phenomena and Gingold and Monaghan (1982) and Monaghan (1982) used this method for problems without boundaries, such as rotating stars and dust clouds. Libersky and Petschek (1991) extended this method to solve solid mechanics problems. Swegle, Hicks, and Attaway (1995) noted a tensile instability existed in SPH and Attaway, Heinstein, and Swegle (1994) coupled SPH to finite elements through a contact algorithm.

A separate branch of meshless methods arose from the work of Nayroles, Touzot, and Villon (1992), who proposed a diffuse element method (DEM) using a basis function and a weight function to form a local approximation based on a set of nodes. Belytschko, Lu, and Gu (1994) recognized that this approximation was actually the moving least squares (MLS) approximation of Lancaster and Salkauskas (1981) and developed a similar method called the element-free Galerkin (EFG) method which has been used extensively for fracture and crack growth (Belytschko, Gu, and Lu, 1994;

Belytschko, Lu, Gu, and Tabbara, 1995; Lu, Belytschko, and Tabbara, 1995). Liu, Jun, and Zhang (1995) also proposed a meshless method called the reproducing kernel particle method (RKPM) with an approximation based on a convolution integral. The form of the convolution was similar to SPH, but it contains a correction function which corrects for consistency near boundaries and for nonuniform spacing. Belytschko, Krongauz, Organ, Fleming, and Krysl (1996) have shown that the discrete form of the convolution integral yields approximants which are identical to those which come from MLS.

Meshless methods based on partitions of unity seem to provide an efficient vehicle for performing *hp* adaptivity. These methods include *hp*-clouds (Duarte and Oden, 1996b) and the partition of unity finite element method (PUFEM) (Melenk and Babuška, 1996). The *hp*-cloud method begins with a partition of unity based on moving least squares and enhances the polynomial order of the approximation through an extrinsic basis which can be added locally to nodes.

Other meshless methods which have evolved are the particle in cell (PIC) method (Sulsky, Zhou, and Schreyer, 1995), the generalized finite difference method (Liszka and Orkisz, 1980) and the finite point method (Oñate, Idelsohn, Zienkiewicz, Taylor, and Sacco, 1996). Belytschko, Krongauz, Organ, Fleming, and Krysl (1996) provide a comprehensive review of the state-of-the-art in meshless methods and details the relationship between several of the key-methods.

The element-free Galerkin method can provide an excellent complement to finite element methods in situations where finite elements is not well suited. A formulation has been presented in Belytschko, Organ, and Krongauz (1995) for consistently coupling EFG and FE by blending the approximations in a transition element. This allows the speed and simplicity of finite elements to be exploited where possible while allowing EFG to be used in regions where a meshless method is appropriate.

One class of problems which is inherently difficult with finite element methods is crack propagation for arbitrary crack paths. The predefined connectivity of the element structure in finite element methods requires special treatment if a crack is to be extended. Crack propagation has been modeled with finite elements in several ways. Early crack growth with finite elements was done by nodal release methods in which cracks were grown along finite element boundaries (Malluck and King, 1980). As the crack grew, the elements were unzipped to create new surfaces. This method suffers from a great deal of mesh dependence for arbitrary crack propagation. In addition, the crack increment is set by the element size because the crack grows from node to node.

The most obvious way to handle crack propagation is by remeshing the geometry. Swenson and Ingraffea (1988) presented a local remeshing technique in which elements ahead of the crack tip in the propagation direction were removed and the crack was extended. This area was triangulated to create a new local crack tip mesh. This

method has the advantage that a vast amount of existing finite element technology can be used for support. There are some drawbacks to this method such as difficulties if the crack step size is too small, then remeshing is unwarranted. Complex geometries and interacting crack tips are also potential difficulties as is rerunning a step with a smaller crack increment.

Al-Ostaz and Jasiuk (1995) modeled fracture and crack growth with finite elements by deleting elements which met a yield criterion. This approach, which is not based on fracture mechanics, requires a very fine mesh to get an acceptable representation of a crack. Other techniques for modeling crack growth include spring network models in which the material is represented by a network of springs and crack propagation is simulated by breaking springs (Schlangen and Mier, 1992). Boundary element methods have also been used to model crack propagation (Gallego and Dominguez, 1992). This method is attractive due to the absence of a domain mesh, making crack extension relatively simple. However, the requirements of a Green's function has limited the scope of problems this method is able to solve.

This report focuses on the element-free Galerkin methods for computational fracture mechanics. In Section 1, the moving least squares methodology is reviewed and used to construct discrete EFG approximations. Issues in modeling cracks in a meshless method are discussed. The elastostatic boundary value problem is presented along with its associated weak form. Approximation of the solution with EFG is presented and the topics of nodal domains of influence and integration of the weak form are discussed. It should be noted that the definition of a meshless method is one in which no predefined element connectivity exists for determining the approximant. Some confusion invariably arises when the meshless approximant is used in a Galerkin method. Integration of the weak form is performed by Gauss quadrature which requires some sort of integration cells. Although this detracts from the "meshless" nature of the method, the background cell structure by no means destroys it.

Smoothing of EFG approximation near nonconvex boundaries is presented in Section 4. Without smoothing, EFG approximations near nonconvex boundaries such as crack tips will contain discontinuities which extend into the domain. These discontinuities arise due to nodal domains of influence which are truncated whenever a ray from a node to a sampling point grazes the boundary. The diffraction method smooths EFG approximations by wrapping the nodal support a short distance around the point at which the discontinuity would begin. The transparency method, which is written only for cracks, yields smooth approximations by gradually enforcing the crack. The "see-through" method, or continuous line criterion, does not enforce nonconvex boundaries for situations in which a continuous line can be drawn between the node and a sampling point without leaving the domain of influence.

Section 5 presents enrichment techniques for the EFG method. These methods hinge on knowledge of the solution form and are developed for linear elastic cracks.

The enrichment method can be categorized in two ways: extrinsic enrichment enhances the approximation by adding functions to the approximation; in intrinsic enrichment, the intrinsic basis is expanded to include enrichment terms. For linear elastic cracks, enrichment can consist of adding the $\sqrt{r}$ term or adding the entire near-tip asymptotic solution.

Several example problems are presented in Section 6 to show the effects of the smoothing and enrichment as well as illustrate the effectiveness of EFG for solving problems of arbitrary crack growth.

2 Meshless Approximations by MLS

A meshless approximation for a discrete system is one which is written entirely in terms of the parameter values at nodes – no predefined connectivities are used as with finite elements or finite differences. A smooth, monotonically decreasing weight function is defined at each node such that the whole domain is covered. Common shapes of weight functions in two dimensions are circles and rectangles (see Figs. 1). The counterparts of these in three dimensions are spheres and bricks.

Two commonly used weight functions are the Gaussian and the quartic spline given in Eqs. (1). For the circular weights shown in Fig. 1a, the weight functions are

$$\text{Gaussian:} \quad w(d_I) = \begin{cases} \dfrac{\exp(-(d_I/c)^2) - \exp(-(d_{mI}/c)^2)}{1 - \exp(-(d_{mI}/c)^2)} & d_I \le d_{mI} \\ 0 & d_I > d_{mI} \end{cases} \tag{1a}$$

$$\text{quartic spline:} \quad w(d_I) = \begin{cases} 1 - 6\left(\dfrac{d_I}{d_{mI}}\right)^2 + 8\left(\dfrac{d_I}{d_{mI}}\right)^3 - 3\left(\dfrac{d_I}{d_{mI}}\right)^4 & d_I \le d_{mI} \\ 0 & d_I > d_{mI} \end{cases} \tag{1b}$$

where $d_I = \|\mathbf{x} - \mathbf{x}_I\|$ is the distance from a sampling point $\mathbf{x}$ to a node $\mathbf{x}_I$, and d_{mI} is the domain of influence of a node, i.e., the area for which the weight function is nonzero. The variable c in the Gaussian weight is used to control the dilation of the weight function. It is useful to define a characteristic nodal spacing, c_I, which is a distance such that a node will yield a minimum set of neighbors sufficient for regularity of the equations used to determine the approximant. The weight function parameters are defined in terms of c_I

$$d_{mI} = d_{max} c_I \tag{2}$$

$$c = \alpha c_I \tag{3}$$

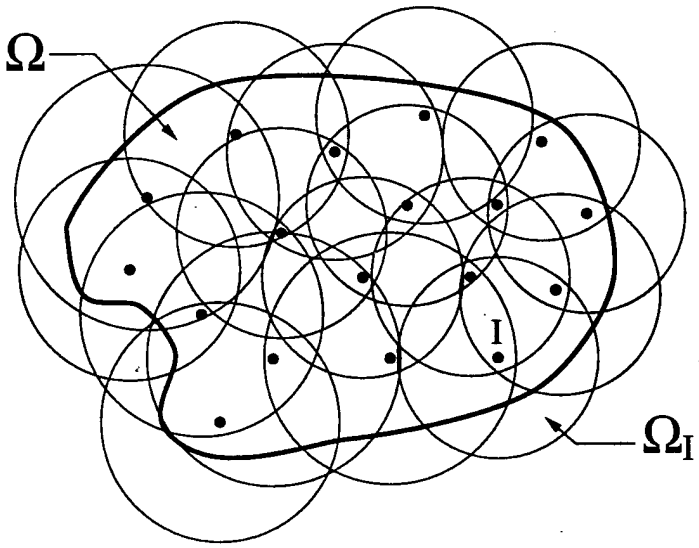

(a) Circular.

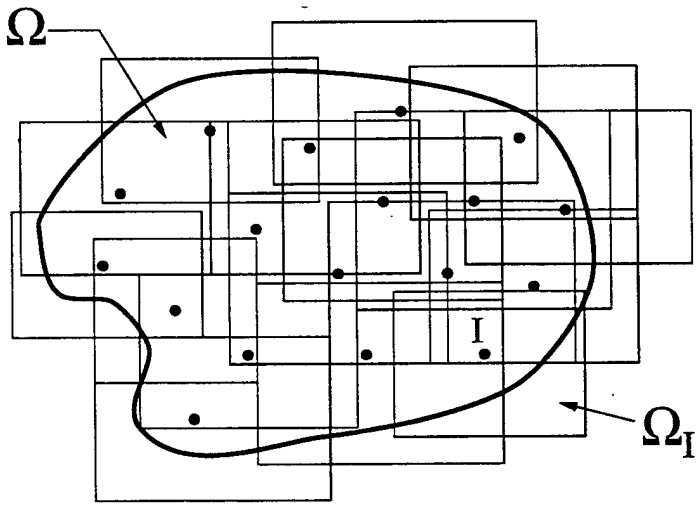

(b) Rectangular.

Figure 1: A computational model for a meshless method showing the boundary, nodes and supports.

where d_{max} and α are constants. For the Gaussian weight function in Eq. (1a), the parameter α is a dilation parameter which controls the shape of the weight function. If α is kept constant while d_{max} is increased, the shape of the weight function will not change and the effective domain of influence will be smaller than the actual domain of influence. It is necessary to have the ratio $d_{max}/\alpha \geq 4.0$ to avoid poorly-formed shape functions. In addition, $\alpha > 0.5$ is needed for smooth shape functions and derivatives. In this report, the Gaussian weight with $d_{max} = 2.5, \alpha = 0.625 (= d_{max}/4)$ is used unless otherwise stated. The characteristic nodal spacing, c_I, is chosen as the distance to the second nearest neighbor for regularly spaced nodes and the distance to the third nearest neighbor for irregularly spaced nodes.

The approximation of a function $u(\mathbf{x})$ at any point $\mathbf{x}$ in the domain Ω is written

$$u^h(\mathbf{x}) = \mathbf{p}^T(\mathbf{x})\mathbf{a}(\mathbf{x}) \tag{4}$$

where $\mathbf{p}(\mathbf{x})$ is a basis (usually polynomial) and $\mathbf{a}(\mathbf{x})$ are unknown coefficients. Some complete polynomial bases are

$$\begin{aligned}
&\text{1D:} && \mathbf{p}^T(\mathbf{x}) = [1, x] && \text{linear} && (5a)\\
& && \mathbf{p}^T(\mathbf{x}) = [1, x, x^2] && \text{quadratic} && (5b)\\
&\text{2D:} && \mathbf{p}^T(\mathbf{x}) = [1, x, y] && \text{linear} && (5c)\\
& && \mathbf{p}^T(\mathbf{x}) = [1, x, y, x^2, xy, y^2] && \text{quadratic} && (5d)
\end{aligned}$$

In Section 5 it is shown that other functions can be added to the basis in situations where it is desirable to enrich the solution.

To find the approximation of the field variable by Eq. (4), it is necessary to determine the coefficients $\mathbf{a}(\mathbf{x})$. The moving least squares (MLS) methodology (Lancaster and Salkauskas, 1981) is an effective technique for approximating a function using a set of scattered data. Given a set of nodes with coordinates $\mathbf{x}_I$ at which the field variable u_I is known, a weighted $\mathcal{L}_2$ norm can be written

$$J = \sum_{I=1}^{n} w(\mathbf{x} - \mathbf{x}_I) \left[\mathbf{p}^T(\mathbf{x}_I)\mathbf{a}(\mathbf{x}) - u_I\right]^2 \tag{6}$$

where $w(\mathbf{x} - \mathbf{x}_I)$ is the weight function of node I at point $\mathbf{x}$, and n is the number of neighbors of point $\mathbf{x}$, i.e., nodes with $w(\mathbf{x} - \mathbf{x}_I) > 0$.

Finding the minimum of J with respect to $\mathbf{a}(\mathbf{x})$ leads to a set of linear equations

$$\mathbf{A}(\mathbf{x})\mathbf{a}(\mathbf{x}) = \mathbf{C}(\mathbf{x})\mathbf{u} \tag{7}$$

where

$$\mathbf{A}(\mathbf{x}) = \sum_{I=1}^{n} w(\mathbf{x}-\mathbf{x}_I)\mathbf{p}(\mathbf{x}_I)\mathbf{p}^T(\mathbf{x}_I) \tag{8a}$$

$$\mathbf{C}(\mathbf{x}) = [w(\mathbf{x}-\mathbf{x}_1)\mathbf{p}(\mathbf{x}_1), w(\mathbf{x}-\mathbf{x}_2)\mathbf{p}(\mathbf{x}_2), \ldots, w(\mathbf{x}-\mathbf{x}_n)\mathbf{p}(\mathbf{x}_n)] \tag{8b}$$

$$\mathbf{u} = [u_1, u_2, \ldots, u_n]\,. \tag{8c}$$

The matrix $\mathbf{A}(\mathbf{x})$ is often called the moment matrix and $\mathbf{C}(\mathbf{x})$ is a matrix of column vectors. Eq. (7) can be solved for $\mathbf{a}(\mathbf{x})$ to yield

$$\mathbf{a}(\mathbf{x}) = \mathbf{A}^{-1}(\mathbf{x})\mathbf{C}(\mathbf{x})\mathbf{u}$$

which can be substituted into Eq. (4) to yield an approximation in terms of the nodal coefficients

$$u^h(\mathbf{x}) = \sum_{I=1}^{n} \mathbf{p}^T(\mathbf{x})\mathbf{A}^{-1}(\mathbf{x})\mathbf{C}_I(\mathbf{x})u_I\,, \tag{9}$$

where $\mathbf{C}_I(\mathbf{x})$ is the Ith column of $\mathbf{C}(\mathbf{x})$ and u_I is the nodal coefficient for the Ith neighbor of $\mathbf{x}$. Defining the shape function $\phi_I(\mathbf{x})$ as

$$\phi_I(\mathbf{x}) = \mathbf{p}^T(\mathbf{x})\mathbf{A}^{-1}(\mathbf{x})\mathbf{C}_I(\mathbf{x}) \tag{10}$$

allows the approximation to be written as

$$u^h(\mathbf{x}) = \sum_{I=1}^{n} \phi_I(\mathbf{x})u_I\,, \tag{11}$$

which is a form familiar to those with a finite element background.

The spatial derivatives of the shape functions, computed by the chain rule, are

$$\phi_{I,i}(\mathbf{x}) = \mathbf{p}^T_{,i}(\mathbf{x})\mathbf{A}^{-1}(\mathbf{x})\mathbf{C}_I(\mathbf{x}) + \mathbf{p}^T(\mathbf{x})\left[\mathbf{A}^{-1}_{,i}(\mathbf{x})\mathbf{C}_I(\mathbf{x}) + \mathbf{A}^{-1}(\mathbf{x})\mathbf{C}_{I,i}(\mathbf{x})\right] \tag{12}$$

where $\mathbf{A}^{-1}_{,i} = -\mathbf{A}^{-1}\mathbf{A}_{,i}\mathbf{A}^{-1}$. Note that the second term in Eq. (12) is expensive to compute because of the term $\mathbf{A}^{-1}_{,i}$. Nayroles, Touzot, and Villon (1992) computed only the first term of the derivatives which results in the inability of their approximation to satisfy the patch test. Krongauz and Belytschko (1997a) have shown that the method can be rendered convergent by a Petrov-Galerkin formulation.

2.1 Fast shape function and derivative computation

The number of operations required to form shape functions and derivatives can be decreased by the procedure in Belytschko, Krongauz, Fleming, Organ, and Liu (1996) and Fleming, Chu, Moran, and Belytschko (1997). The shape function in Eq. (10) can be written as

$$\phi_I(\mathbf{x}) = \underline{\mathbf{p}^T(\mathbf{x})\mathbf{A}^{-1}(\mathbf{x})}\mathbf{C}_I(\mathbf{x}) = \underline{\boldsymbol{\gamma}^T(\mathbf{x})}\mathbf{C}_I(\mathbf{x}) \tag{13}$$

with corresponding derivatives

$$\phi_{I,i}(\mathbf{x}) = \boldsymbol{\gamma}^T_{,i}(\mathbf{x})\mathbf{C}_I(\mathbf{x}) + \boldsymbol{\gamma}^T(\mathbf{x})\mathbf{C}_{I,i}(\mathbf{x})\,. \tag{14}$$

Comparing the underlined terms in Eq. (13) leads to the relationship

$$\mathbf{A}(\mathbf{x})\boldsymbol{\gamma}(\mathbf{x}) = \mathbf{p}(\mathbf{x}). \tag{15}$$

The coefficients $\boldsymbol{\gamma}(\mathbf{x})$ can be obtained by an LU decomposition of $\mathbf{A}(\mathbf{x})$ and backsubstitution. This requires fewer computations than a full inversion of $\mathbf{A}(\mathbf{x})$, which is required to form the shape functions with Eq. (10).

The derivative of $\boldsymbol{\gamma}(\mathbf{x})$ is required to compute the shape function derivatives in Eq. (14). Taking the derivative of Eq. (15)

$$\mathbf{A}_{,i}(\mathbf{x})\boldsymbol{\gamma}(\mathbf{x}) + \mathbf{A}(\mathbf{x})\boldsymbol{\gamma}_{,i}(\mathbf{x}) = \mathbf{p}_{,i}(\mathbf{x}) \tag{16}$$

and rearranging known terms which to the right-hand side leads to

$$\mathbf{A}(\mathbf{x})\boldsymbol{\gamma}_{,i}(\mathbf{x}) = \mathbf{p}_{,i}(\mathbf{x}) - \mathbf{A}_{,i}(\mathbf{x})\boldsymbol{\gamma}(\mathbf{x})\,. \tag{17}$$

Using the LU decomposition of $\mathbf{A}(\mathbf{x})$, which is known from solving Eq. (15), $\boldsymbol{\gamma}_{,i}(\mathbf{x})$ can be computed with only a backsubstitution. Higher order derivatives can be easily obtained by repeating the procedure used for computing the first derivative.

While this procedure for computing shape functions and their derivatives is theoretically identical to directly evaluating Eqs. (10) and (12), the number of computations is reduced. In addition to increasing speed, this modification can also alleviate ill conditioning of shape functions in cases where the moment matrix, $\mathbf{A}(\mathbf{x})$, is not well conditioned.

2.2 Modeling cracks with EFG

A crack is modeled in EFG by defining a line segment internal to the domain. The domains of influence for nodes near the crack are truncated whenever they intersect the crack surface so that a node on one side of the crack will not affect points on the

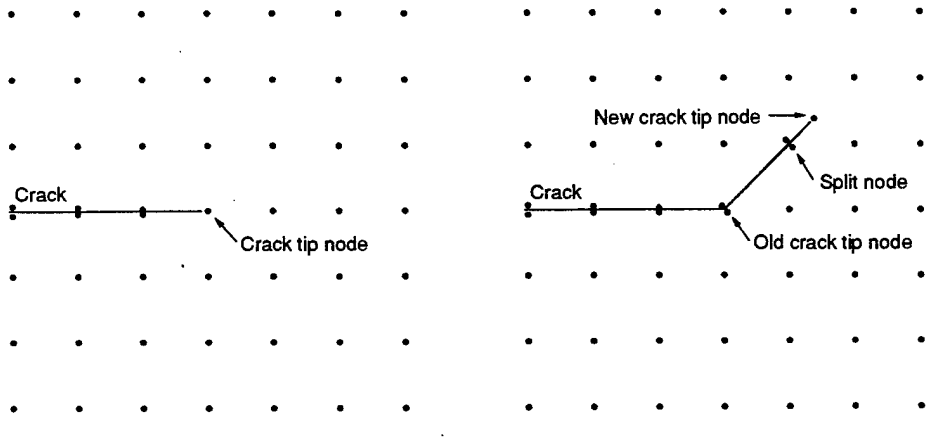

(a) Initial setup (b) After 1 step

Figure 2: Crack setup for modeling crack propagation with EFG.

opposite side of the crack. This technique was first presented in Belytschko, Lu, and Gu (1994) has been called the *visibility criterion* by Krysl and Belytschko (1996). The nodal domain of influence can be considered as the line of sight and a crack can be considered as an opaque boundary. Whenever the line of sight meets the opaque boundary, the domain of influence is cut. The visibility criterion has some limitations near crack tips which are discussed in Section 4. Determining whether a line drawn between a node and a sampling point intersects a crack segment requires an efficient and robust algorithm capable of handling complex geometries. The Sedgewick algorithm (Sedgewick, 1988) is found to work well.

One of the biggest benefits of meshless methods such as EFG is their inherent ability to model arbitrary crack propagation due to the absence of a predefined element connectivity. Growing a crack consists of simply adding another line segment at the existing crack tip as shown in Fig. 2.

As the crack propagates, it will pass directly through the current crack tip node and may pass through other nodes as well. In this case, the node is replaced by two nodes, one above the crack and another below the crack (see Fig. 2). This is preferred to deleting the node because it increases the spatial resolution along the crack surface.

Using a linear basis for crack problems necessitates increased nodal refinement around the crack tip in order to capture the crack tip stress field accurately. A star-shaped array of nodes consisting of several rings of nodes around the crack tip is found to work well. A recommended arrangement of nodes is given in (Terry, 1994). The star-shaped arrangement is found to be more effective if existing nodes which

fall within the radius of the star are turned off (except for the crack tip node). For a propagating crack, the star-shaped array moves with the crack tip and turned off nodes are turned back on once they are no longer in the radius of the star.

3 Elastostatics

The report focuses on fracture of linear elastic media. The elastostatic boundary value problem is reviewed, the variational form is given and numerical approximations by mesh-free methods are shown; enforcement of essential boundary conditions is also discussed.

Consider a two-dimensional domain Ω bounded by Γ. The equation of equilibrium is

$$\nabla \cdot \boldsymbol{\sigma} + \mathbf{b} = \mathbf{0} \qquad \text{in } \Omega \tag{18}$$

where $\boldsymbol{\sigma}$ is the stress tensor for a displacement field $\mathbf{u}$, and $\mathbf{b}$ is the body force. The boundary conditions are

$$\begin{aligned} \mathbf{u} &= \bar{\mathbf{u}} && \text{on } \Gamma_u \\ \boldsymbol{\sigma} \cdot \mathbf{n} &= \bar{\mathbf{t}} && \text{on } \Gamma_t \end{aligned}$$

where the superposed bar indicates prescribed values and $\mathbf{n}$ is the unit normal vector to Γ.

The variational (or weak) form for Eq. (18) can be written

$$\delta W \triangleq \int_\Omega \nabla_s \delta\mathbf{u} : \boldsymbol{\sigma} d\Omega - \int_\Omega \delta\mathbf{u} \cdot \mathbf{b} d\Omega - \int_{\Gamma_t} \delta\mathbf{u} \cdot \bar{\mathbf{t}} d\Gamma - \delta W_u(\mathbf{u}) = 0, \ \forall \delta\mathbf{u} \in \mathcal{H}^1 \tag{19}$$

where ∇_s is the symmetric gradient operator and $\delta\mathbf{u}$ is a test function from the same space of functions as $\mathbf{u}$, i.e., this is a Bubnov-Galerkin method (see Hughes (1987)). The term $\delta W_u(\mathbf{u})$ is required for enforcing the essential boundary conditions in a meshless method and will be discussed in the subsequent section.

For linear elasticity,

$$\boldsymbol{\varepsilon} = \nabla_s \mathbf{u} \qquad \boldsymbol{\sigma} = \mathbf{D} : \boldsymbol{\varepsilon} \tag{20}$$

which can be used to write the weak form from Eq. (19) in terms of the displacement, $\mathbf{u}$.

The discrete form of Eq. (19) for a meshless method can be obtained using the approximation from Eq. (11) as an approximation for $\mathbf{u}$ and $\delta\mathbf{u}$ to get the system of equations

$$\mathbf{K}\mathbf{u} = \mathbf{f}^{ext}. \tag{21}$$

The stiffness matrix $\mathbf{K} \in \Re^{neq \times neq}$ (neq is the number of equation) and the external force vector $\mathbf{f}^{ext} \in \Re^{neq}$ are composed of the submatrices

$$\mathbf{K}_{IJ} = \int_{\Omega} \mathbf{B}_I \mathbf{D} \mathbf{B}_J d\Omega \tag{22a}$$

$$\mathbf{f}_I^{ext} = \int_{\Gamma_t} \phi_I \bar{\mathbf{t}} d\Gamma + \int_{\Omega} \phi_I \mathbf{b} d\Omega \tag{22b}$$

where $\mathbf{K}_{IJ} \in \Re^{nsd \times nsd}$, $\mathbf{f}_I^{ext} \in \Re^{nsd}$ (nsd is number of spatial dimensions), $\mathbf{D}$ is the constitutive matrix

$$\mathbf{D} = \frac{E}{(1+\nu)(1-2\nu)} \begin{bmatrix} 1-\nu & \nu & 0 \\ \nu & 1-\nu & 0 \\ 0 & 0 & \frac{1-2\nu}{2} \end{bmatrix} \qquad \text{plane strain} \tag{23}$$

$$\mathbf{D} = \frac{E}{1-\nu^2} \begin{bmatrix} 1 & \nu & 0 \\ \nu & 1 & 0 \\ 0 & 0 & \frac{1-\nu}{2} \end{bmatrix} \qquad \text{plane stress} \tag{24}$$

and $\mathbf{B}_I$ is a matrix of shape function derivatives

$$\mathbf{B}_I = \begin{bmatrix} \phi_{I,x} & 0 \\ 0 & \phi_{I,y} \\ \phi_{I,y} & \phi_{I,x} \end{bmatrix} . \tag{25}$$

3.1 Enforcement of essential boundary conditions

One drawback of MLS approximations is that essential boundary conditions cannot be satisfied directly because $\phi_I(\mathbf{x}_J) \neq \delta_{IJ}$, and consequently, shape functions from nodes on the interior of the domain are nonzero on the boundary. The term $\delta W_u(\mathbf{u})$ in Eq. (19) is one way of enforcing essential boundary conditions. Some forms which have been suggested are 1) Lagrange multipliers (Belytschko, Lu, and Gu, 1994)

$$\delta W_u(\mathbf{u}) = \int_{\Gamma_u} \delta\lambda \cdot (\mathbf{u} - \bar{\mathbf{u}}) d\Gamma + \int_{\Gamma_u} \delta\mathbf{u} \cdot \lambda d\Gamma , \tag{26}$$

where λ is a Lagrange multiplier, 2) a modified variational principle in which the Lagrange multipliers are replaced by their physical meaning, the traction (Lu, Belytschko, and Gu, 1994)

$$\delta W_u(\mathbf{u}) = \int_{\Gamma_u} \delta\mathbf{t} \cdot (\mathbf{u} - \bar{\mathbf{u}}) d\Gamma + \int_{\Gamma_u} \delta\mathbf{u} \cdot \mathbf{t} d\Gamma , \tag{27}$$

where $\mathbf{t} = \boldsymbol{\sigma} \cdot \mathbf{n}$, and 3) a penalty method (Belytschko, Gu, and Lu, 1994)

$$W_u(\mathbf{u}) = \frac{\beta}{2} \int_{\Gamma_u} \|\mathbf{u} - \bar{\mathbf{u}}\|^2 d\Gamma \tag{28}$$

where β is a penalty parameter.

Another method of enforcing essential boundary conditions in meshless methods is by coupling with finite elements (Krongauz and Belytschko, 1996; Belytschko, Organ, and Krongauz, 1995). In this method, a row of finite elements is placed along the essential boundaries allowing the boundary conditions to be enforced by prescribing the values at the nodes.

3.2 Integration issues

Computing the stiffness matrix and force vector from Eqs. (22) requires an integration over the domain Ω, which in two dimensions corresponds to an area integration. Integrating the stiffness matrix and force vector requires a numerical integration scheme such as Gauss quadrature, which in turn, requires a subdivision of the domain. Since meshless methods have no inherent subdivision of the domain like finite elements, it is necessary to introduce a subdivision of the domain. One type is a background cell structure. Two subdivisions are shown in Figs. 3. The first one shown, which is the most common, uses a finite element mesh generator to create a cell structure which matches the domain; this technique is often called an *element quadrature*. The vertices of this background mesh are often used as the initial array of nodes for the EFG model; however, additional nodes may be added where desired such as the nodes at the crack tip in the model shown.

The second integration technique, which is often called *cell quadrature*, uses a background grid of cells which is independent of the domain. At each integration point it is necessary to determine if it lies inside the domain before it is used for integrating Eqs. (22). This technique is not widely used because it does not yield good accuracy along curved and angled boundaries.

A nodal integration technique was proposed by Beissel and Belytschko (1996) in an effort to make EFG a completely meshless method. However, additional stability terms must be added to make the method stable and accuracy is not as good as cell-based integration schemes.

Hegen (1997) proposed subdividing the cells through which a crack passes by a triangulation technique to avoid integration errors. This subdivision is not found to significantly increase the accuracy of EFG computations and imposes undesirable "remeshing" conditions on a meshless method. The lack of a noticeable effect when aligning the cell structure with a crack can be shown by using the model shown in Fig. 4. A crack is placed between rows of nodes and the near crack tip displacement

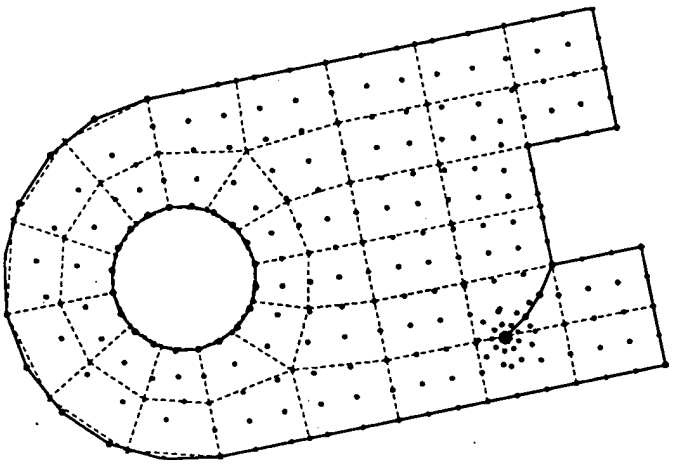

(a) Element quadrature

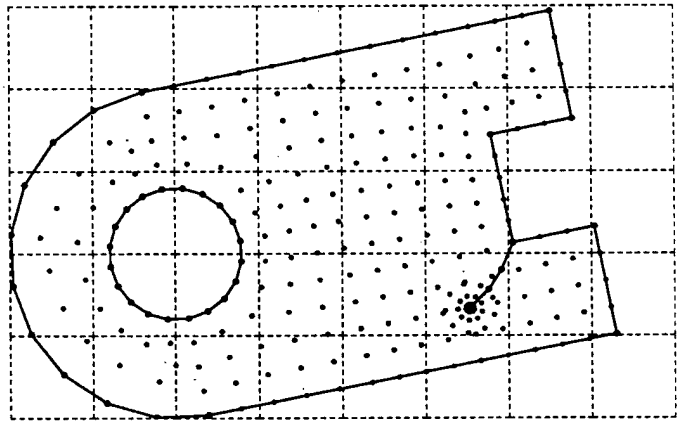

(b) Cell quadrature

Figure 3: Two integration methods for integrating the weak form with a meshless method.

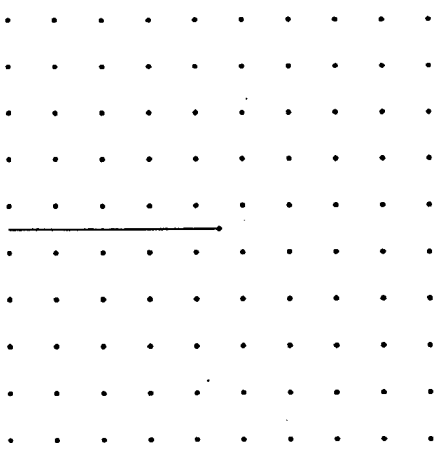

Figure 4: Discrete model for near-tip crack problem.

field is applied to the boundary; for this problem, the asymptotic near-tip field is the exact solution. Gauss quadrature is performed in a cell structure with vertices at the nodes. The problem is also solved by dividing the cells through which the crack passes so that the cell boundaries coincide with the crack. No appreciable change in the error in strain energy (1% change) or stress intensity factor (0.1% change) was noticed when the crack was allowed to pass through the middle of the cell.

In this report, element quadrature is used with 4×4 Gauss quadrature points in each cell. For cells near a crack tip, the quadrature order is increased to 9×9. Cells surrounding a crack are not subdivided to align cell boundaries with the crack.

3.3 Domains of influence

Properly choosing the domain of influence or nodal support is an important aspect of meshless methods. The size of the support should be sufficiently large so that the moment matrix is regular and well conditioned and that the spatial distribution of neighbors is fairly even. On the other hand, choosing domains of influence which are too large leads to a great deal of computational expense in forming the approximations as well as assembling the stiffness matrix. Support sizes which are too large also detract from the local character of the approximation; for problems involving sharp gradients, some loss of accuracy is typically noted as the effect of the gradient is smeared.

These aspects of meshless methods are easily shown by considering a one dimensional bar on the domain $0 \leq x \leq \pi$ with Young's modulus of $E = 1$. The bar is loaded with a body force $b(x) = \sin(x)$ and boundary conditions $u(0) = 0, \sigma(\pi) = -1$. Evenly spaced nodal arrangements ranging from 21 to 201 nodes are used and the characteristic nodal spacing, c_I, is set equal to the nodal spacing; the nodal support size is $d_{mI} = d_{max}\, c_I$. Fig. 5 presents the stress profile along the length of the bar computed using $d_{max} = 2.0$ and $d_{max} = 1.01$ and Fig. 6 shows results for the error in energy computed with varying support sizes. When the support size is only slightly larger than the nodal spacing, the error is high and the stress field mimics a linear finite element solution, i.e., the stress is nearly discontinuous at the nodes. Increasing the support size to $d_{max} = 2.0$ or 2.5 leads to a sharp improvement in accuracy, although the rate of convergence remains the same. Further increasing to $d_{max} = 3.0$ and 3.5 actually leads to an increase in error, most likely because the gradients in the solution become smeared for such large nodal supports. Note that the rate of convergence in each case is linear and only the absolute accuracy increases with increasing d_{max}. These results disagree with the results of Liu, Li, and Belytschko (1996) and Duarte and Oden (1996a), who showed increasing rates of convergence. This increasing rate of convergence is perhaps attributable to keeping the domain of influence constant in size as the mesh is refined. Note that the RKPM in Liu, Li, and Belytschko (1996) and the *hp*-clouds both used the moving least squares approximations (see Belytschko, Krongauz, Organ, Fleming, and Krysl (1996)).

Determining proper domains of influence in two and three dimensions is more difficult than in one dimension. The stress fields are usually much more complicated and evenly spaced nodal arrangements are not practical.

4 Smoothing of EFG approximations near nonconvex boundaries

The smoothness which is inherent in meshless methods is a two-edged sword. On one hand, it provides approximations of functions and their derivatives which are smooth and have the same continuity as the weight function. However, in cases where a discontinuity is present in either the geometry or the material, this higher order smoothness leads to difficulties which must be addressed in order to obtain good accuracy. Discontinuities can arise from material and geometric sources. A material discontinuity occurs along an interface between two materials with different properties, leading to discontinuous strains across the interface. This situation is easily modeled using finite elements where the interpolants are C^0. Cordes and Moran (1996) have solved problems with multiple materials using EFG by treating the individual materials as separate bodies and joining them together with Lagrange

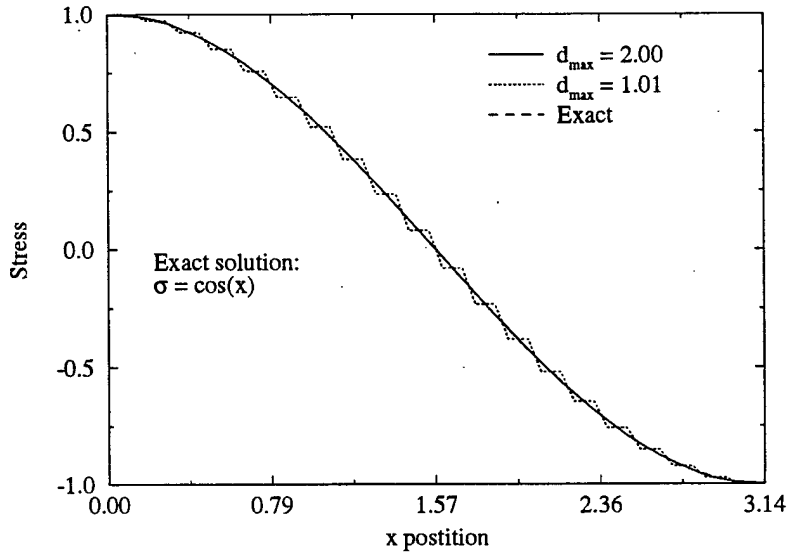

Figure 5: Stress distribution along one dimensional bar using 20 nodes.

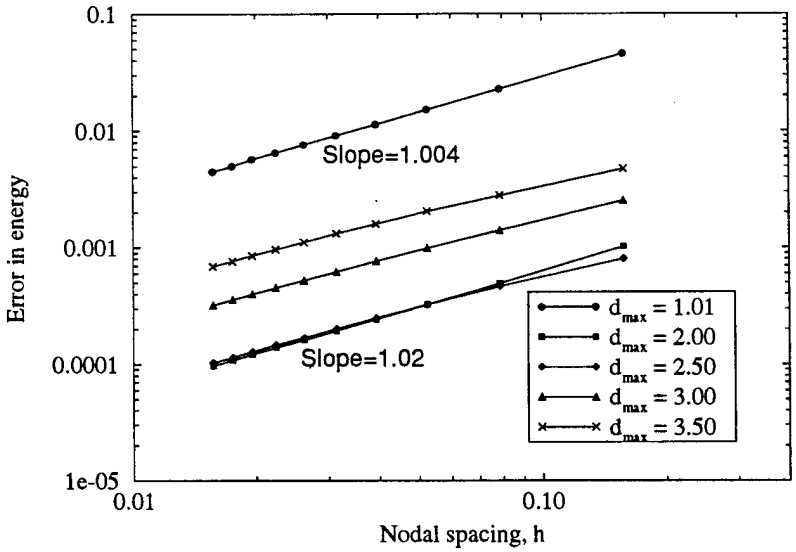

Figure 6: Error in energy versus nodal spacing with various support sizes for a one-dimensional bar with $b(x) = \sin(x)$.

multipliers. Krongauz and Belytschko (1997b) have developed techniques in which a so-called jump term is included in the trial function which is capable of representing the discontinuity. The magnitude of the jump becomes an unknown in the Galerkin discretization.

The second class of problems which contain discontinuities are due to geometrical effects. This includes cases where a boundary of the geometry is nonconvex, such as a body with a hole or a crack. Because of the aforementioned smoothness of meshless methods, special procedures are required near nonconvex boundaries. In this section, techniques for modeling nonconvex boundaries will be discussed. The *visibility* criterion will be presented first and some of its limitations will be pointed out. To overcome some of the limitations of the visibility criterion, the *diffraction, transparency* and *"see-through"* methods are introduced. Numerical examples will be given to illustrate the behavior of these alternative techniques and show when they are necessary.

4.1 Visibility Criterion

The first technique for dealing with nonconvex boundaries is the *visibility* criterion (Belytschko, Lu, and Gu (1994), the name was coined in Krysl and Belytschko (1996)). In this straightforward approach, the domain of influence is considered as the field of vision at a node. All boundaries, internal and external, are considered to be opaque so that the field of vision is interrupted as soon as such a boundary is encountered. Consider node J in Fig. 7, where the surface of the crack is within its domain of influence and is therefore truncated. This truncation will create a discontinuity in the shape function for node J which will lead to the desired discontinuity in the solution across the crack (see Fig. 8a,c).

A difficulty with the visibility criterion arises for nodes near the end of a discontinuity, i.e., a crack tip in fracture mechanics. Consider node I in Fig. 7. The field of vision is cut by the crack, leading to a discontinuity along line AC, i.e., the line of the crack. However, the field of vision is also truncated along line AB, which extends into the domain. This leads to a discontinuity in the weight function as well as the shape function along this line as shown in Fig. 8b,d. Note that because the shape functions are created from the interaction of weight functions, additional discontinuities arise in the shape functions from other nodes which have discontinuous weight functions due to the crack tip.

Discontinuities in the shape functions can also arise for nodes near the surface of nonconvex boundaries such as a hole. As an example, consider the domain of influence of node I in Fig. 9. Whenever a ray emanating from the node grazes the surface of the hole such as points A or C, the weight function will have a discontinuity along lines AB and CD. A contour plot of the weight function for node I is shown in Fig. 10a

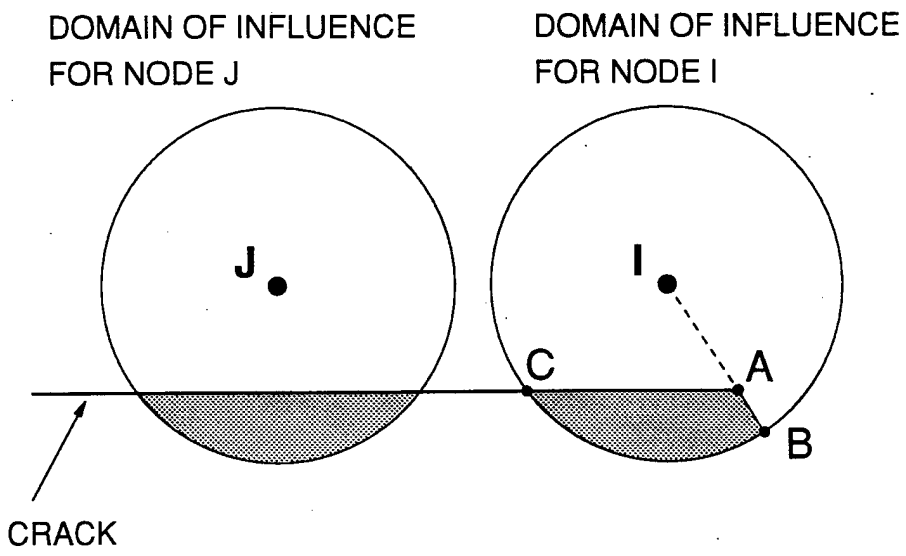

Figure 7: Domain of influence by the visibility criterion near a crack.

and the corresponding shape function is shown in Fig. 10b. Note that the shape function has several lines of discontinuity because it is formed by the interaction of several weight functions, some of which have discontinuities similar to those shown in Fig. 10a.

The presence of discontinuities within the domain is undesirable in a Galerkin method and must be handled with care. The length and size of the discontinuities is a function of the nodal refinement near a nonconvex boundary, i.e., as the nodal spacing goes to zero, the discontinuities go to zero. Using this argument and others similar to the arguments used in proving convergence for nonconforming finite elements, Krysl and Belytschko (1996) showed that the discontinuous approximations generated by the visibility criterion can lead to convergent solutions.

4.2 Diffraction Method

Continuous and smooth approximations near nonconvex boundaries can be constructed quite easily by the *diffraction* method (Organ, Fleming, and Belytschko, 1996; Organ, 1996; Belytschko, Krongauz, Fleming, Organ, and Liu, 1996). The nodal support is wrapped around nonconvex boundaries similar to the way light diffracts around sharp corners. This method, which has also been called the *wrap-around* method, is quite general and can be used for cracks or smooth boundaries such as interior holes. The method will first be described for cracks and then generalized for other nonconvex boundaries.

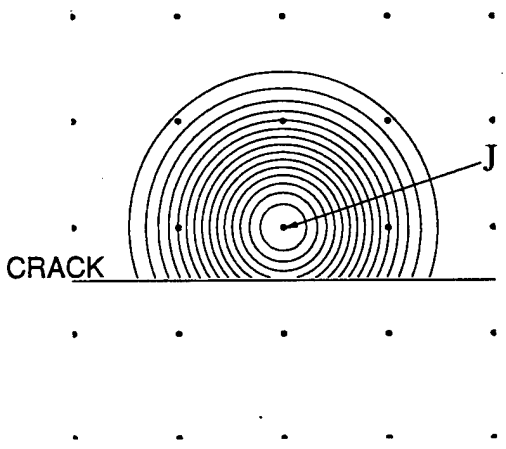

(a) Weight function for node J

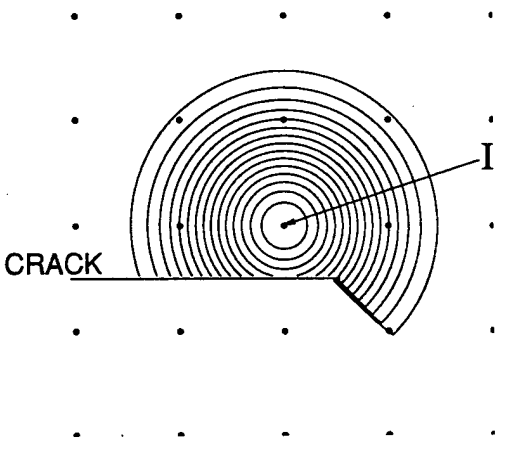

(b) Weight function for node I

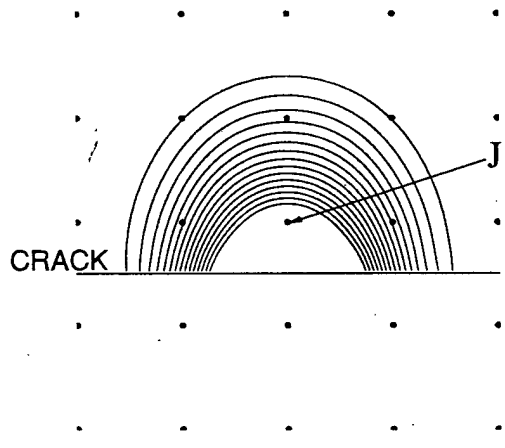

(c) Shape function for node J

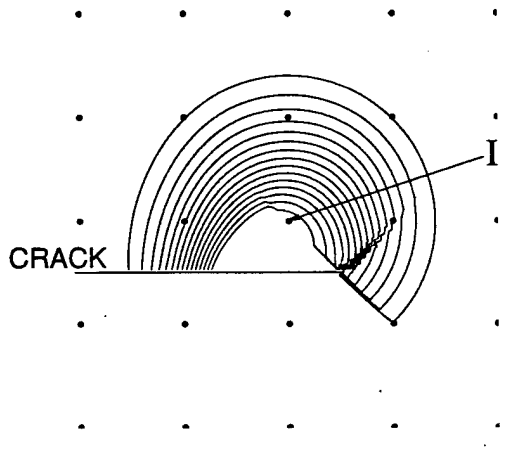

(d) Shape function for node I

Figure 8: Contour plots of the weight function $w(\mathbf{x}-\mathbf{x}_I)$ and shape function $\phi_I(\mathbf{x})$ as determined by the visibility criterion for nodes adjacent to a line of discontinuity due to a crack.

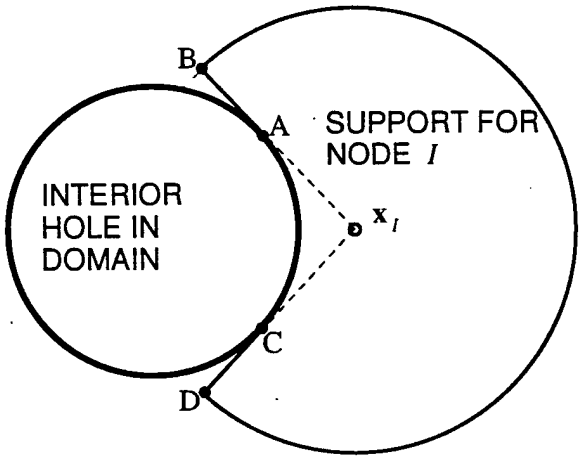

Figure 9: Domain of influence near an interior hole by the visibility criterion.

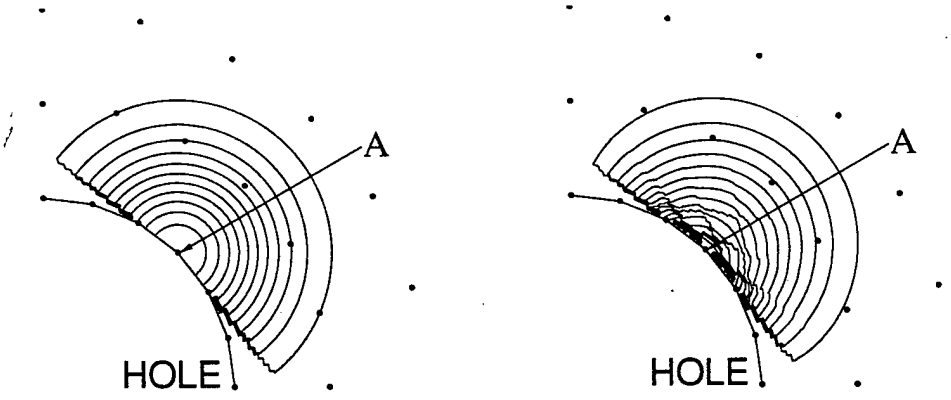

(a) Weight function for node A

(b) Shape function for node A

Figure 10: Contours for weight and shape function near an interior hole by the visibility criterion.

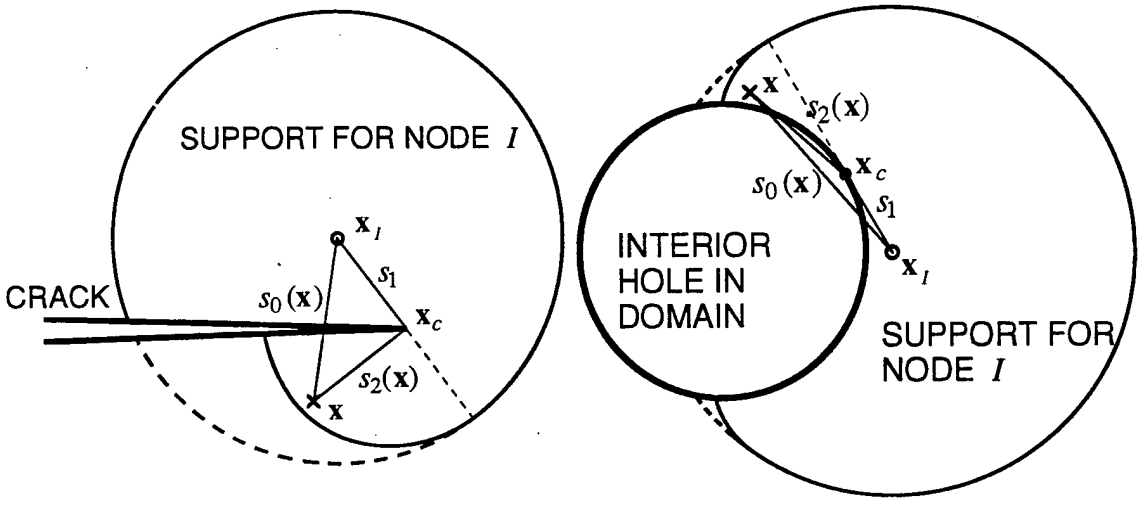

(a) Support around a crack tip.

(b) Support around a hole.

Figure 11: The diffraction (wrap-around) method for constructing smooth weight functions around nonconvex boundaries.

Consider Fig. 11a, where a line between the node, $\mathbf{x}_I$, and a sampling point, $\mathbf{x}$, intersects a crack and the tip is within the domain of influence of the node. The weight function distance, d_I, is modified (lengthened) by

$$d_I = \left(\frac{s_1 + s_2(\mathbf{x})}{s_0(\mathbf{x})}\right)^{\lambda} s_0(\mathbf{x}) \tag{29}$$

where $s_1 = \|\mathbf{x}_I - \mathbf{x}_c\|$, $s_2(\mathbf{x}) = \|\mathbf{x} - \mathbf{x}_c\|$, $s_0(\mathbf{x}) = \|\mathbf{x} - \mathbf{x}_I\|$, and $\mathbf{x}_I$ is the node, $\mathbf{x}$ is the sampling point, and $\mathbf{x}_c$ is the crack tip. The parameter λ is used to adjust the distance of the support on the opposite side of the crack. It was found that $\lambda = 1, 2$ performs well. Contour plots of the weight and shape functions by the diffraction method are shown in Fig. 12 and surface plots are shown in Fig. 13.

The spatial derivatives of the weight function are computed using the chain rule:

$$\frac{dw}{dx_i} = \frac{\partial w}{\partial d_I}\frac{\partial d_I}{\partial x_i}. \tag{30}$$

Since $\partial w/\partial d_I$ is unchanged, all that is necessary are expressions for $\partial d_I/\partial x_i$:

$$\frac{\partial d_I}{\partial x_i} = \lambda\left(\frac{s_1 + s_2}{s_0}\right)^{\lambda-1}\frac{\partial s_2}{\partial x_i} + (1-\lambda)\left(\frac{s_1 + s_2}{s_0}\right)^{\lambda}\frac{\partial s_0}{\partial x_i}, \tag{31}$$

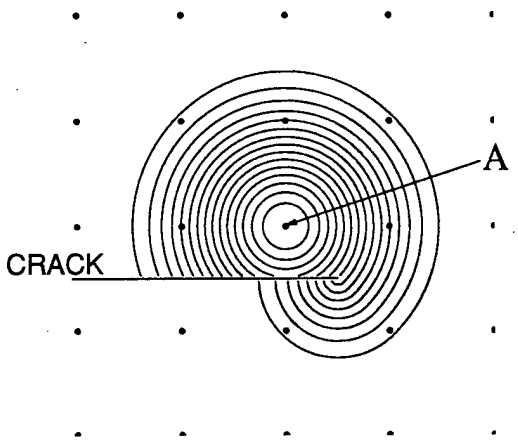

(a) Weight function for $\lambda = 1$.

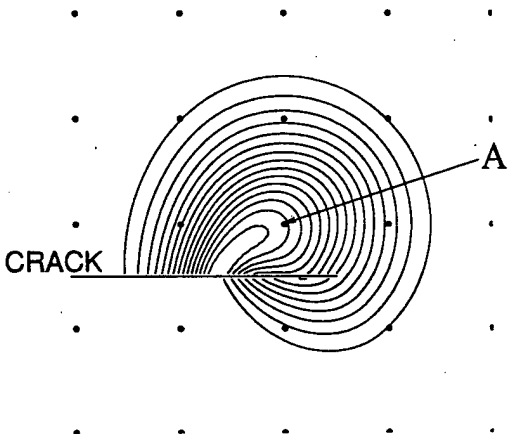

(b) Shape function for $\lambda = 1$.

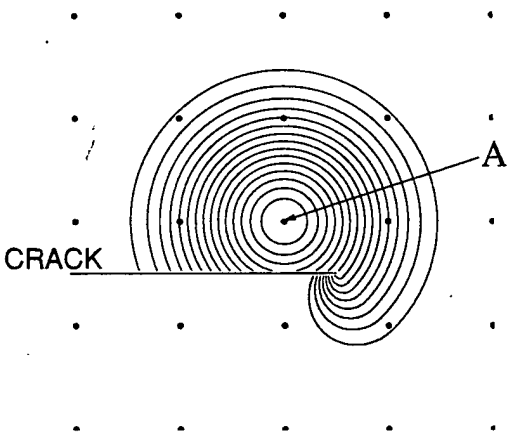

(c) Weight function for $\lambda = 2$.

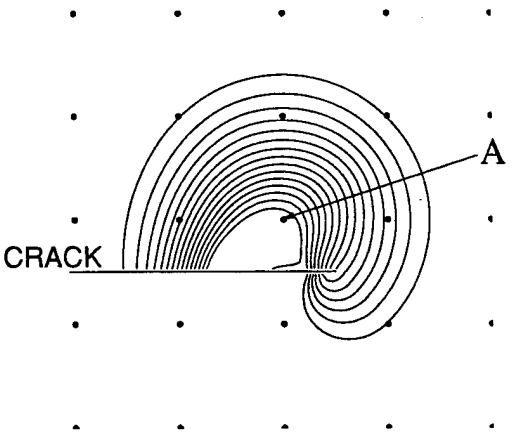

(d) Shape function for $\lambda = 2$.

Figure 12: Contours for weight and shape functions associated with node A near a crack tip constructed using the *diffraction method.* The quartic weight function in (1b) is used with $d_{max} = 2.01$.

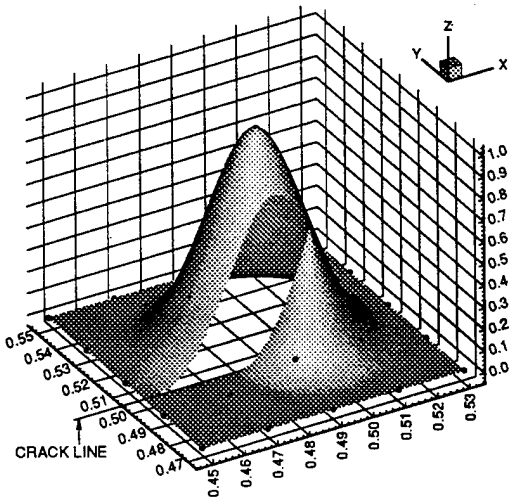

(a) Weight function associated with node A in Fig. 12a.

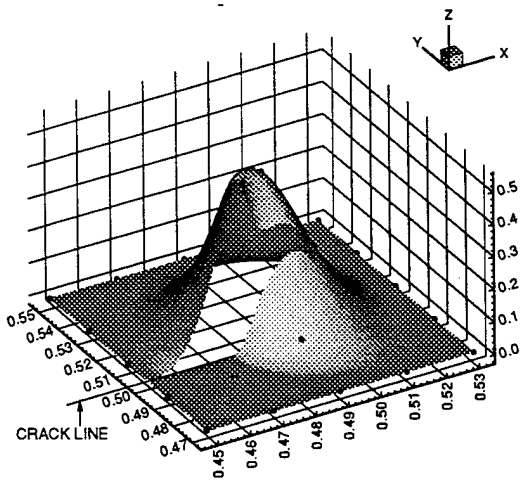

(b) Shape function associated with node A in Fig. 12b.

Figure 13: Surface plots for weight and shape functions near a crack tip constructed using the *diffraction method* with $\lambda = 1$. The quartic weight function in (1b) is used with $d_{max} = 2.01$.

where

$$\frac{\partial s_0}{\partial x_i} = \frac{x_i - x_{I_i}}{s_0} \qquad \text{and} \qquad \frac{\partial s_2}{\partial x_i} = \frac{x_i - x_{c_i}}{s_2}.$$

The diffraction method works well for general nonconvex boundaries as well. Consider the case shown in Fig. 11b where the line between a node and a sampling point intersects the boundary of a hole. The tangent point between the node and the nonconvex boundary is used as the wrap-around point, $\mathbf{x}_c$, and Eq. (29) used to compute the weight function distance, d_I (see Fig. 11b). Note that for this implementation of the diffraction method, the segment $d_2(\mathbf{x})$ intersects the boundary. This should not be a cause for alarm because with adequate refinement this effect is quite negligible. As is shown in Section 4.4, acceptable results can be obtained when the smooth boundary is considered fully transparent.

4.3 Transparency Method

Another technique for constructing continuous approximations is the *transparency* method (Organ, Fleming, and Belytschko, 1996; Belytschko, Krongauz, Fleming, Organ, and Liu, 1996), which will be described here for cracks. The underlying concept of this method is to endow the crack tip with a varying measure of transparency such that it is completely transparent at the tip and becomes completely opaque a short distance behind the tip. In this way, the field of vision for a node near the crack tip is not abruptly truncated when it reaches the crack tip, but rather diminishes smoothly to zero a short distance behind the tip of the crack.

When a ray passes between a node $\mathbf{x}_I$ and a sampling point $\mathbf{x}$, and crosses the crack as shown in Fig. 14, the distance parameter d_I in the weight function is modified (lengthened) by the following:

$$d_I(\mathbf{x}) = s_0(\mathbf{x}) + d_{mI}\left(\frac{s_c(\mathbf{x})}{\bar{s}_c}\right)^{\lambda}, \quad \lambda \geq 2, \tag{32}$$

where $s_0(\mathbf{x}) = \|\mathbf{x} = \mathbf{x}_I\|$, d_{mI} is the radius of support for node I, and $s_c(\mathbf{x})$ is the intersection distance behind the crack tip. The parameter $\bar{s}_c$ sets the distance behind the crack tip at which complete opacity occurs:

$$\bar{s}_c = \kappa h, \tag{33}$$

where h is the nodal spacing and κ is a constant, usually $0 < \kappa < 1$.

The spatial derivatives of the distance parameter, d_I, obtained by the chain rule, are

$$\frac{\partial d_I}{\partial x_i} = \frac{\partial s_0}{\partial x_i} + \lambda d_{mI}\frac{s_c^{\lambda-1}}{\bar{s}_c^{\lambda}}\frac{\partial s_c}{\partial x_i}, \tag{34}$$

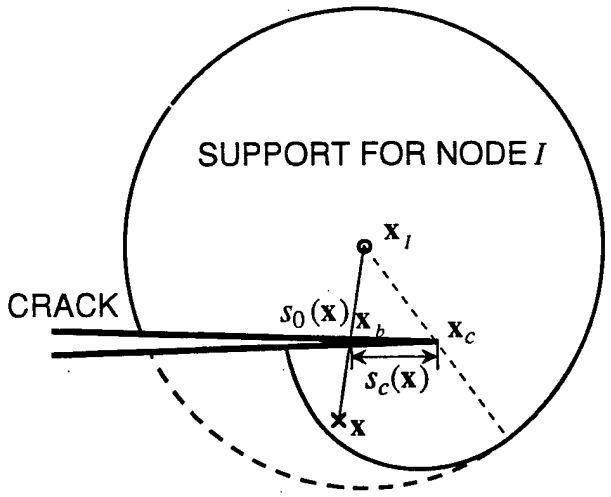

Figure 14: Transparency method for computing smooth weight functions.

where

$$\frac{\partial s_0}{\partial x_i} = \frac{x_i - x_{I_i}}{s_0},$$

$$\frac{\partial s_c}{\partial x_1} = -\cos\theta = \frac{x_b - x_c}{s_c} \qquad \text{and} \qquad \frac{\partial s_c}{\partial x_2} = -\sin\theta = \frac{y_b - y_c}{s_c},$$

where θ is the angle between the crack and the x-axis and $\mathbf{x}_b$ is the intersection point behind the crack tip.

Contour plots of the weight and shape functions near a crack tip constructed by the transparency method are shown in Fig. 15 and surface plots are shown in Fig. 16. Note that the functions are continuous at the crack tip.

One drawback of the transparency method is that it does not work well when nodes are placed too close to the crack surface. Fig. 17 shows a surface plot of a shape function constructed by the transparency method when nodes are placed along the crack surface. Note the trough which appears in the shape function ahead of the crack. This trough appears because although the crack tip is transparent for this node, the change in the degree of transparency with respect to the change in angle is very sharp, i.e., $s_c(\mathbf{x})$ in Eq. (32) increases rapidly. There is no discontinuity in the shape function, only a small dip in the shape function. To circumvent this problem in the transparency method, a restriction has been placed on the position of the nodes. All nodes should be placed so that the normal distance from the node to the crack surface is greater than roughly $1/4h$, where h is the nodal spacing.

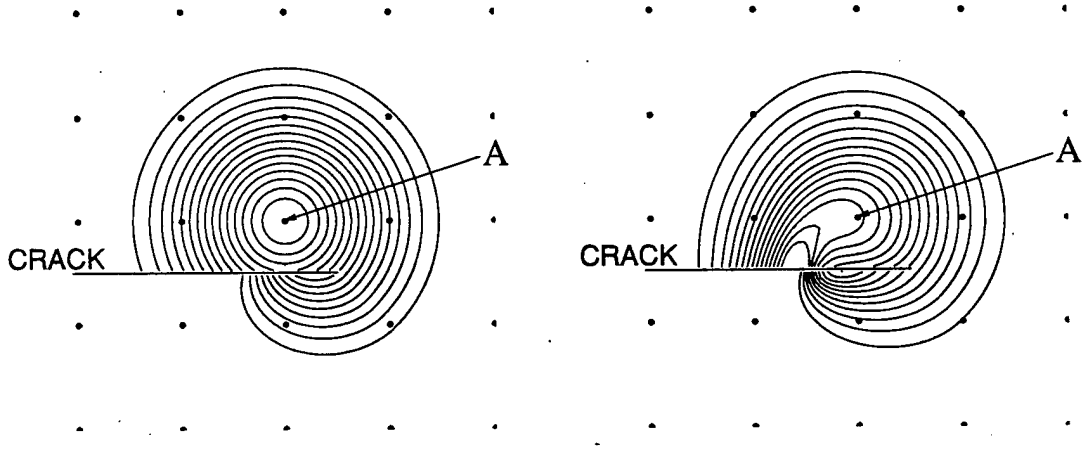

(a) Weight function for $\kappa = 1.0$.

(b) Shape function for $\kappa = 1.0$.

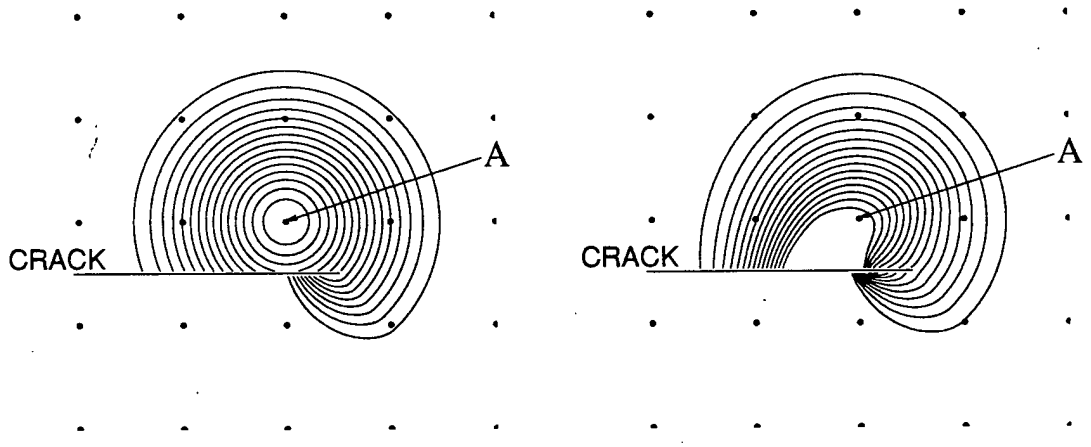

(c) Weight function for $\kappa = 0.5$.

(d) Shape function for $\kappa = 0.5$.

Figure 15: Contours for weight and shape functions associated with node A near a crack tip constructed using the *transparency method.* The quartic weight function in (1b) is used with $d_{max} = 2.01$.

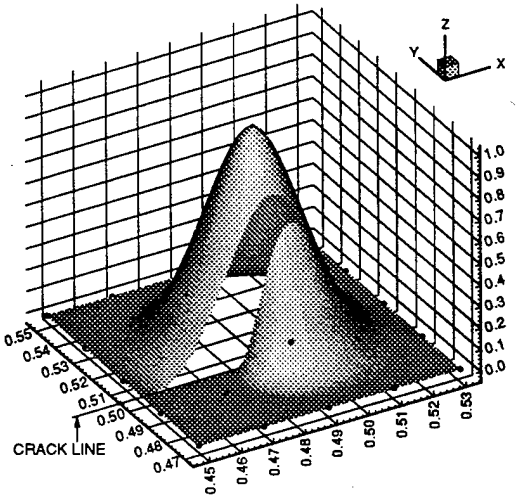

(a) Weight function associated with node A in Fig. 15a.

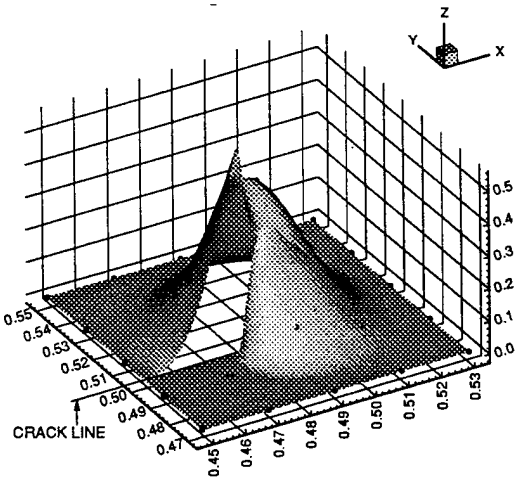

(b) Shape function associated with node A in Fig. 15b.

Figure 16: Surface plots for weight and shape functions near a crack tip using the *transparency method* with $\kappa = 1.0$. The quartic weight function in (1b) is used with $d_{max} = 2.01$.

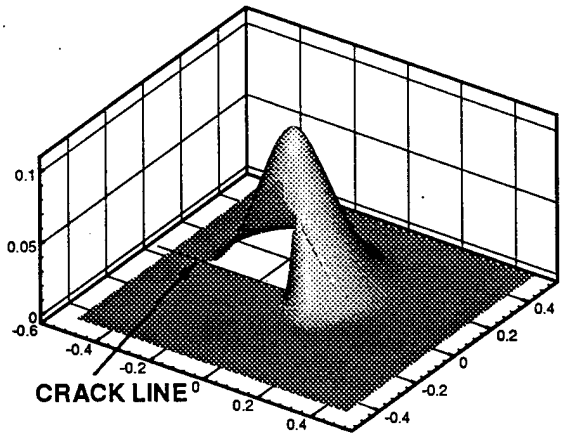

Figure 17: Surface plot for shape function using the transparency method ($\kappa = 1$) when nodes are placed too close to the crack surface.

4.4 "See-through" Method

Terry (1994) constructed a smooth approximation near nonconvex boundaries using a "*see-through*" method in which all or part of the curved boundary is made completely transparent. Terry (1994) found that better accuracy is obtained for a problem with an interior hole when the boundary of the hole was not strictly enforced by the visibility criterion.

Duarte and Oden (1996b) and (Krysl and Belytschko, 1996) suggested a smoothing technique in which the crack was completely transparent if the crack tip is within the domain of influence of a node. This is also called the *continuous line criterion*: if a continuous line connecting the node to a point lies entirely withing the domain of influence of the node, the point is visible. While this technique is easy to implement and provides smooth approximations, it effectively shortens the crack and leads to inaccurate solutions (see Fig. 18). One situation in which this method does work for cracks is when the enrichment techniques from Chapter 5 are used. In this case, the approximation function near the crack tip is strong enough to yield correct crack opening displacements.

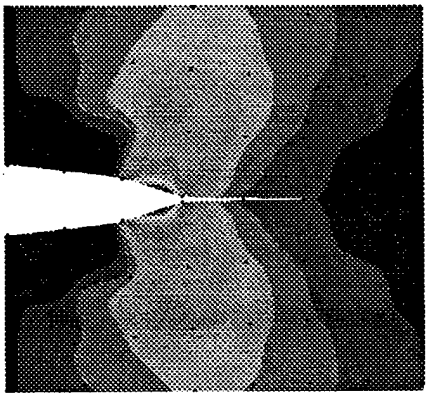

Figure 18: Crack opening displacement and Mises stress contours when using the "*see-through*" method ($d_{max} = 2$). The dots are the nodal locations and the contours are generated using values at the integration points.

4.5 Numerical Examples

Two problems are presented here to illustrate the performance of the smoothing techniques for nonconvex boundaries. The EFG method is used for numerical computations and a background element mesh is used for integrating the weak form.

4.5.1 Infinite plate with a hole

An infinite plate with a hole subjected to a remote unit traction in the x-direction is solved and the solutions are compared for the visibility, diffraction, and "see-through" methods. The solution of this problem is given in Timoshenko and Goodier (1970) as:

$$\sigma_{xx} = 1 - \frac{a^2}{r^2}\left(\frac{3}{2}\cos(2\theta) + \cos(4\theta)\right) + \frac{3a^4}{2r^4}\cos(4\theta), \tag{35a}$$

$$\sigma_{yy} = -\frac{a^2}{r^2}\left(\frac{1}{2}\cos(2\theta) - \cos(4\theta)\right) - \frac{3a^4}{2r^4}\cos(4\theta), \tag{35b}$$

$$\sigma_{xy} = -\frac{a^2}{r^2}\left(\frac{1}{2}\sin(2\theta) + \sin(4\theta)\right) + \frac{3a^4}{2r^4}\sin(4\theta), \tag{35c}$$

where a is the radius of the hole.

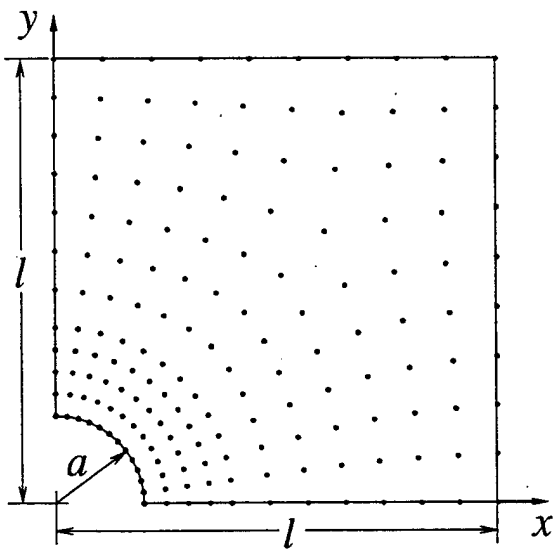

Figure 19: Typical mesh for the infinite plate with a hole problem. Due to symmetry, only a quarter mesh is modeled.

A finite model of the problem is constructed by applying the exact tractions corresponding to Eq. (35) on the boundaries; due to symmetry, only a quarter of the plate is modeled (see Fig. 19). The dimensions used are $a = 1.0$ in., $l = 5.0$ in.; plane strain, linear elastic conditions are assumed with Young's modulus and Poisson's ratio, $E = 30 \times 10^6$ psi and $\nu = 0.3$, respectively. A typical nodal arrangement is shown in Fig. 19. The EFG meshes were graded with additional refinement around the hole up to a radius of $2a$; a typical mesh is shown in Fig. 19. The integration cells coincided with the nodal arrangement; 9×9 Gauss quadrature is used in the graded region, with 5×5 quadrature in the remaining cells; for the simulations by the diffraction method, $\lambda = 2$.

According to the analytic solution in Eq. (35a), the hole acts as a stress raiser with a stress concentration factor of 3 at $(x, y) = (0, a)$. The numerical solution captures the stress concentration well for smaller support sizes (see Fig. 20), but the accuracy deteriorates for larger support sizes when shape functions are discontinuous. The errors in the stress concentration using the visibility criterion at large d_{max} can be traced to oscillations in the stress distribution, as shown along the line $x = 0$ in Fig. 21.

The error in energy as a function of the domain of influence is plotted in Fig. 22, where the exact solution is computed from the solution given in Timoshenko and

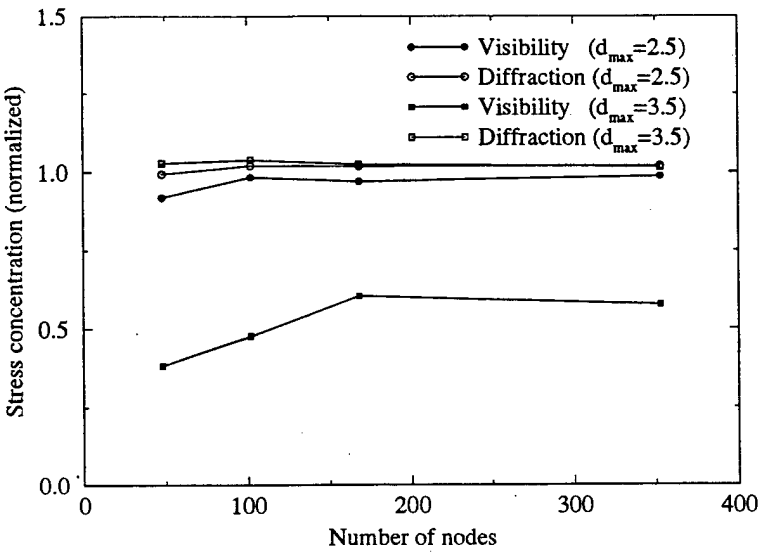

Figure 20: Convergence of the stress concentration at the hole versus the number of nodes.

Goodier (1970), and the energy norm is computed by

$$\text{energy norm} = \left[\frac{1}{2}\int_{\Omega}(\boldsymbol{\sigma}-\boldsymbol{\sigma}^h):(\boldsymbol{\epsilon}-\boldsymbol{\epsilon}^h)d\Omega\right]^{1/2}. \tag{36}$$

The results again show that for smaller domains of influence, there are no significant differences in accuracy between the discontinuous and the smooth approximation functions; however, as the domain of influence is increased, the error increases for the discontinuous shape functions. On the other hand, both accuracy and convergence rate increase for the smooth shape functions as d_{max} increases (see Fig. 23).

4.5.2 Mode 1 static fracture

A near-tip crack problem is studied for the effects of smoothing the approximation for crack problems and shows the improvements in accuracy when using the EFG enrichment techniques from Section 5.

For the numerical model, the asymptotic mode 1 displacement field in Eqs. (60) is applied to the boundaries of an EFG mesh, with the stress intensity factor prescribed as $k_1 = 1$ psi$\sqrt{\text{in}}$. The mesh dimensions are $2a \times 2a$, with a crack of length a oriented such that the crack tip was located at the center as in Fig. 24. Numerical results are

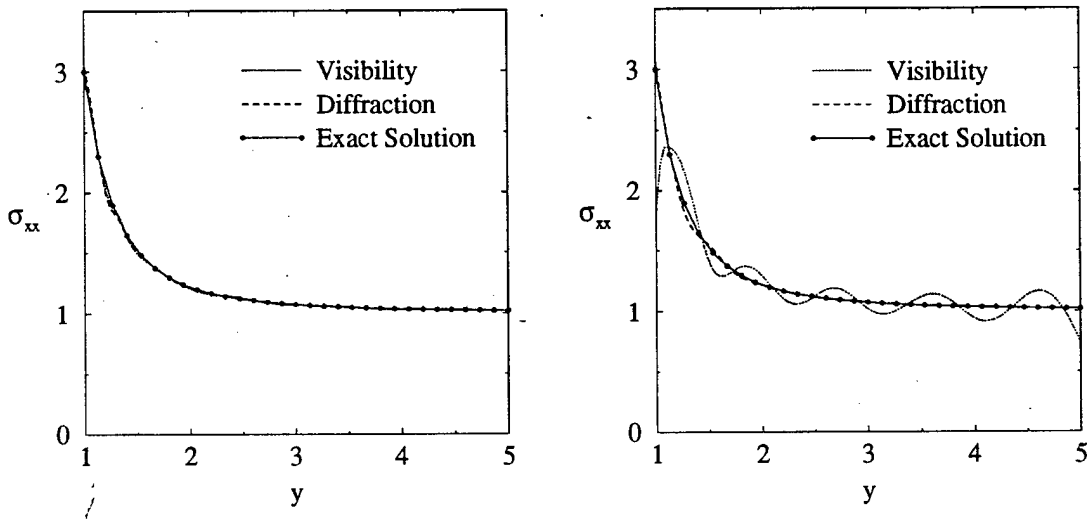

(a) $d_{max} = 2.5$ (b) $d_{max} = 3.5$

Figure 21: Stress distribution along $x = 0$ for a mesh with 168 nodes shown in Fig. 19.

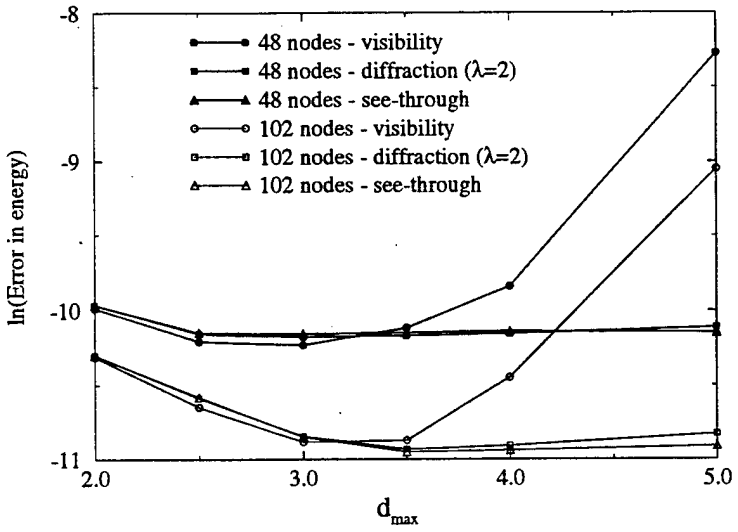

Figure 22: Error in energy versus the support size d_{max} for the infinite plate with a hole problem.

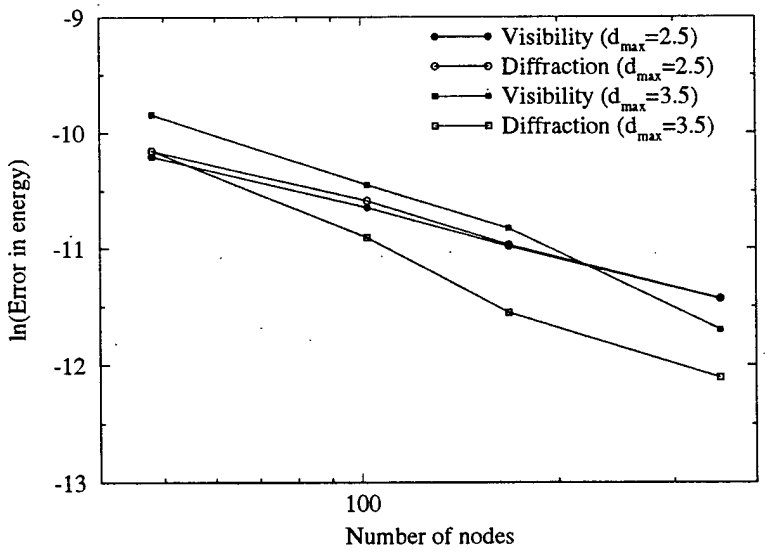

Figure 23: Convergence of the error in energy versus the number of nodes for the infinite plate with a hole problem.

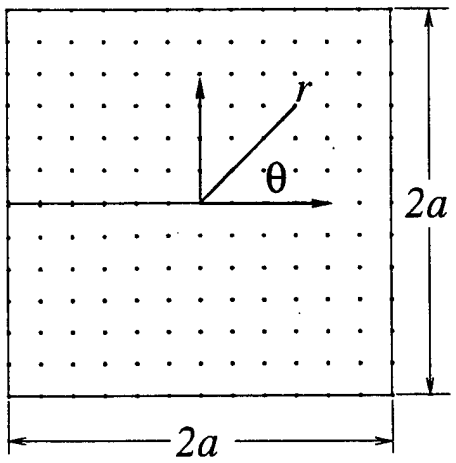

Figure 24: Typical mesh for the mode 1 fracture problem.

presented for both a linear basis and an intrinsically enriched basis from Eq. (50). In addition, the effects of local crack tip refinement are investigated.

Fig. 25a shows the circumferential distribution of the displacement; note the discontinuities near the crack tip for shape functions based on the visibility criterion. These discontinuities occur at fixed angles and vanish away from the crack tip. In other words, the discontinuities occur on rays from the nodes to the crack tip; the weight functions associated with those nodes are discontinuous along these rays. Krysl and Belytschko (1996) have shown that the solution is still convergent due to the local nature of the discontinuities.

One drawback of the smooth approximations is that the computed crack opening profile is not parabolic at the tip. The shape functions wrap around the crack tip and the crack is effectively shortened if the smoothing effect is too large or the mesh is too coarse, leading to the crack opening displacement (COD) shown in Fig. 26a. The maximum stress is then not at the crack tip, but is shifted a small distance that depends on the mesh refinement. This effect can be reduced by increasing λ in the diffraction method, or decreasing κ in the transparency method. When the mesh is refined locally as in Fig. 26b or an enriched approximation is used as in Fig. 26c, the maximum stress shifts to the crack tip and the COD profile becomes parabolic.

Smooth approximations provide substantial benefits when using an enriched approximation. Fig. 27 shows the error in energy in (36) plotted as a function of

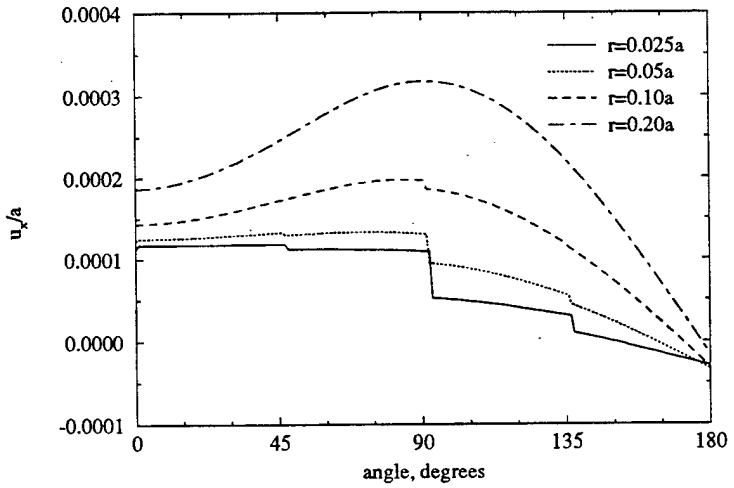

(a) Discontinuous, visibility criterion.

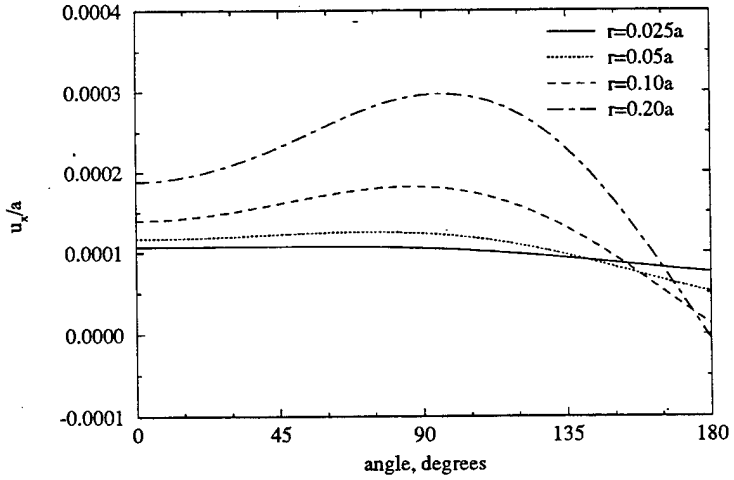

(b) Continuous, diffraction method.

Figure 25: Angular variation of displacement around the crack tip at various radial distances. The jumps at 45°, 90°, and 135° in (a) occur due to the discontinuous shape functions generated by the *visibility criterion.*

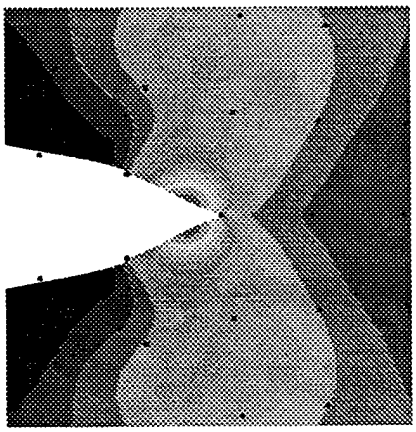

(a) Uniform mesh (linear basis).

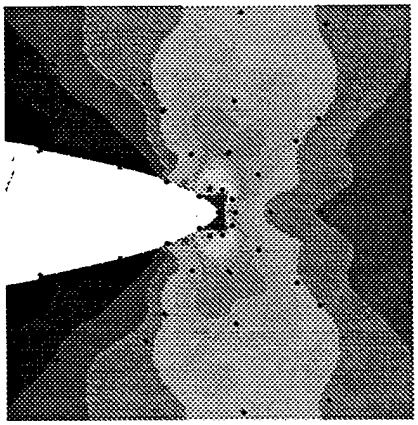

(b) Refinement at crack tip (linear basis).

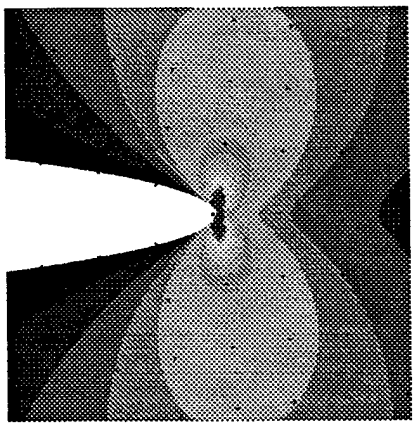

(c) Uniform mesh (enriched basis)

Figure 26: Crack opening displacement and Mises stress contours for a mode 1 fracture problem using the *diffraction method* ($\lambda = 1$). The dots are nodal locations and the contours are generated using values at the integration points.

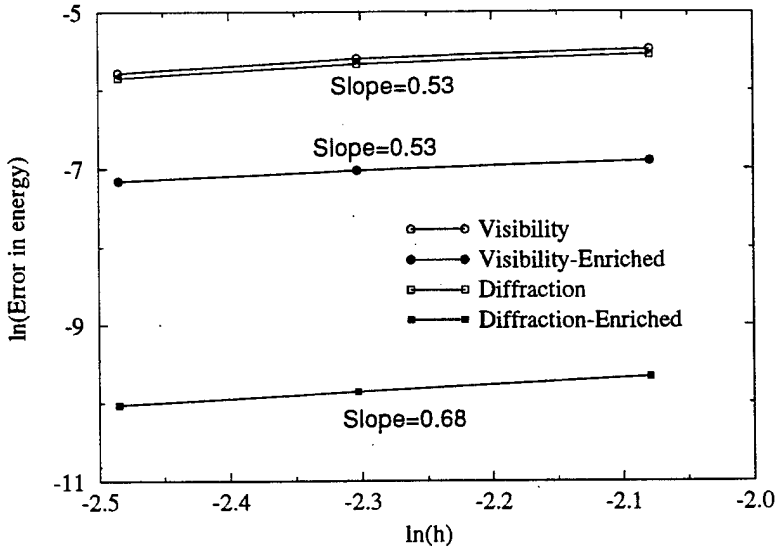

Figure 27: Convergence of the error in energy for the mode 1 crack problem. For the diffraction method, $\lambda = 2$.

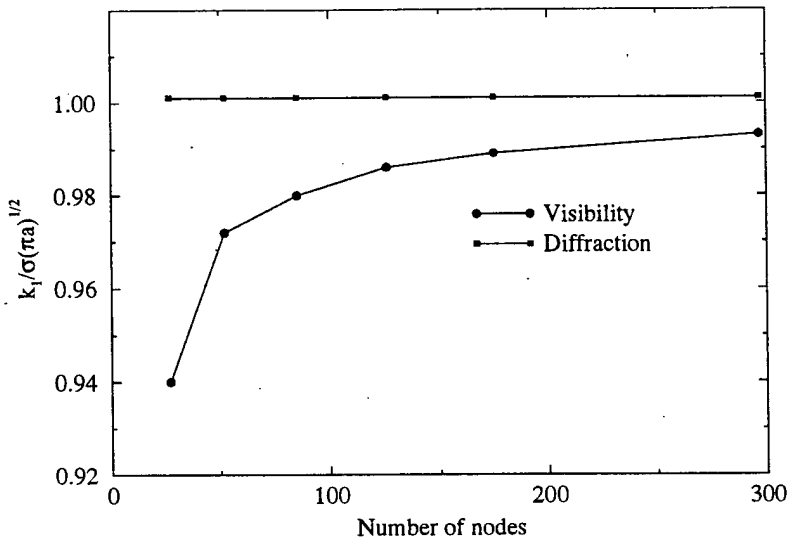

Figure 28: Convergence of the mode 1 stress intensity factor using the enriched basis. For the diffraction method, $\lambda = 2$.

uniform nodal refinement for both linear and enriched bases with the discontinuous and smooth approximations. The results are nearly identical for continuous and discontinuous approximations with a linear basis because oscillations are the dominant source of error. The enriched basis reduces oscillations, so discontinuities in the shape functions become a noticeable source of error. Fig. 28 shows the convergence of the mode 1 stress intensity factor using the enriched basis. The stress intensity factor was computed using the J integral in domain form (Moran and Shih, 1987). For the discontinuous shape functions, the stress intensity factor is low by as much as 6% for a coarse mesh, but improves as the mesh is refined. For the smooth approximations, the stress intensity factor is within 0.1% for all meshes.

As stated previously, in spite of the discontinuities due to the visibility criterion, the approximation is still convergent. Figs. 29 show four levels of increasing nodal refinement surrounding the crack tip. Fig. 30a shows the error in energy using a linear basis plotted as a function of the number of nodes added to the crack tip region and Fig. 30b shows the corresponding stress intensity factors for those levels of refinement. It is readily seen that as under these circumstances the discontinuous approximations do not degrade the accuracy compared to the smooth approximations for either total error or stress intensity factor. In addition, the smooth approximations generated by the "see-through" method are greatly in error, leading to the conclusion that these approximations should not be used in conjunction with sharp nonconvex boundaries such as cracks. It should also be noted that over-refinement of the crack tip region can actually lead to an increase in error if the mesh away from the crack tip is not refined. Fig. 30a shows that for the highest level of refinement in Fig. 29d, the error actually increases slightly over the previous refinement. As a general rule for meshless methods, a sharp gradient in nodal spacing leads to error. A likely source of this error is that nodes in the coarse region will have domains of influence which extend into the refined region while the converse is not true.

5 Enrichment of EFG for Crack Tip Fields

Finite element methods have reached a high degree of effectiveness in analysis of stationary cracks. A large variety of approaches have evolved, such as direct application of standard elements, singular crack tip elements, and enriched elements. While direct application of standard elements is the most straightforward, a high degree of mesh refinement is required near the crack tip to capture the singular stress fields. Singular crack tip elements can achieve high accuracy in linear elastic fracture mechanics without extremely refined meshes. The most popular of these elements is the quarter-point element (Henshell and Shaw, 1975; Barsoum, 1977; Banks-Sills and Bortman, 1984) which introduced a singularity in the Jacobian of an 8-node serendip-

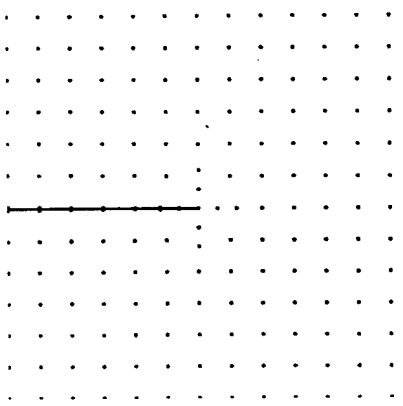

(a) 2 rings, 5 nodes/ring

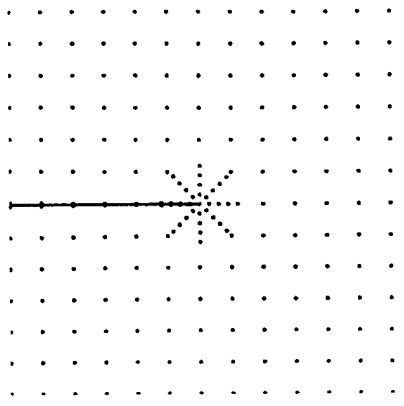

(b) 4 rings, 9 nodes/ring

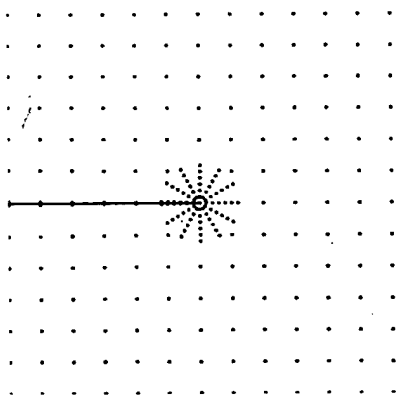

(c) 6 rings, 13 nodes/ring

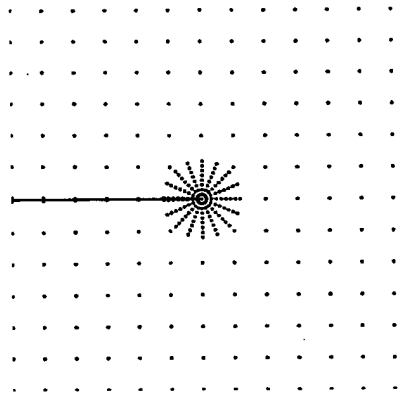

(d) 8 rings, 17 nodes/ring

Figure 29: Four levels of nodal refinement using a star-shaped nodal array at the crack tip.

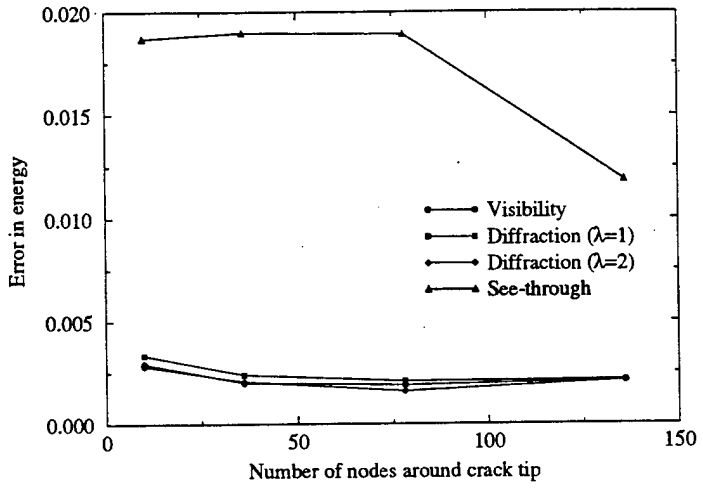

(a) Error in energy

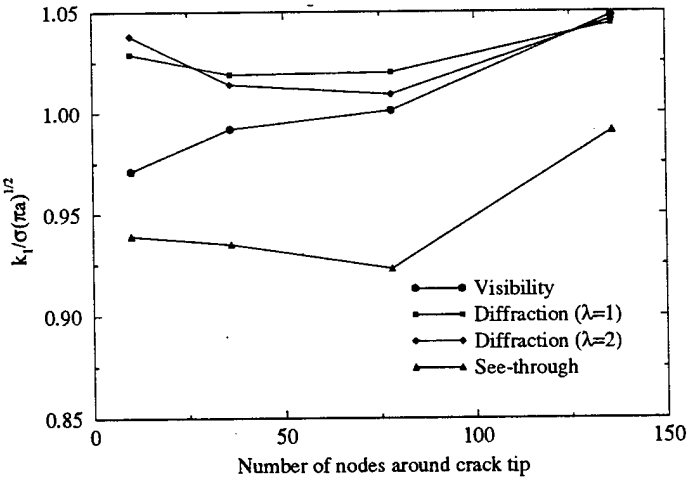

(b) Stress intensity factors

Figure 30: Energy error and stress intensity factors with four crack tip nodal refinements. All calculations were made with a linear basis and Gaussian weight function ($d_{max} = 2.5, \alpha = 0.625$).

ity element by moving the mid-side node on the sides connected to the crack tip to the quarter-point. Akin (1976) presented an element in which the shape function at the crack tip node is modified so it possesses singular derivatives of the correct order.

Another method of capturing the singular stress fields in finite elements is to enrich isoparametric finite elements by including the near tip fields in the trial functions (Benzley, 1974; Gifford and Hilton, 1978). The advantage of these elements is that the stress intensity factors can be computed directly as part of the solution. However, the results of elements enriched by singular fields are quite sensitive to their size, and do not exhibit uniform convergence. In addition, these elements are cumbersome to implement because the stiffness matrix and force vector have to be expanded to account for the extra unknowns, the stress intensity factors. Transition elements are needed because these enriched elements are generally not compatible with standard elements.

In applications of EFG or meshless methods, special techniques have been developed for incorporating the singular functions associated with elastostatic fracture as an alternative to large arrays of nodes at the crack tip; the latter can be expensive and awkward for problems with complex geometry. It was found that the incorporation of the singular fields in a meshless method is substantially simpler and more trouble-free than in finite element methods.

Enrichment of a meshless method may be carried out extrinsically or intrinsically. Extrinsic enrichment consists of adding an enrichment function to the trial function. For intrinsic enrichment, the enrichment functions are included in the EFG basis, so that no additional unknowns are needed in the final system of equations.

In this section, extrinsic and intrinsic enrichment techniques are presented for meshless methods. In Sections 5.1 and 5.2, two methods of extrinsic enrichment are presented and discussed. Section 5.3 presents intrinsic enrichment. Techniques for coupling enriched and linear approximations are discussed in Section 5.4 and a mapping for kinked cracks is given in Section 5.5. Numerical results are shown in Section 5.6. In addition, two degrees of enrichment are discussed: 1) full enrichment by all linearly independent functions of the asymptotic near-tip field, and 2) radial enrichment consisting of only the $\sqrt{r}$ field.

5.1 Extrinsic MLS Enrichment

In extrinsic enrichment of a meshless approximation, a function closely related to the solution is added to the polynomial expansion of MLS, Eq. (4). For example, in linear elastic fracture mechanics, the near tip asymptotic field or its constituents can

be added. The approximation takes the form

$$u^h_\alpha(\mathbf{x}) = \mathbf{p}^T(\mathbf{x})\mathbf{a}_\alpha(\mathbf{x}) + \sum_{j=1}^{n_c}[k^j_1 Q^j_{1\alpha}(\mathbf{x}) + k^j_2 Q^j_{2\alpha}(\mathbf{x})] \qquad \alpha = 1,2 \tag{37}$$

where $u^h_\alpha(\mathbf{x})$ denotes the approximation for $u_\alpha(\mathbf{x})$, $\mathbf{p}(\mathbf{x})$ is a complete polynomial basis in the spatial coordinates, n_c is the number of cracks in the model, $\mathbf{a}_\alpha(\mathbf{x})$ are the coefficients of the polynomial basis; k^j_1 and k^j_2 are global unknowns associated with crack j. Lower case Greek subscripts have a range of 2 and refer to Cartesian components. Some complete bases are given in Eqs. (5).

The functions $Q_{1\alpha}(\mathbf{x})$ and $Q_{2\alpha}(\mathbf{x})$, which describe the near-tip displacement field for an elastic crack, are (Williams, 1957; Anderson, 1991)

$$Q_{11}(\mathbf{x}) = \frac{1}{2\mu}\sqrt{\frac{r}{2\pi}}\cos\left(\frac{\theta}{2}\right)\left[\kappa - 1 + 2\sin^2\left(\frac{\theta}{2}\right)\right] \tag{38a}$$

$$Q_{12}(\mathbf{x}) = \frac{1}{2\mu}\sqrt{\frac{r}{2\pi}}\sin\left(\frac{\theta}{2}\right)\left[\kappa + 1 - 2\cos^2\left(\frac{\theta}{2}\right)\right] \tag{38b}$$

$$Q_{21}(\mathbf{x}) = \frac{1}{2\mu}\sqrt{\frac{r}{2\pi}}\sin\left(\frac{\theta}{2}\right)\left[\kappa + 1 + 2\cos^2\left(\frac{\theta}{2}\right)\right] \tag{38c}$$

$$Q_{22}(\mathbf{x}) = -\frac{1}{2\mu}\sqrt{\frac{r}{2\pi}}\cos\left(\frac{\theta}{2}\right)\left[\kappa - 1 - 2\sin^2\left(\frac{\theta}{2}\right)\right] \tag{38d}$$

where r is the distance from the crack tip, θ is the angle from the tangent to the crack path at the crack tip (see Fig. 31), μ is the shear modulus and κ the Kolosov constant defined as

$$\kappa = \begin{cases} 3 - 4\nu & \text{plane strain} \\ (3-\nu)/(1+\nu) & \text{plane stress.} \end{cases}$$

The coefficients, $\mathbf{a}_\alpha(\mathbf{x})$, are functions of the spatial coordinates and are determined by the MLS methodology in Section 2. However, additional terms arise from the inclusion of the near-tip field and so the MLS formulation will be rederived here in the interest of completeness. A weighted, discrete $\mathcal{L}_2$ norm is written

$$J = \sum_{I=1}^{n} w(\mathbf{x} - \mathbf{x}_I)\left[\mathbf{p}^T(\mathbf{x}_I)\mathbf{a}_\alpha(\mathbf{x}) + \sum_{j=1}^{n_c}[k^j_1 Q^j_{1\alpha}(\mathbf{x}_I) + k^j_2 Q^j_{2\alpha}(\mathbf{x}_I)] - u_{I\alpha}\right]^2, \tag{39}$$

where n is the number of points in the neighborhood of $\mathbf{x}$ for which the weight function, $w(\mathbf{x} - \mathbf{x}_I)$, is non-zero, and $u_{I\alpha}$ is the α component of the nodal value at

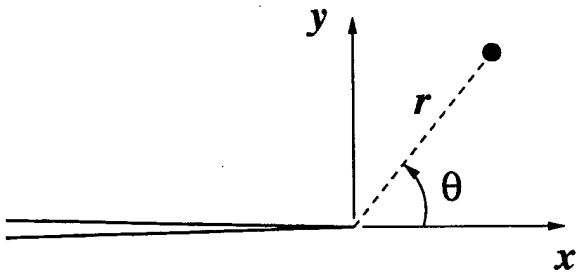

Figure 31: Local coordinate system at crack tip.

$\mathbf{x}_I$. The stationarity of J with respect to $\mathbf{a}_\alpha(\mathbf{x})$ leads to

$$\mathbf{A}(\mathbf{x})\mathbf{a}_\alpha(\mathbf{x}) = \sum_{I=1}^{n} \mathbf{C}_I(\mathbf{x}) \left\{ u_{I\alpha} - \sum_{j=1}^{n_c} [k_1^j Q_{1\alpha}^j(\mathbf{x}_I) + k_2^j Q_{2\alpha}^j(\mathbf{x}_I)] \right\} \tag{40}$$

where

$$\mathbf{A}(\mathbf{x}) = \sum_{I=1}^{n} w(\mathbf{x} - \mathbf{x}_I)\mathbf{p}(\mathbf{x}_I)\mathbf{p}^T(\mathbf{x}_I) \tag{41}$$

$$\mathbf{C}_I(\mathbf{x}) = w(\mathbf{x} - \mathbf{x}_I)\mathbf{p}(\mathbf{x}_I)\,. \tag{42}$$

It should be noted that k_1^j and k_2^j are global parameters in this method and they are considered fixed in the process of obtaining the parameters $\mathbf{a}_\alpha$ for the local fit.

Solving Eq. (40) for $\mathbf{a}_\alpha(\mathbf{x})$ gives

$$\mathbf{a}_\alpha(\mathbf{x}) = \sum_{I=1}^{n} \mathbf{A}^{-1}(\mathbf{x})\mathbf{C}_I(\mathbf{x}) \left\{ u_{I\alpha} - \sum_{j=1}^{n_c} [k_1^j Q_{1\alpha}^j(\mathbf{x}_I) + k_2^j Q_{2\alpha}^j(\mathbf{x}_I)] \right\}. \tag{43}$$

Expressing Eq. (37) in terms of the nodal parameter $u_{I\alpha}$ and the enriched field pa-

rameters k_1^j and k_2^j yields

$$u_\alpha^h(\mathbf{x}) = \sum_{I=1}^{n} \phi_I(\mathbf{x}) \left\{ u_{I\alpha} - \sum_{j=1}^{n_c} [k_1^j Q_{1\alpha}^j(\mathbf{x}_I) + k_2^j Q_{2\alpha}^j(\mathbf{x}_I)] \right\} + \sum_{j=1}^{n_c} [k_1^j Q_{1\alpha}^j(\mathbf{x}) + k_2^j Q_{2\alpha}^j(\mathbf{x})] \tag{44a}$$

$$u_\alpha^h(\mathbf{x}) = \sum_{I=1}^{n} \phi_I(\mathbf{x}) u_{I\alpha} + \sum_{j=1}^{n_c} k_1^j \left[Q_{1\alpha}^j(\mathbf{x}) - \sum_{I=1}^{n} \phi_I(\mathbf{x}) Q_{1\alpha}^j(\mathbf{x}_I) \right] + \sum_{j=1}^{n_c} k_2^j \left[Q_{2\alpha}^j(\mathbf{x}) - \sum_{I=1}^{n} \phi_I(\mathbf{x}) Q_{2\alpha}^j(\mathbf{x}_I) \right] \tag{44b}$$

where the shape function, $\phi_I(\mathbf{x})$, is defined as

$$\phi_I(\mathbf{x}) = \mathbf{p}^T(\mathbf{x}) \mathbf{A}^{-1}(\mathbf{x}) \mathbf{C}_I(\mathbf{x}) . \tag{45}$$

These shape functions are identical to those defined in Eq. (10) and are capable of representing the smooth part of the solution. Eq. (44a) will be written as

$$u_\alpha^h(\mathbf{x}) = \sum_{I=1}^{n} \phi_I(\mathbf{x}) \tilde{u}_{I\alpha} + \sum_{j=1}^{n_c} [k_1^j Q_{1\alpha}^j(\mathbf{x}) + k_2^j Q_{2\alpha}^j(\mathbf{x})], \tag{46}$$

where the modified nodal coefficients, $\tilde{u}_{I\alpha}$, are

$$\tilde{u}_{I\alpha} = u_{I\alpha} - \sum_{j=1}^{n_c} [k_1^j Q_{1\alpha}^j(\mathbf{x}_I) + k_2^j Q_{2\alpha}^j(\mathbf{x}_I)]. \tag{47}$$

Note that the enriched finite element formulation given by Benzley (1974) and Gifford and Hilton (1978) is the same as Eq. (44b). This form is advantageous in finite elements, but not necessary in a meshless method. Using the approximation in Eq. (46) is simpler to implement and computationally faster because the terms $\sum_{I=1}^{n} \phi_I(\mathbf{x}) k_1^j Q_{1\alpha}^j(\mathbf{x}_I)$ and $\sum_{I=1}^{n} \phi_I(\mathbf{x}) k_2^j Q_{2\alpha}^j(\mathbf{x}_I)$ are not subtracted at each sampling point.

5.2 Extrinsic PU enrichment

Extrinsic enrichment of meshless methods can be carried out using partition of unity (PU) methods (Duarte and Oden, 1996b; Melenk and Babuška, 1996; Belytschko,

Krongauz, Organ, Fleming, and Krysl, 1996). In this method, the approximation is augmented by enrichment functions added extrinsically to the existing EFG approximation from Eq. (11). This basis can consist of higher order polynomials or, for linear elastic fracture problems, terms from the asymptotic near tip field can be used. The extrinsic basis is smoothly added to the existing approximation by multiplying it by a partition of unity.

The essential element of this method is the construction of a partition of unity, which can be obtained by the MLS methodology (see Section 2). A partition of unity $\phi(\mathbf{x})^k$, constructed from a complete polynomial basis of order k, is a local approximation for which

$$\sum_{I=1}^{n} \phi_I(\mathbf{x}) = 1\,. \tag{48}$$

It can easily be seen that MLS approximations are partitions of unity since Eq. (48) is the reproducing condition for a constant, which MLS approximations must satisfy (see Belytschko, Krongauz, Fleming, Organ, and Liu (1996)).

Approximations based on partitions of unity take the form

$$u^h(\mathbf{x}) = \sum_{I=1}^{n} \phi_I^k(\mathbf{x}) u_I + \sum_{I=1}^{n} \sum_{i=1}^{m_e} \phi_I^k(\mathbf{x}) b_{Ii} q_i(\mathbf{x}) \tag{49}$$

where u_I and b_{Ii} are nodal coefficients, and n is the number of neighbors of point $\mathbf{x}$. The vector $\mathbf{q}(\mathbf{x})$ is called the extrinsic basis and is of length m_e. For enriching linear elastic fracture problems, this basis can contain the $\sqrt{r}$ radial dependence or the $\sqrt{r}$ radial and angular θ dependence which spans Eq. (38). A superscript k is added to the shape functions ϕ_I in the approximation to denote the polynomial order of the basis used in forming the partition of unity. It is sometimes convenient to construct the partitions of unity using Shepard functions (i.e., $k = 1$) which satisfy constant consistency and add the terms to satisfy linear and higher order consistency to the extrinsic PU basis.

PU methods appear to provide a vehicle for local enrichment. The partition of unity, $\phi_I(\mathbf{x})^k$, can be formed from a linear basis ($k = 2$), which yields linear consistency. Enrichment of the approximation may be carried out locally by adding the known form of the solution to the extrinsic basis, $\mathbf{q}(\mathbf{x})$, at nodes in the region in which it is needed. It should be noted that the enrichment should be added to each node whose domain of influence extends into the region to be enriched.

5.3 Intrinsic Basis Enrichment

Meshless approximations can be intrinsically enriched by including a special functions in the basis (Fleming, Chu, Moran, and Belytschko, 1997). For example, in fracture

mechanics, one can include the asymptotic near-tip displacement field in Eqs. (38), or an important ingredient such as $\sqrt{r}$. The choice of functions depends on the coarse-mesh accuracy desired. For higher accuracy, include the full asymptotic field from (38), while for higher speed at some cost of accuracy, only the $\sqrt{r}$ function can be included in the basis. Both methods are described in the subsequent sections.

5.3.1 Full enrichment

In full intrinsic enrichment of EFG approximations for fracture problems, the entire near-tip asymptotic displacement field is included in the basis. Following some trigonometric manipulation, it can be shown that all the functions in Eqs. (38) are spanned by the basis

$$\mathbf{p}^T(\mathbf{x}) = \left[1, x, y, \sqrt{r}\cos\frac{\theta}{2}, \sqrt{r}\sin\frac{\theta}{2}, \sqrt{r}\sin\frac{\theta}{2}\sin\theta, \sqrt{r}\cos\frac{\theta}{2}\sin\theta\right] \tag{50}$$

(the linear terms are not related to the near-tip fields and are represented through the linear completeness of the EFG approximant). This basis can be used in Eq. (4) and leads to approximations of the form

$$u^h(\mathbf{x}) = \sum_{I=1}^{n} \underbrace{\mathbf{p}^T(\mathbf{x})\mathbf{A}^{-1}(\mathbf{x})\mathbf{C}_I(\mathbf{x})}_{\phi_I(\mathbf{x})} u_I \,. \tag{51}$$

where $\phi_I(\mathbf{x})$ is the enriched EFG shape function.

In contrast to the extrinsic methods presented in Sections 5.1 and 5.2, this method involves no additional unknowns. However, because of the increased size of the basis, additional computational effort is required to invert the moment matrix, $\mathbf{A}(\mathbf{x})$. In addition, the domain of influence must be enlarged to achieve regularity of $\mathbf{A}(\mathbf{x})$. For multiple cracks, four additional terms would have to be added to the basis for each crack; a method for coupling an enriched basis with a linear basis is presented in Section 5.4 which avoids this difficulty.

Using an enriched basis can lead to a moment matrix which exhibits some ill-conditioning. While this generally does not affect the final solution when the enriched basis is used globally, it does have a deleterious effect when trying to couple shape functions from an enriched basis to shape functions from another basis such as a linear basis. A treatment which has been found to be effective for dealing with ill-conditioning is to reduce the number of computations required to compute the shape functions by the procedure in Section 2.1. This procedure replaces the full inversion of the moment matrix with only a forward reduction and back substitution. A second method found to be effective for dealing with ill-conditioning is to diagonalize the

moment matrix by Gram-Schmidt orthogonalization (Lu, Belytschko, and Gu, 1994), which increases the linear independence of the moment equations.

When an enriched basis is used at any node of a mesh, it must be used at all nodes or a special technique must be used to blend it to nodes with a different basis. Simply deleting functions from the basis results in discontinuities in the approximation.

5.3.2 Radial enrichment

Meshless approximations can be partially enriched by expanding the intrinsic basis to include only the radial variation in Eq. (38). This leads to the basis

$$\mathbf{p}^T(\mathbf{x}) = \left[1, x, y, \sqrt{r}\right] \tag{52}$$

where r is the radial distance from the crack tip. This partial enrichment is feasible because the angular variation around the crack tip is smooth, but the radial variation is singular in the stress.

The advantage of partial enrichment is that the intrinsic basis is only expanded by one term and inverting the moment matrix, $\mathbf{A}(\mathbf{x})$, to form the shape functions is much cheaper than for full enrichment. In addition, it does not seem to be necessary to use the smoothing techniques in Chapter 4 because there are no discontinuities in the radial direction; the discontinuities in the angular direction lead to a noticeable loss of accuracy when full enrichment is used.

5.4 Coupling enriched and linear approximations

Enriching the approximation for the entire domain of a problem is generally unnecessary and leads to unneeded computational expense. For example, the crack-tip singular field is local to the crack tip with radius $\sim 0.1a$, where a is the length of the crack. Two techniques are presented here for coupling enriched and linear approximations, one which uses a consistent coupling to maintain C^0 continuity and one which does not.

The first technique involves coupling the approximation over a transition region as a linear combination of the enriched linear approximations (this is similar to the way Belytschko, Organ, and Krongauz (1995) coupled EFG to finite elements). The approximation is written

$$u^h(\mathbf{x}) = Ru^{enr}(\mathbf{x}) + (1 - R)u^{lin}(\mathbf{x}). \tag{53}$$

where $u^{enr}(\mathbf{x})$ is the enriched approximation and u^{lin} is the linear approximation; R is a ramp function which is equal to unity on the enriched boundary of the coupling

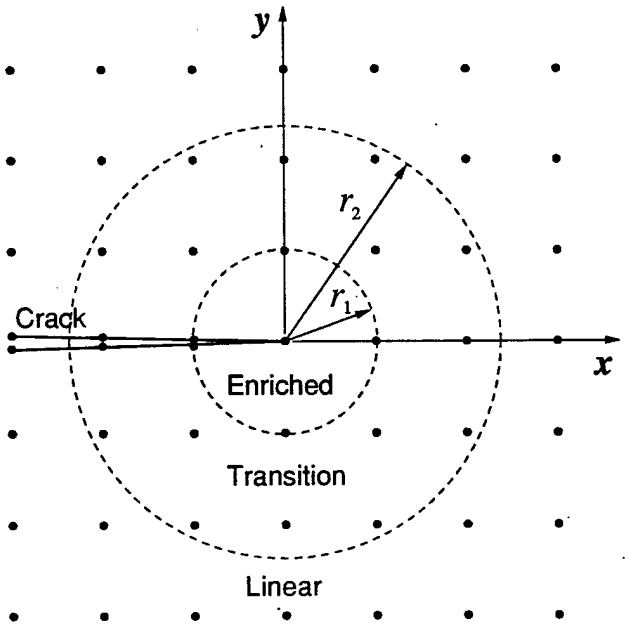

Figure 32: Schematic for the coupling of enriched and linear approximations.

region ($r = r_1$) and equal to zero on the linear boundary of the coupling region ($r = r_2$) (see Fig. 32). Some suggested polynomial ramp functions are

$$R = \begin{cases} 1 - \xi & \text{linear ramp} \\ 1 - 10\xi^3 + 15\xi^4 - 6\xi^5 & \text{quintic ramp} \end{cases} \tag{54}$$

where $\xi = (r - r_1)/(r_2 - r_1)$, r is the radial distance from the crack tip.

The coupled approximation for the intrinsically enriched basis from Section 5.3 is written

$$u^h(\mathbf{x}) = \sum_{I=1}^{n} \tilde{\phi}_I(\mathbf{x}) u_I \tag{55}$$

where

$$\tilde{\phi}_I(\mathbf{x}) = R\phi_I^{enr}(\mathbf{x}) + (1 - R)\phi_I^{lin}(\mathbf{x}). \tag{56}$$

and $\phi_I^{enr}(\mathbf{x})$ is the shape function formed from the enriched basis of Eq. (50) and $\phi_I^{lin}(\mathbf{x})$ is the shape function formed from a linear basis. This method ensures a compatible displacement field. The continuity in the strain field depends on the continuity of the ramp function, R (i.e., the linear ramp will yield continuous displacements, but

discontinuous strains at $r = r_1, r_2$; both displacements and strains will be continuous and smooth using the quintic ramp).

Through numerical experiments, it was found that the location of the inner radius of the ramp, r_1, is rather arbitrary and can actually begin at the crack tip. However, the outer radius, r_2, needs to be outside the singularity-dominated zone to obtain good accuracy.

It should be noted that it is possible to confine the enrichment to the crack tip region by simply changing from an enriched to a linear intrinsic basis away from the crack tip. The distance where the basis is changed should be outside the stress intensity factor dominated region, with an outer radius similar to the transition region described above. One drawback of this method is that the displacement field at the transition point will be C^{-1}, i.e., it will have a small jump in displacement. While this is theoretically not permissible in a Galerkin method, it is acceptable if the transition radius is sufficiently far from the crack tip so that jump is very small. In this case, the small jump will not have a noticeable effect on the solution.

These two methods of coupling the enriched and linear approximations were found to work better for the intrinsically enriched basis in Section 5.3 than for the extrinsic MLS enrichment in Section 5.1. The extrinsic MLS enrichment is sensitive to discontinuities and some loss of accuracy was noticed for this coupling.

Another method of localizing the enrichment to the crack tip region is to use extrinsic PUM enrichment from Section 5.2. The extrinsic basis can be added only to nodes near the crack tip region. However, it is necessary to enrich all nodes which contribute to the crack tip region or else the enrichment is incomplete and the solution is poor.

5.5 Mapping for kinked cracks

The enriched field of Eq. (38) predicts a discontinuity along $\theta = \pm\pi$. However, for kinked cracks, this discontinuity falls in the interior of the domain behind the crack tip. Therefore, a mapping is required to align this discontinuity in enriched field with the actual crack in the area behind the leading crack segment (i.e., the area to the left of the dotted line in Fig. 33). The mapping is designed so that a) the preceding segment of the crack is rotated to be aligned with the leading crack segment, b) the field along the line perpendicular to the leading segment (denoted by the dotted line) is not rotated, and c) the field between the two is rotated by a proportion of the angle α to θ_R.

We define an angle θ_R as the angle between the leading crack segment and the preceding segment, and α as the angle between the leading crack segment and a line from the kink (or rotation) point (x_{rot}, y_{rot}) to the point of interest (x, y). Let $\hat{\theta} = \alpha - \theta_R$ and $\bar{r} = \sqrt{(x - x_{rot})^2 + (y - y_{rot})^2}$. A new angle $\bar{\theta}$ is defined

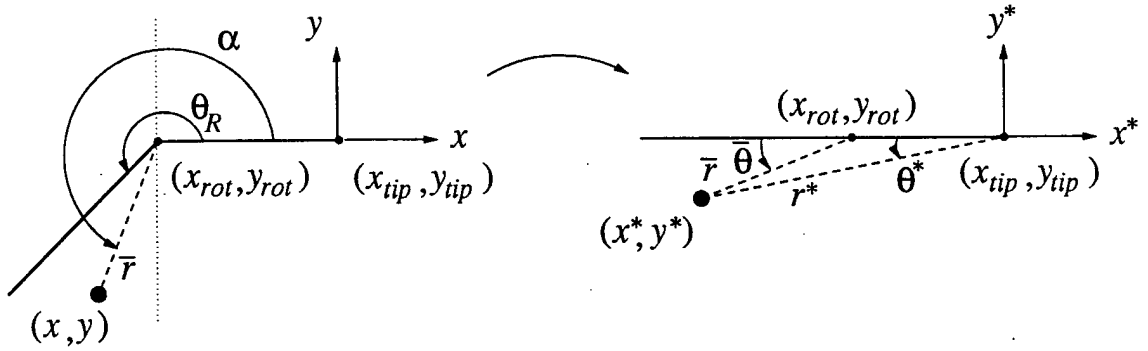

Figure 33: Coordinate mapping used for kinked cracks.

$$\bar{\theta} = \begin{cases} \dfrac{\hat{\theta}}{3\pi/2 - \theta_R}\,\dfrac{\pi}{2} = \hat{\theta}\, C_b & \hat{\theta} > 0 \\ \dfrac{\hat{\theta}}{\theta_R - \pi/2}\,\dfrac{\pi}{2} = \hat{\theta}\, C_a & \hat{\theta} < 0 \end{cases} \tag{57}$$

where

$$C_b = \frac{\pi/2}{3\pi/2 - \theta_R}$$

$$C_a = \frac{\pi/2}{\theta_R - \pi/2}$$

which is used to determine the coordinates of a point in the mapped coordinate system

$$x^* = x_{rot} - \bar{r}\cos\bar{\theta} - x_{tip} \tag{58a}$$

$$y^* = y_{rot} - \bar{r}\sin\bar{\theta} - y_{tip}\,. \tag{58b}$$

These coordinates are used to compute r^* and θ^* which are used in Eq. (38) or Eq. (50) to compute the enriched fields at (x, y). Note that the computation of strain involves derivatives with respect to (x^*, y^*) and it is necessary to obtain the derivatives with respect to the original crack tip coordinate system (x, y). The derivatives are obtained by the chain rule which leads to

$$\begin{bmatrix} \dfrac{\partial}{\partial x} \\ \dfrac{\partial}{\partial y} \end{bmatrix} = \begin{bmatrix} -\cos\bar{\theta}\cos\alpha - \sin\bar{\theta}\sin\alpha\, C_l & -\sin\bar{\theta}\cos\alpha + \cos\bar{\theta}\sin\alpha\, C_l \\ -\cos\bar{\theta}\sin\alpha + \sin\bar{\theta}\cos\alpha\, C_l & -\sin\bar{\theta}\sin\alpha - \cos\bar{\theta}\cos\alpha\, C_l \end{bmatrix} \begin{bmatrix} \dfrac{\partial}{\partial x^*} \\ \dfrac{\partial}{\partial y^*} \end{bmatrix} \tag{59}$$

where $C_l = C_a$ or C_b depending on the sign of $\hat{\theta}$ (see Eq. (57)).

5.6 Numerical Results for Enrichment

Several problems are solved to illustrate the effectiveness of enriching the EFG formulation for fracture problems. Solutions are given for single and mixed mode problems.

5.6.1 Near-tip crack problem

A closed form solution for a crack problem can be constructed by using the well-known near-tip field in a domain about the crack tip and prescribing the displacements along the boundary according to this field. This is called a patch test for singular fields. A square patch with sides of length $2a$ and a crack of length a is used (see Fig. 34). This problem is used to compare the performance of full enrichment (extrinsic and intrinsic), radial enrichment, and a linear basis. The displacement field for a mode 1 crack is (Williams, 1957)

$$u_x(\mathbf{x}) = \frac{k_1}{2\mu}\sqrt{\frac{r}{2\pi}}\cos\left(\frac{\theta}{2}\right)\left[\kappa - 1 + 2\sin^2\left(\frac{\theta}{2}\right)\right] \tag{60a}$$

$$u_y(\mathbf{x}) = \frac{k_1}{2\mu}\sqrt{\frac{r}{2\pi}}\sin\left(\frac{\theta}{2}\right)\left[\kappa + 1 - 2\cos^2\left(\frac{\theta}{2}\right)\right], \tag{60b}$$

where r is the distance from the crack tip and θ is the angle measured from the line of the crack (see Fig. 31). The stress intensity factor is prescribed as $k_1 = 1$ psi$\sqrt{\text{in.}}$ The stresses resulting from this displacement field satisfy equilibrium so the solution is exact if the displacements from Eqs. (60) are prescribed on the outer boundaries.

Without enrichment, the EFG method requires considerable nodal refinement near the crack tip to capture the singular stress field with sufficient accuracy to provide a useful computation of the stress intensity factor; the mesh used for comparison is shown in Fig. 34. A regular grid of nodes is used throughout the domain with a radial array of nodes around the crack tip for enhanced spatial resolution. The background finite element mesh used for quadrature of the Galerkin weak form is shown in Fig. 34c. The stress field ahead of the crack tip computed with a linear basis and the visibility criterion is shown in Fig. 35. Without the radial array of nodes around the crack tip, the singular stress is not adequately captured by regular EFG and the computed stress intensity factors are generally $5 - 15\%$ low (see Fig. 42). The radial array aids in capturing the singular stress field; however, the stresses are oscillatory in the radial direction (see Fig. 35) and in the angular direction (see Fig. 36). These oscillations are typical in approximating a singular field by a smooth function, but they lead to moderate domain dependence for the J integral.

Enriching the EFG trial function greatly aids in capturing the singular stress field around the crack tip; when full enrichment is used the oscillations are almost completely eliminated. The stress along $\theta = 0°$ from the crack tip computed with

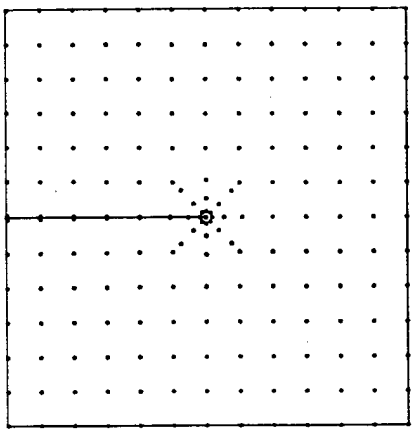

(a) Full mesh

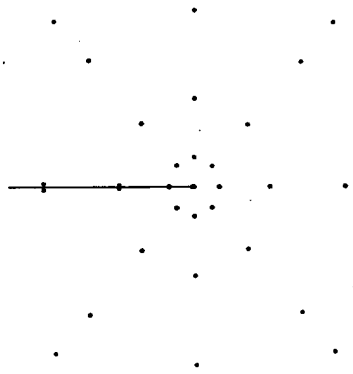

(b) Closeup at crack tip

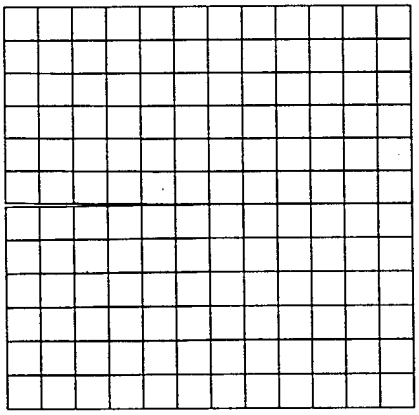

(c) Integration cells

Figure 34: Mesh used for near-tip crack problem without enrichment using rings at $r = 0.03a, 0.09a, 0.18a$.

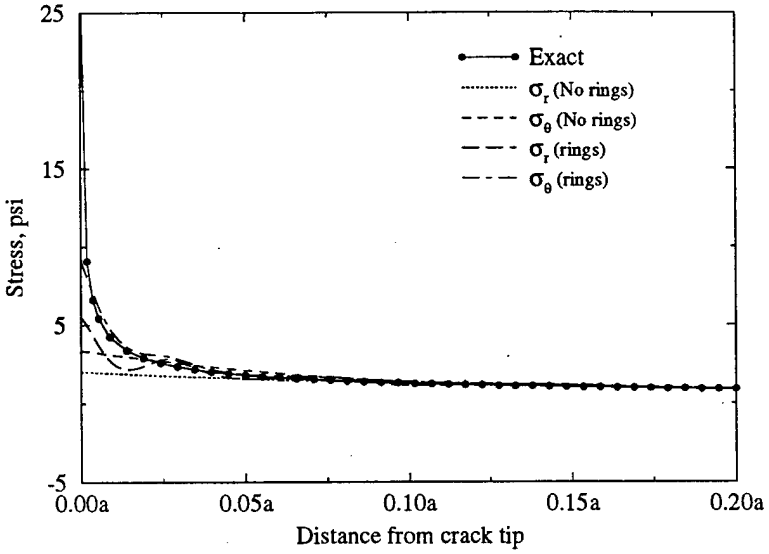

Figure 35: Stresses ahead of the crack tip ($\theta = 0, r > 0$) for the near-tip crack problem.

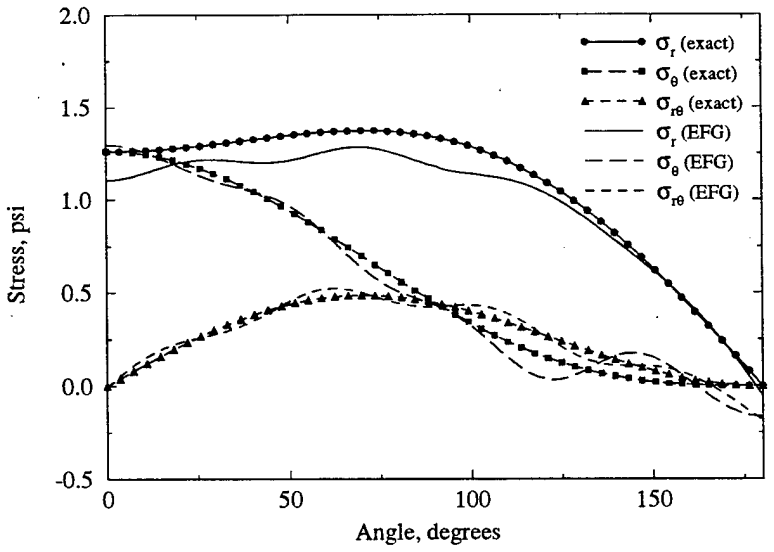

Figure 36: Angular variation in stress at a distance $r = 0.1a$ from the crack tip. Solution using linear basis with mesh shown in Fig. 34.

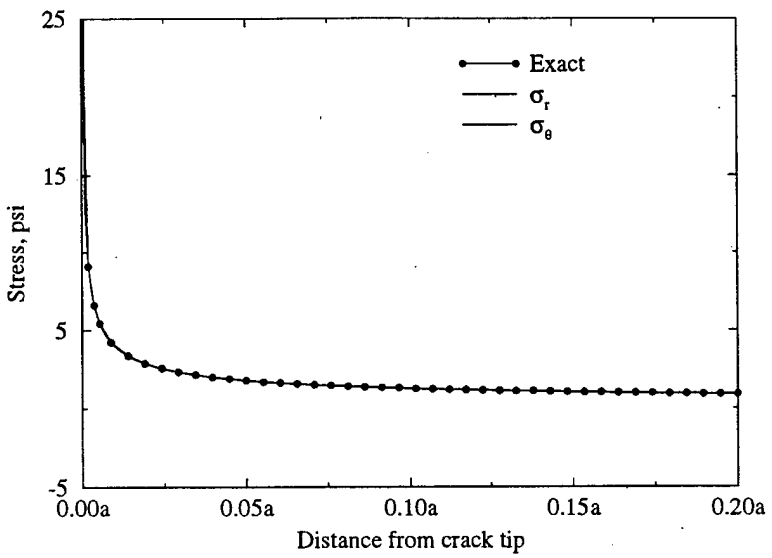

Figure 37: Stresses ahead of the crack tip for the near-tip crack problem with extrinsic MLS enrichment.

extrinsic MLS enrichment is shown in Fig. 37 and the angular variation of stress at $r = 0.1a$ from the crack tip, where a is the length of the crack, is shown in Fig. 38. These results were calculated using the background nodal arrangement shown in Fig. 34a without refinement at the crack tip. The diffraction method with $\lambda = 1$ (unless otherwise specified) is used with the enriched approximations to provide smooth and continuous shape functions near the crack tip. It can be seen that the enriched EFG method is able to capture the singularity and eliminate oscillations at the crack tip without using extra refinement in the crack tip region. The stress profiles for extrinsic and fully intrinsic enrichment are identical for this problem. Radial $\sqrt{r}$ enrichment of the intrinsic basis captures the singular stress much better than the linear basis with no extra nodes, but it tends to underestimate the stress field, as shown in Fig. 39.

The relative error in strain energy is shown in Fig. 40, and it can be seen that the enrichment greatly increases the absolute accuracy. For a linear basis, the slope of the line represents the rate of convergence of the approximation for uniform nodal refinement. For problems with a singularity, the rate of convergence is controlled by the order of the singularity for a polynomial basis of any order (Krysl and Belytschko, 1996; Strang and Fix, 1973). The rate of convergence for the linear basis in Fig. 40 is 0.58, which is just slightly higher than the theoretical value of 1/2. For the fully enriched approximations (extrinsic or intrinsic), the exact solution is contained in the

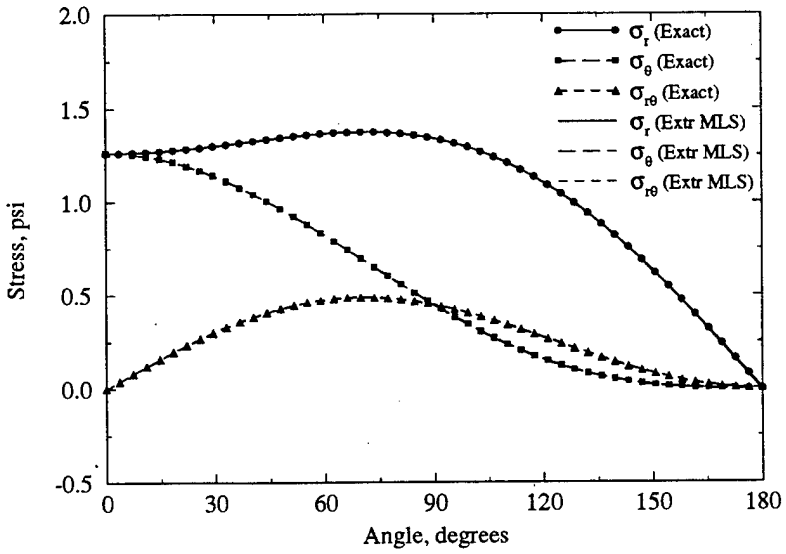

Figure 38: Angular variation of stress along constant radius ($r = 0.1a$) from the crack tip. Calculated using extrinsic MLS enrichment.

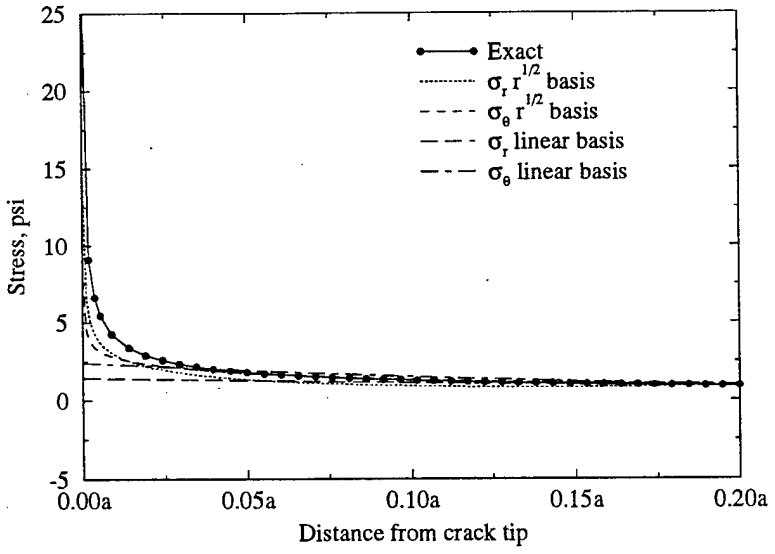

Figure 39: Stresses ahead of the crack tip ($\theta = 0, r > 0$) for the near-tip crack problem.

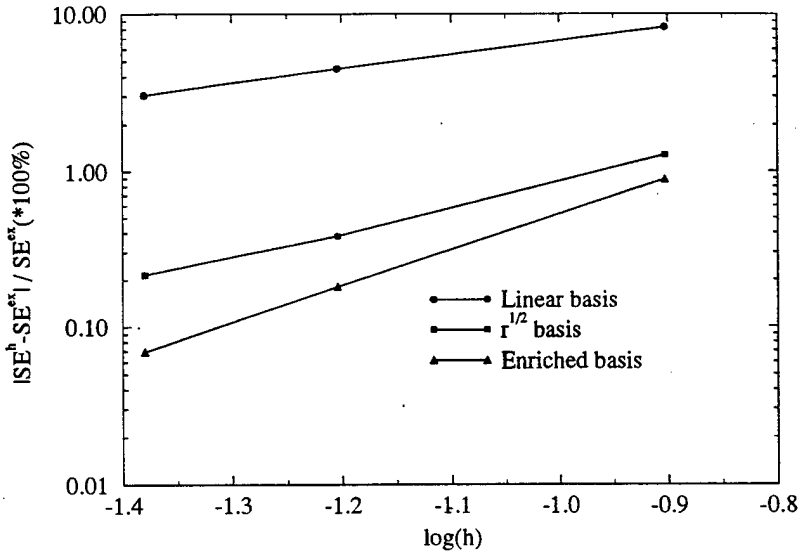

Figure 40: Convergence for near-tip crack problem. Diffraction method ($\lambda = 2$) used for enriched basis.

trial function and according to the theory of minimum potential energy, there should be no error due to approximation. In this case, the errors which arise are due to other effects, such as quadrature error and discretization of the essential boundary conditions.

Stress intensity factors were computed using the domain form of the J integral (Moran and Shih, 1987) with the domain shown in Fig. 41. The J integral is theoretically domain independent; however, oscillations such as those apparent in Figs. 35 and 36 and inaccuracy in the approximation of the singular crack-tip stress field as in Fig. 39 lead to some domain dependence. Enriching the EFG method yields domain independence by capturing the singularity and eliminating oscillations. Figs. 42 show stress intensity factors plotted against domain size for the J integral with enrichment by full and $\sqrt{r}$ enrichment versus EFG with a linear basis using nodal meshes of 9×9, 17×17 and 25×25 nodes. Full enrichment shows virtually no dependence on either domain size or number of nodes for this problem and for $\sqrt{r}$ enrichment, the stress intensity factor varies less than 3% for the coarsest mesh tested.

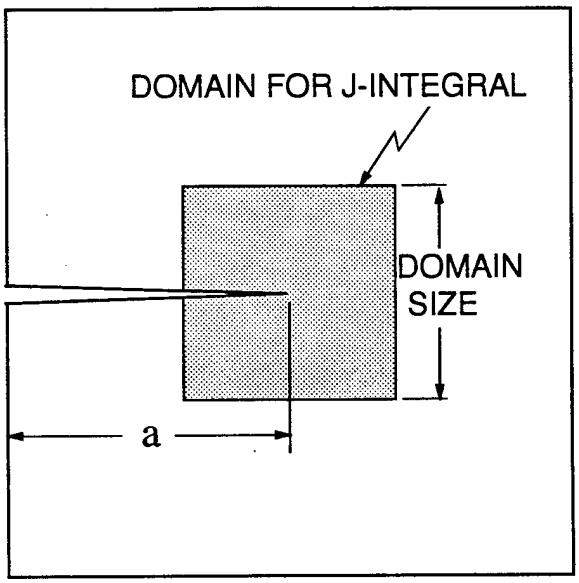

Figure 41: Domain used for evaluating domain form of J integral.

5.6.2 Shear edge crack

In this example, we consider a plate clamped on the bottom and subjected to shear traction $\tau = 1$ psi on the top and containing an edge crack of length $a = W/2 = 3.5$ in (see Fig. 43). The material constants used are $E = 30 \times 10^6$psi and $\nu = 0.25$ and plane strain conditions are assumed. The reference solution for the stress intensity factors is (Wilson, 1969)

$$k_1 = 34.0 \text{ psi}\sqrt{\text{in}}$$
$$k_2 = 4.55 \text{ psi}\sqrt{\text{in}}\,.$$

Stress intensity factors are computed by a mixed mode J integral formulation which uses the near crack tip fields as auxiliary fields; contour integrals in this method are converted to domain integrals using Gauss' theorem (Moran and Shih, 1987).

The EFG method has been shown to work well for this problem (Belytschko, Gu, and Lu, 1994), but a great deal of nodal refinement near the crack tip was required; in addition a large domain was needed for the J integral. The enriched EFG formulation for this problem gives results which are accurate and require much less computational expense. Table 1 gives results for a linear basis and enriched EFG using nodal grids of 57 (5×11) nodes and 324 (11×29) nodes, all evenly spaced. A domain of ± 1 in. from the crack tip is used for computing the J integral.

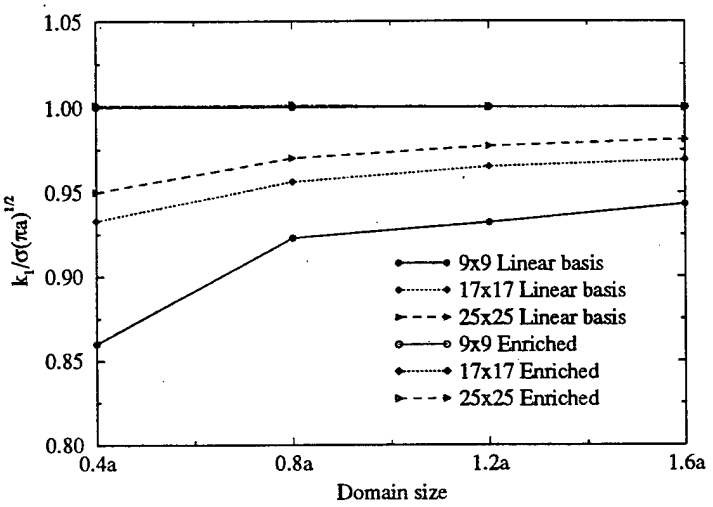

(a) Fully enriched EFG

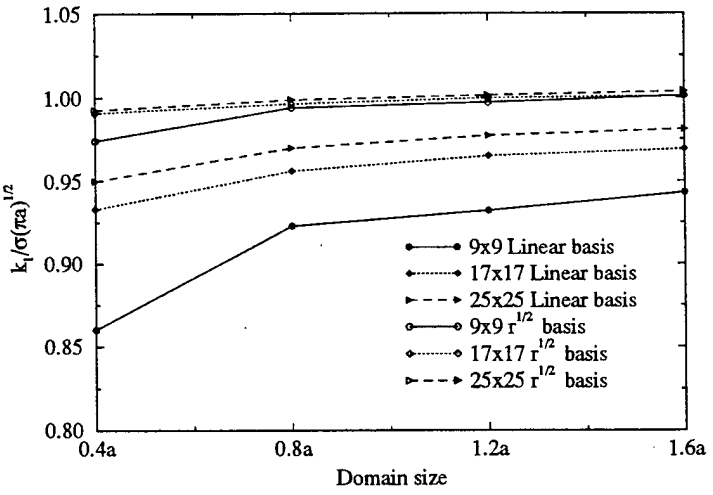

(b) $\sqrt{r}$ basis

Figure 42: Domain dependence of normalized stress intensity factor for linear basis and enriched EFG for the near-tip crack problem. Results are identical for full intrinsic and extrinsic enrichment.

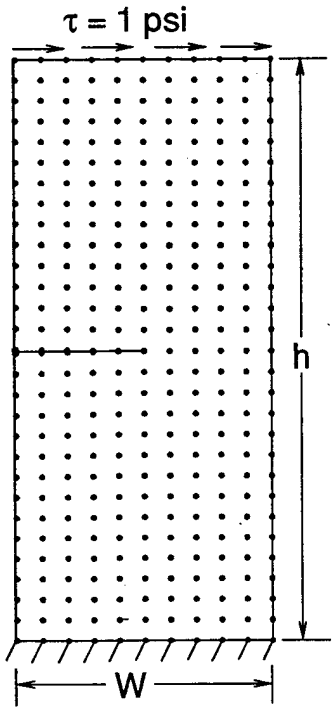

Figure 43: Geometry and nodal configuration for shear edge crack.

	Linear (no rings)		Extrinsic MLS		Intrinsic (Full)		Intrinsic ($\sqrt{r}$)	
nodes	k_1	k_2	k_1	k_2	k_1	k_2	k_1	k_2
5×11	26.90	3.43	34.43	4.58	32.24	4.21	31.86	4.20
11×29	32.51	4.33	34.21	4.55	33.87	4.54	33.01	4.59

Table 1: Stress intensity factors for shear edge crack calculated by linear basis and enriched EFG.

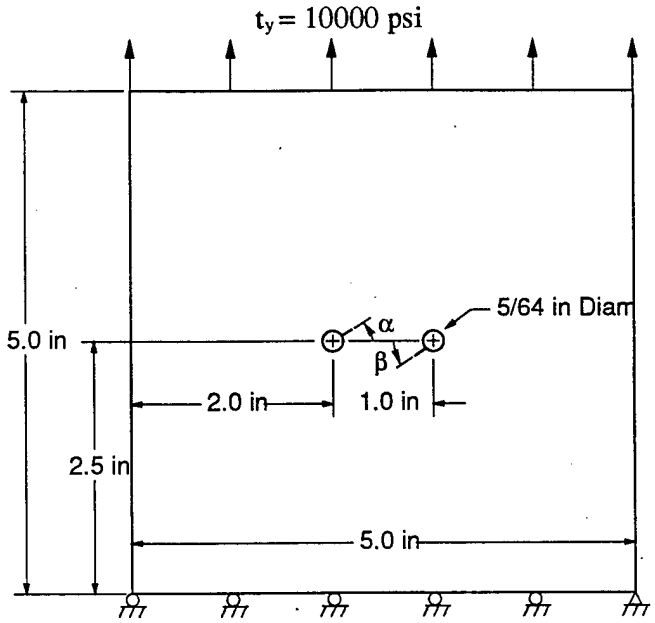

Figure 44: Schematic drawing of a tension-loaded plate with two holes and two fatigue cracks growing.

6 Numerical Results

6.1 Plate with 2 Holes and 2 Cracks

Fatigue crack growth from rivet holes is a common problem for structures made of thin, riveted sheets. For example, an aircraft fuselage is generally constructed of aluminum sheets which are riveted together at lap joints using thousands of rivets. The holes act as stress raisers to create a local stress concentration and small defects often develop in to cracks. Fig. 44 presents a simplified model of a plate with two holes subjected to a remote tension field. Initial cracks are assumed to emanate from each hole, with the left crack at an angle α and the right crack at an angle β as shown. Placing the cracks at an angle allows for the investigation of crack passing and crack bridging where the crack tips will actually avoid each other (Melin, 1983).

The first case shown is for $\alpha = \beta = 45°$. Figs. 45 shows Mises stress contours as the cracks are passing each other and after the cracks have passed. Before the cracks pass, there is significant load-bearing capacity in the region between the holes and up to the point where the cracks pass the crack tips are the area of highest stress. However, after the cracks pass, the region between the holes is severely weakened and the high stress area is shifted to the edge of the holes away from the cracks. This

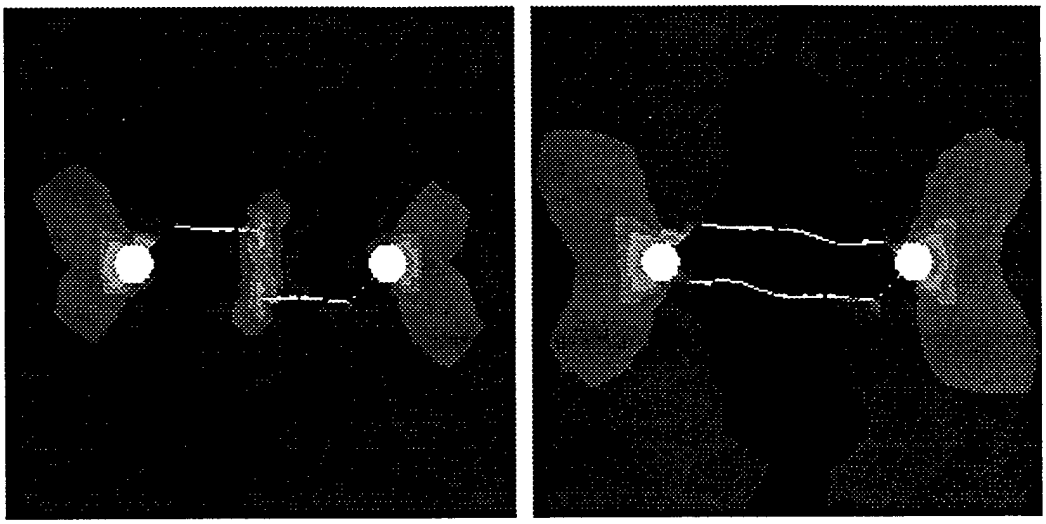

(a) step 8 (b) Step 16

Figure 45: Mises stress contours for a plate with two holes and two cracks growing. Initial cracks are at angles $\alpha = \beta = 45°$.

is further illustrated by the stress intensity factors in Fig. 46. For the first several steps of crack growth, the mode 1 stress intensity factors are increasing, but after the cracks pass the mode 1 stress intensity factors decrease. The mode 2 stress intensity factors are a measure of crack smoothness and curvature and it can be noted that as the cracks pass, they begin to curve and the mode 2 stress intensity factor deviates slightly from zero.

The next case shown is for $\alpha = 15°, \beta = 5°$. At this shallower angle the crack interaction is much more significant. Figs. 47 shows Mises stress contours at two stages of crack growth. These results show a similar trend as in the previous example where the crack propagation weakens the area between the holes to the point where it does not carry load any longer. It is interesting to note that even at this shallow angle the crack tips do not coalesce, but rather avoid each other only to curve around and meet each other behind the tip. This phenomena is known as crack bridging (Melin, 1983).

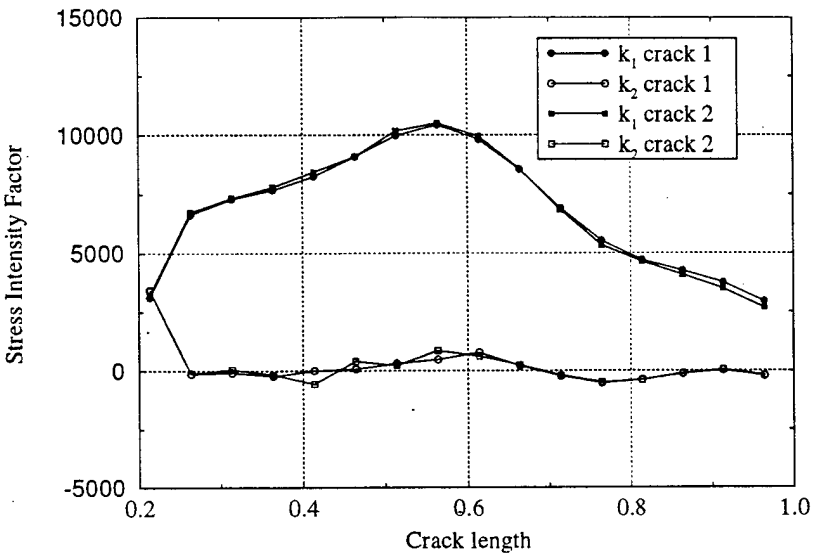

Figure 46: Stress intensity factors for plate with two holes and two cracks. Initial cracks are at angles $\alpha = 45°, \beta = -45°$.

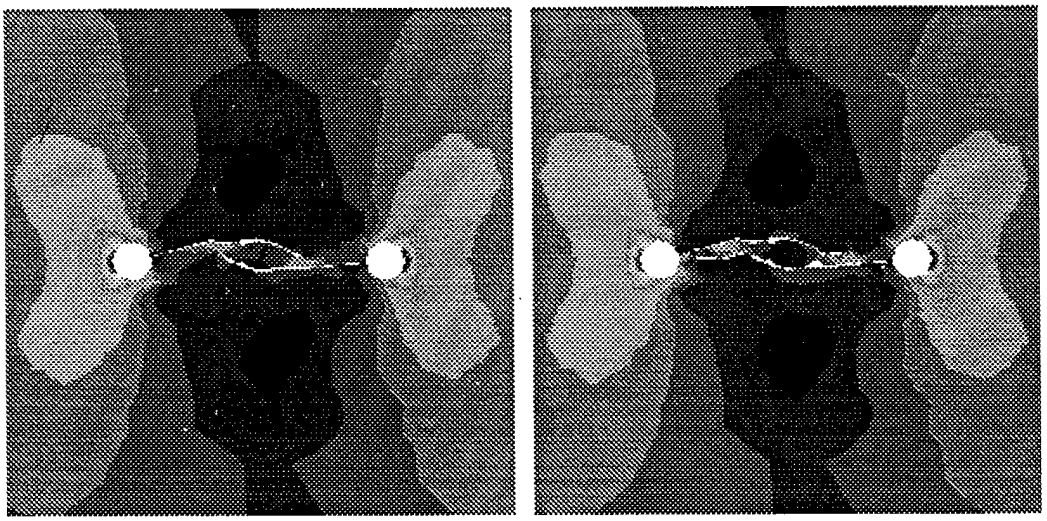

(a) step 7 (b) step 11

Figure 47: Mises stress contours for crack growth in a plate with two holes. Initial crack angles are $\alpha = 15°, \beta = 5°$.

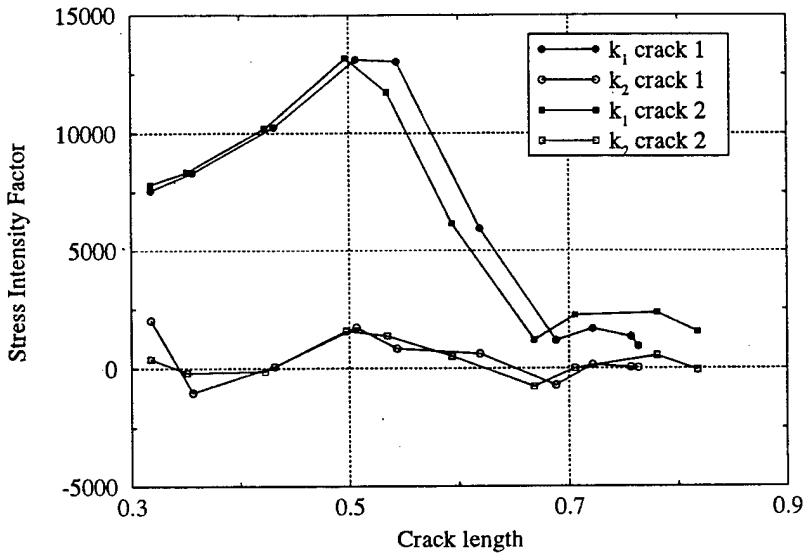

Figure 48: Stress intensity factors for two cracks growing in a plate with two holes. Initial crack angles are $\alpha = 15°, \beta = 5°$.

6.2 Double Cantilever Beam

In this example, a quasi-static crack is allowed to grow in a double cantilever beam (DCB) specimen. The geometry is shown in Fig. 49, with $L = 300$ mm, $h = 100$ mm, $a = 138$ mm, and $P = 100$ N. Plane stress linear elastic conditions are assumed with Young's modulus $E = 200$ GPa and Poisson's ratio $\nu = 0.3$.

In addition, a small perturbation is introduced at the crack tip consisting of a small kink at angle $d\theta$ relative to the direction of the long crack. The double cantilever beam exhibits crack path instability, meaning that the crack will curve away from the original straight path after a small perturbation. Physically, a perturbation may arise from an inclusion or other imperfection in the material or original crack geometry. Sumi, Nemat-Nasser, and Keer (1985) presented experimental results demonstrating the unstable nature of the crack path. Cotterell (1966) and Cotterell and Rice (1980) showed through perturbation techniques that the second term in the near-tip asymptotic expansion of stress, which is the non-singular stress parallel to the crack, can be used to identify the instability. Sumi, Nemat-Nasser, and Keer (1985) expanded this analysis to show situations of intermediate stability where either the path is initially stable and becomes unstable or else the path is initially unstable but becomes stable after some crack growth. Sumi (1985) performed numerical studies using finite ele-

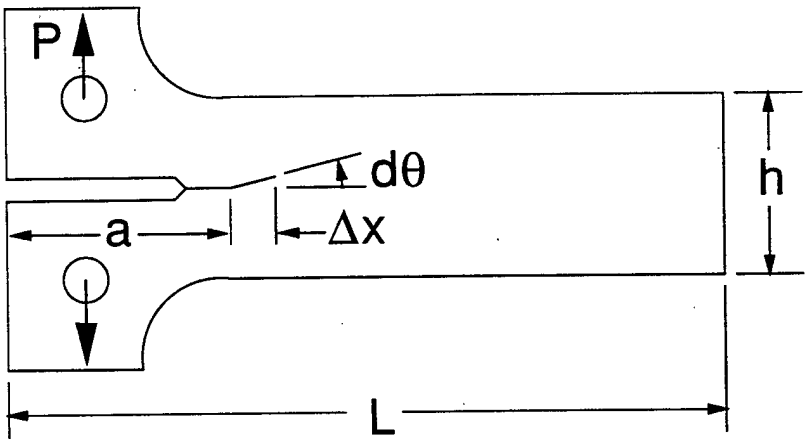

Figure 49: Initial geometry of double cantilever beam (DCB) specimen

ments and found that by using a small perturbation at the crack tip it was possible to simulate the experimental results; however, the crack path was incorporated in the initial mesh or treated by remeshing.

EFG results for three stages of crack growth are shown in Fig. 50 for a linear basis and in Fig. 50 for a linear $+\sqrt{r}$ basis. A perturbation of length $\Delta x = 12$ mm at an angle $d\theta = 4.8°$ is placed at the crack tip resulting in an unstable crack path which deviates from the original straight path and curves toward the boundary. A star-shaped array of nodes is placed at the crack tip for enhanced spatial resolution and the crack growth step is $\Delta a = 5$ mm. Figs. 51 and 52 show the effect of using a crack step size which is too large. The predicted path will contain significant error when the step size is not small enough to resolve the sharp change in the path. The stress intensity factors for the linear basis and linear + $\sqrt{r}$ basis are shown in Fig. 53 using a crack increment of $\Delta a = 5$ mm. The stress intensity factors for the two bases are quite similar, accounting for the similar crack path results shown in Figs. 50.

6.3 Crack Growth from a Fillet

This example shows the growth of a crack from a fillet in a structural member. The set-up to be modeled is shown in Fig. 54, with the actual domain modeled outlined with a dashed line. Sumi, Yang, and Wang (1995) performed experiments on a similar structure but also included the effects of welding residual stresses and varied the bending stiffness of the structure by varying the size of the bottom I-beam. The results presented here are for a simplified model in which the residual stresses due to welding are neglected. In addition, only the limiting cases for the bottom I-beam of

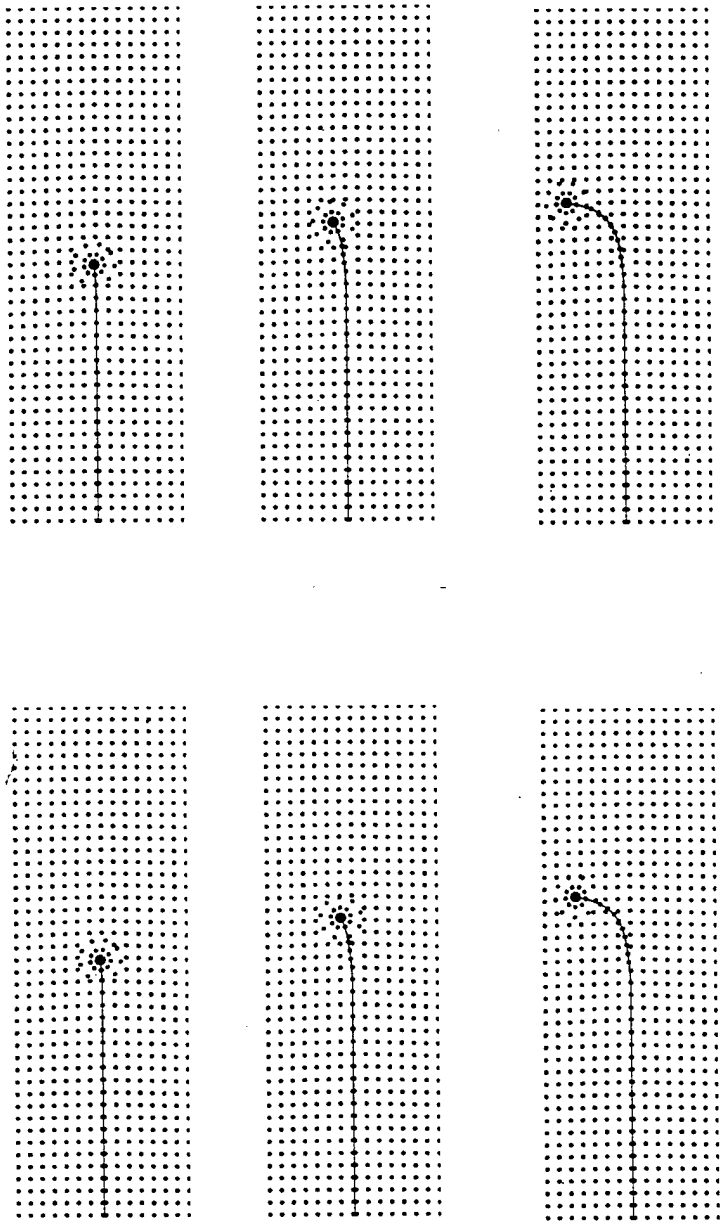

(a) Linear basis (b) $\sqrt{r}$ basis

Figure 50: Three steps of crack growth in a double cantilever beam (DCB) specimen using a *linear basis* and a *linear* $+\sqrt{r}$ *basis*. Crack growth increment is $\Delta a = 5$ mm.

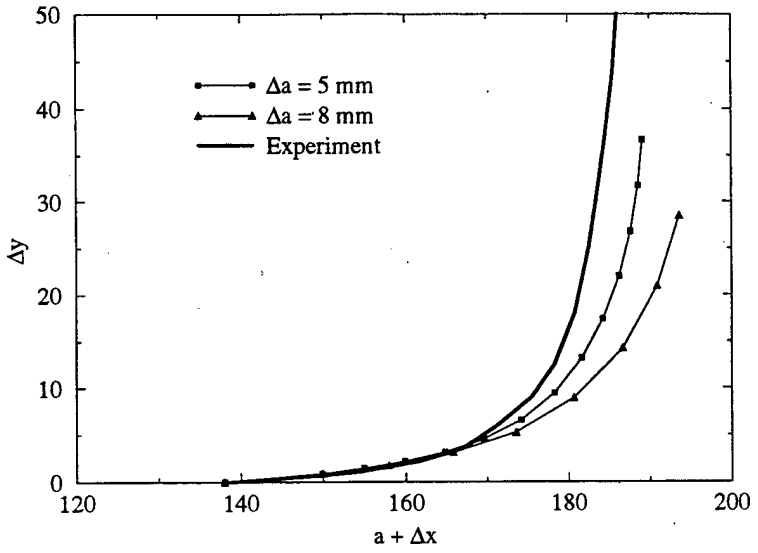

Figure 51: Crack path in double cantilever beam specimen for 2 growth step sizes using a linear basis.

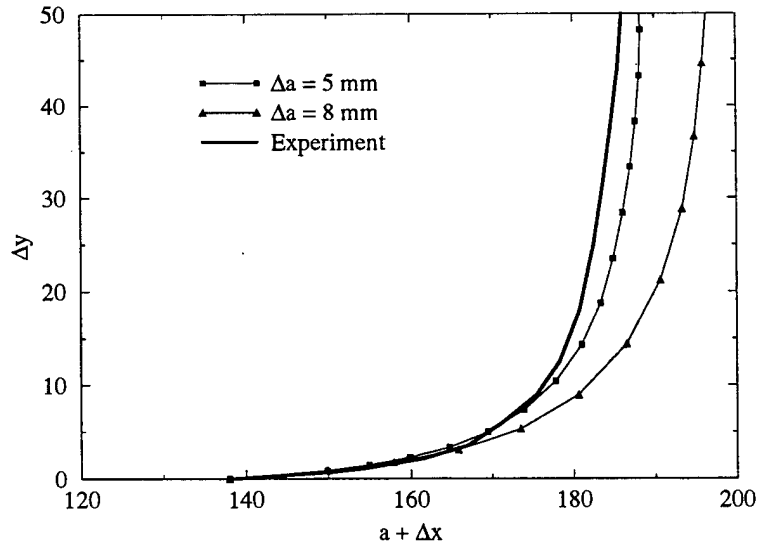

Figure 52: Crack path in double cantilever beam specimen for 2 growth step sizes using a linear $+\sqrt{r}$ basis.

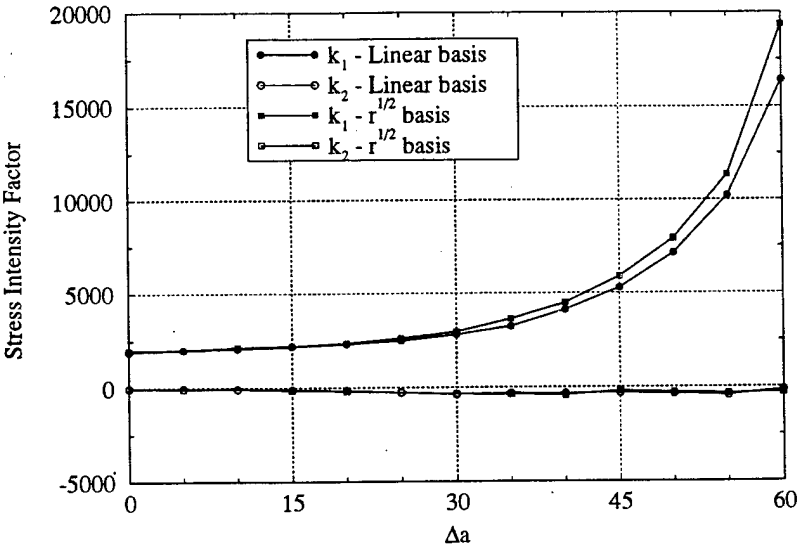

Figure 53: Stress intensity factors versus crack growth for linear basis and linear $+\sqrt{r}$ basis.

rigid (very thick beam) and flexible (very thin beam) are considered. The material is assumed to be plane strain linear elastic with Young's modulus and Poisson's ratio of $E = 200$ GPa and $\nu = 0.3$, respectively. The applied load is $P = 1.0$ N and the fillet radius is $\rho = 20$ mm. The initial crack length is $a_0 = 5$ mm. The EFG formulation is enriched using the enriched basis in the region surrounding the crack tip ($r_1 = 0, r_2 = 12$ mm) and the enriched fields are mapped using the procedure of Section 5.5.

The crack path evolution shown in Fig. 55 is for the case in which the supporting I-beam is very thin. In this case, the crack curves sharply downward and propagates toward the bottom of the structure. In contrast, when the structure is supported by a rigid I-beam, the crack will propagate almost directly toward the opposite fillet as shown in Fig. 56.

6.4 Beam Under 3-Point Bending

The next example is crack growth in a beam under 3-point bending. Three holes are located in a vertical line offset from the centerline and a crack is seeded at the bottom of the beam and allowed to grow (see Fig. 57). Bittencourt, Sousa, Wawrzynek, and Ingraffea (1995) presented experimental and numerical results for this problem which

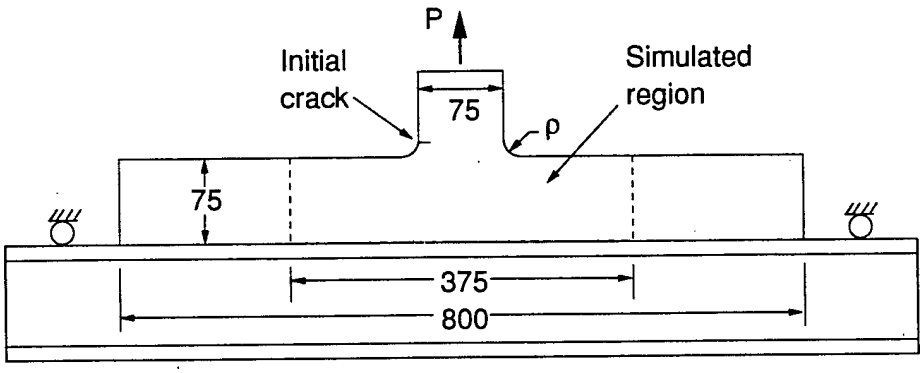

Figure 54: Experimental set-up from Sumi, et al. (1995).

Configuration	Crack length, a	Crack offset, b
Setup A	1.5	5.0
Setup B	1.0	6.0

Table 2: Crack configurations run for beam under 3-point bending.

showed that based on the location and length of the original crack, the path of crack growth would either intersect one of the holes or pass between them.

This problem is solved by the EFG method using a linear basis except for the crack tip region where the basis is locally enriched. The coupling procedure in Section 5.4 is used with $r_1 = 0.0001, r_2 = 0.5$. The locally enriched basis has the advantage of yielding accurate results for stress intensity factors without additional refinement at the crack tip. The presence of the holes makes this a useful feature because the additional nodes would create difficulties if they fell inside the holes.

Table 2 gives the dimensions and location of the initial crack for the two cases run and Figs. 58 shows EFG results corresponding to these two cases. For the first case solved, the crack passed between the bottom two holes and then passed very close to the middle hole on the opposite side. Experimental results showed that the crack actually curved into the hole; however, this effect was not captured numerically by either EFG or by the finite elements with remeshing as shown in Fig. 59. For the second setup, the crack was moved farther from the centerline and shortened. Results showed that the crack grew directly toward the center hole for this case.

6.5 Plate with 31 Holes

The examples presented to this point have been for relatively simple geometries. To demonstrate the power and flexibility of EFG, a problem with a more compli-

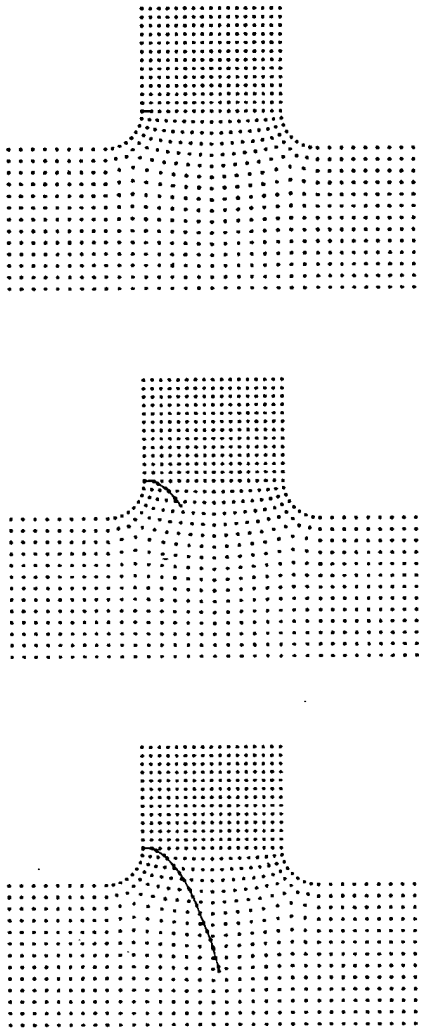

Figure 55: Crack path progression from a fillet for the case of a thin I-beam. Crack tip field enriched by enriched basis for $r = 0 - 12$ mm.

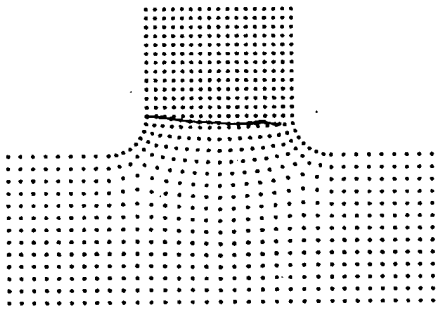

Figure 56: Crack path from a fillet for the case of a rigid I-beam. Crack tip field enriched by enriched basis for $r = 0 - 12$ mm.

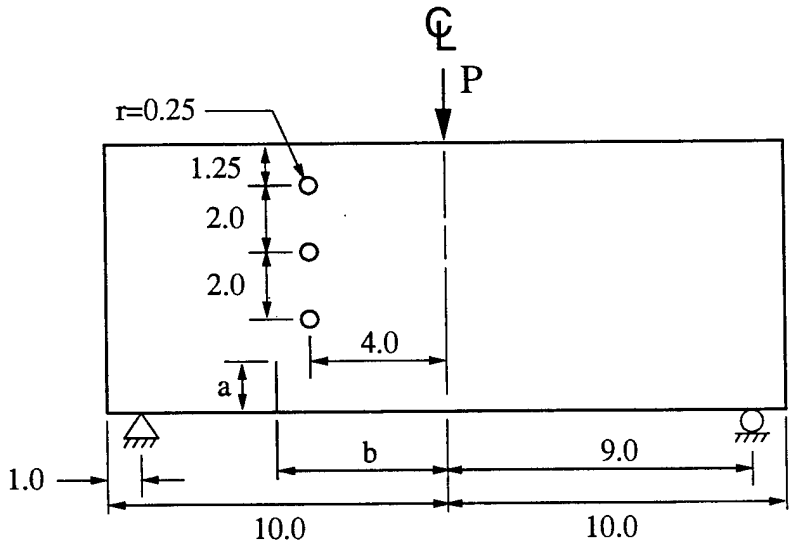

Figure 57: Schematic drawing of beam with three holes subjected to 3-point bending.

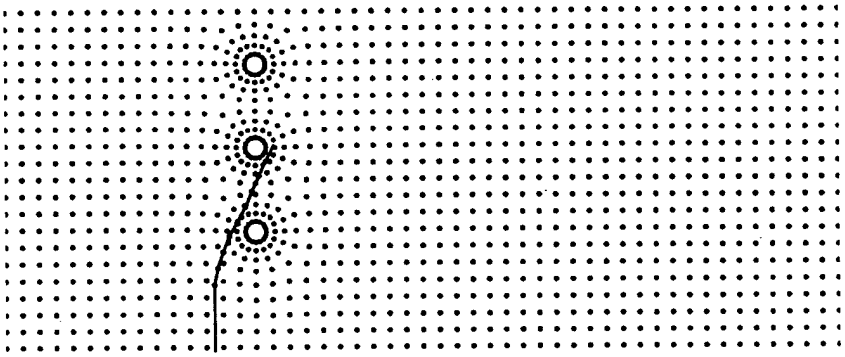

(a) Setup A

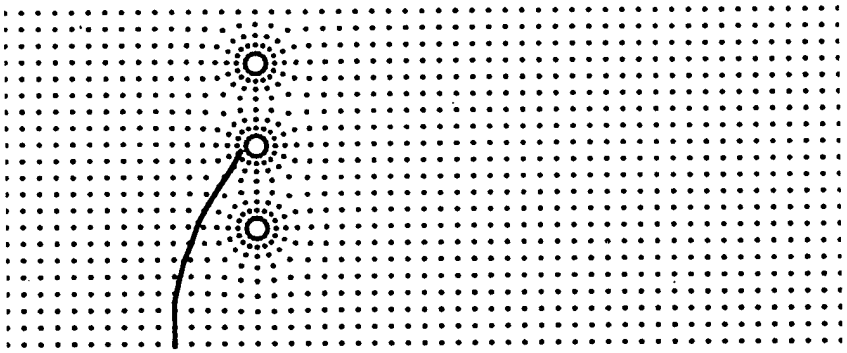

(b) Setup B

Figure 58: Final crack growth results for two different initial crack configurations.

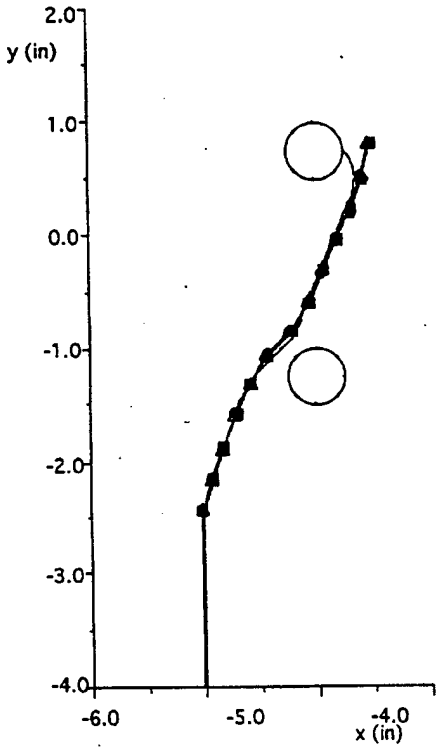

Figure 59: Experimental and numerical results from Bittencourt, Sousa, Wawrzynek, and Ingraffea (1995) for setup A.

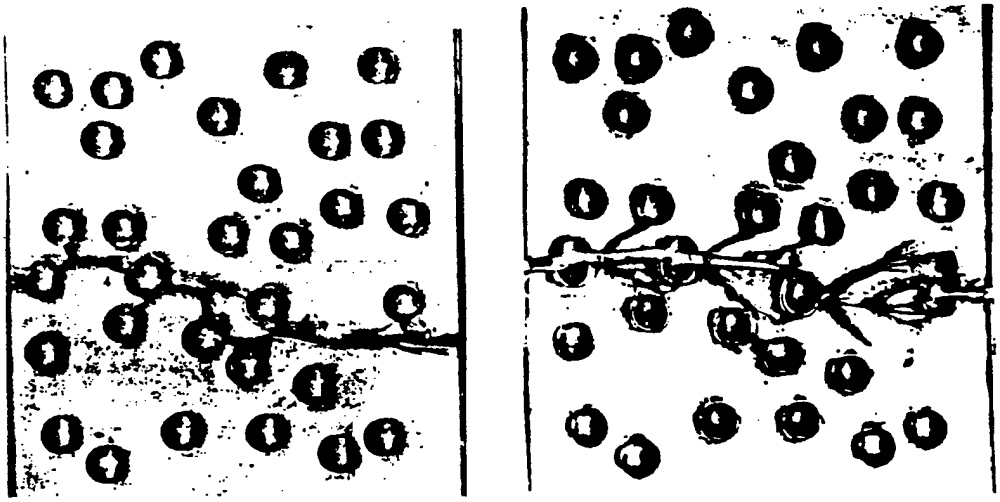

Figure 60: Two experimental specimens for crack propagation in a plate with 31 randomly spaced holes from Al-Ostaz and Jasiuk (1995).

cated geometry is solved. Consider a specimen with thirty-one holes randomly spaced throughout the domain. Crack growth in such a specimen is quite challenging and several of the enhancements for meshless methods are useful for solving this problem.

Al-Ostaz and Jasiuk (1995) presented experimental results for brittle fracture propagation in specimens with this geometry. The cracks began at the edge of holes and tended to intersect the holes directly until the whole specimen had fractured (see Figs. 60). They also performed finite element studies with a fine mesh in which fracture was simulated by the removal of elements. Whenever the strain energy or the maximum principal stress in an element reached a critical value, the element was deleted from the mesh, thereby extending the crack.

This problem was modeled by EFG using an initial nodal distribution of 2396 nodes. A stress analysis was performed with no cracks in order to determine where the highest stresses were. Small cracks were seeded at the seven highest stress locations. The bottom edge was fixed and a constant displacement was applied in the vertical direction to the top surface. The displacement along the top surface was incremented each step by 0.02% each step. The enriched basis from Eq. (50) was used in the region surrounding each crack and was ramped to a linear basis. The enriched basis was chosen over increased spatial refinement because of the complex geometry.

Results following 12 steps of crack growth are shown in Fig. 62. After a few steps of growth, a few dominant cracks developed and the other cracks arrested. Some cracks grew into other holes, but in general the cracks seemed to deflect away

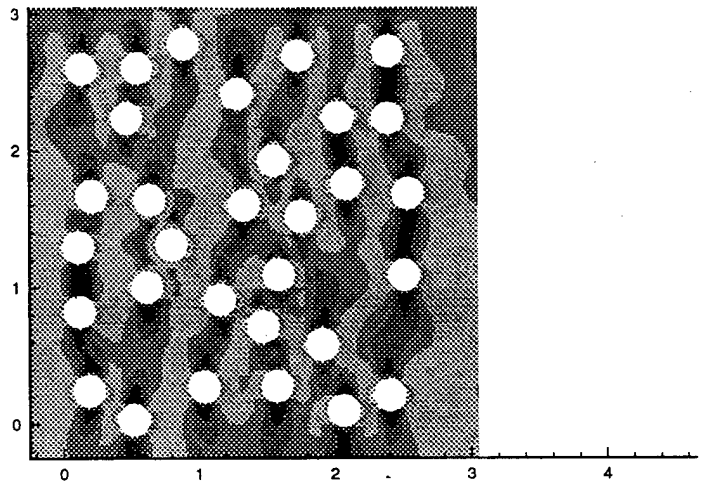

Figure 61: Mises stress contours for stress analysis without cracks for plate with 31 randomly spaced holes. Cracks are seeded at the seven highest stress locations.

from the holes. This result is in contrast to the experimental and numerical results of Al-Ostaz and Jasiuk (1995) who found that the crack tended to grow directly into the holes. Possible explanations of the differences with the experiments and the EFG computations is dynamic effects. The crack speed in the experiments was quite high (the specimens fractured completely in less than 1/3000 sec) while the EFG computations assumed quasi-static crack propagation. The cracking patterns obtained by EFG use the principles of fracture mechanics, whereas the finite element cracking pattern was predicted by the area of high stress.

7 Conclusions

A meshless method called the element-free Galerkin (EFG) method has been presented as a computational tool for simulating fatigue and quasi-static crack propagation. EFG approximations are formed from a basis, polynomial or enriched, and a set of unknown coefficients. A moving least squares (MLS) method is used to determine the unknown coefficients by minimizing a weighted $\mathcal{L}_2$ norm written in terms of nodal coefficients. The $\mathcal{L}_2$ norm in multiplied by a weight function with compact support, resulting in a local approximation, i.e., the approximation is written in terms of the

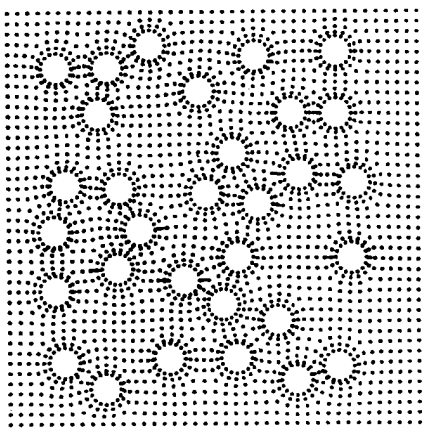

(a) Initial setup

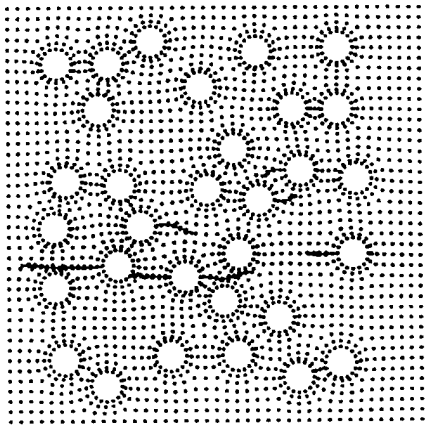

(b) After 12 steps

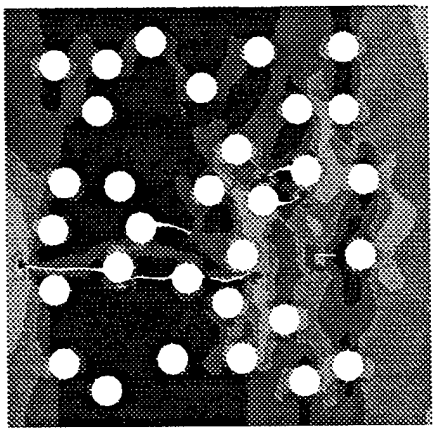

(c) Mises stress contours

Figure 62: Quasi-static crack propagation in plate with 31 randomly spaced holes.

surrounding nodes so the discrete equations are sparse. A weight function is defined at each node and common support shapes are circles and squares. A crack is modeled as a line segment in the interior of the domain. When a domain of influence of a node near the crack intersects the crack, it is truncated along the crack surface. Crack growth is modeled by adding an additional segment at the tip.

Smoothing methods for meshless approximations near nonconvex boundaries are presented. Boundaries in meshless methods are enforced by truncating the domains of influence of the nodal weight functions along the boundary. For nonconvex boundaries, this leads to discontinuities which extend into the domain. For the case of a crack, the weight function of a node near the crack tip will be discontinuous along the ray from the node which grazes the crack tip. Because the shape functions consist of the contributions of several weight functions, all shape functions near the crack tip will contain discontinuities along this line. These discontinuities are dealt with in several ways. The first is to simply ignore them and use the discontinuous approximations. The second technique is to use the diffraction method in which nodal domains of influence for nodes near a crack tip or other nonconvex boundary are wrapped around the boundary similar to the way in which light diffracts. A third method, called the transparency method, is developed only for cracks. In this method, the domains of influence for nodes near the crack tip are not severed at the crack tip, but are truncated gradually until at a short distance behind the tip they are truncated completely. Another method for obtaining continuous approximations is called the "see-through" method or the continuous line criterion. According to this criterion, if a continuous line can be drawn between two points without leaving the domain of influence, then the weight function is not modified. This method works well for smooth boundaries, such as holes, for refined nodal discretizations, but is not recommended for sharp boundaries such as cracks.

Techniques for enriching meshless approximations for linear elastic fracture are presented. Enrichment can be used when the form of the solution is known; this information may be used to form better approximations yielding better solutions with fewer degrees of freedom. The enrichment is carried out in two basic ways, extrinsically and intrinsically. Extrinsic enrichment involves adding the form of the solution to the EFG approximations constructed from a standard polynomial basis. Within extrinsic enrichment, extrinsic MLS enrichment and extrinsic PU enrichment are presented. Extrinsic MLS enrichment consists of adding the enrichment functions to the approximation which is used in the MLS methodology. Extrinsic PU enrichment consists of using the EFG shape functions as partitions of unity (hence the term PU) and adding the enrichment terms in an extrinsic basis which is multiplied by the partition of unity and some unknown nodal coefficients. The other form of enrichment, which is called intrinsic basis enrichment, consists of expanding the existing polynomial basis to include the terms from the asymptotic near tip solution. Both

full and partial enrichment are presented. Full enrichment adds the complete span of the near tip displacement field to the intrinsic basis, while partial enrichment adds only the $\sqrt{r}$ radial dependence to the basis. Computing enriched approximations is more expensive and is unnecessary away from a crack tip. To this end, a consistent coupling procedure is defined which allows enriched approximations to be used near a crack tip and then blended with the approximations from a linear basis. The coupling is defined such that consistency is maintained and no discontinuities arise in the displacement field. When the crack is kinked, a transformation is defined which will map the enriched fields to coincide with the actual crack path. This modification is required because the enriched field includes a discontinuity at $\theta = \pm\pi$ which does not coincide with the required discontinuity beyond the kink.

The element-free Galerkin method is shown to be an effective method for solving solid mechanics problems. The method is easily able to handle arbitrary crack propagation.

References

Akin, J. E. (1976). The generation of elements with singularities. *International Journal for Numerical Methods in Engineering 10*, 1249–1259.

Al-Ostaz, A. and I. Jasiuk (1995). Damage initiation and propagation in an elastic-brittle material with randomly distributed holes. In *1995 Winter Annual Meeting*. ASME.

Anderson, T. L. (1991). *Fracture Mechanics: Fundamentals and Applications* (First ed.). CRC Press.

Attaway, S. W., M. W. Heinstein, and J. W. Swegle (1994). Coupling of smooth particle hydrodynamics with the finite element method. *Nuclear Engineering and Design 150*, 199–205.

Banks-Sills, L. and Y. Bortman (1984). Reappraisal of the quarter-point quadrilateral element in linear elastic fracture mechanics. *International Journal of Fracture 25*, 169–180.

Barsoum, R. P. (1977). Triangular quarter-point elements as elastic and perfectly-plastic crack tip elements. *International Journal for Numerical Methods in Engineering 11*, 85–98.

Beissel, S. and T. Belytschko (1996). Nodal integration of the element-free Galerkin method. *Computer Methods in Applied Mechanics and Engineering 139*.

Belytschko, T., L. Gu, and Y. Y. Lu (1994). Fracture and crack growth by element-free Galerkin methods. *Modelling Simul. Mater. Sci. Eng. 2*, 519–534.

Belytschko, T., Y. Krongauz, M. Fleming, D. J. Organ, and W. K. Liu (1996). Smoothing and accelerated computations in the element free Galerkin method. *Journal of Computational and Applied Mathematics 74*, 111–126.

Belytschko, T., Y. Krongauz, D. Organ, M. Fleming, and P. Krysl (1996). Meshless methods: An overview and recent developments. *Computer Methods in Applied Mechanics and Engineering 139*, 3–47.

Belytschko, T., Y. Y. Lu, and L. Gu (1994). Element-free Galerkin methods. *International Journal for Numerical Methods in Engineering 37*, 229–256.

Belytschko, T., Y. Y. Lu, L. Gu, and M. Tabbara (1995). Element-free Galerkin methods for static and dynamic fracture. *International Journal of Solids and Structures 32*, 2547–2570.

Belytschko, T., D. Organ, and Y. Krongauz (1995). A coupled finite element–element-free Galerkin method. *Computational Mechanics 17*, 186–195.

Benzley, S. E. (1974). Representation of singularities with isoparametric finite elements. *International Journal for Numerical Methods in Engineering 8*, 537–545.

Bittencourt, T. N., J. L. Sousa, P. A. Wawrzynek, and A. R. Ingraffea (1995). Quasi-automatic simulation of crack propagation for 2D LEFM problems. *Engineering Fracture Mechanics*.

Cordes, L. W. and B. Moran (1996). Treatment of material discontinuity in the element-free Galerkin method. *Computer Methods in Applied Mechanics and Engineering 139*.

Cotterell, B. (1966). Notes on the paths and stability of cracks. *International Journal of Fracture Mechanics 2*, 526–533.

Cotterell, B. and J. R. Rice (1980). Slightly curved or kinked cracks. *International Journal of Fracture Mechanics 16*, 155–169.

Duarte, C. A. and J. T. Oden (1996a). *H-p* clouds — an *hp* meshless method. *Numerical Methods for Partial Differential Equations*, 1–34.

Duarte, C. A. M. and J. T. Oden (1996b). An *hp* adaptive method using clouds. *Computer Methods in Applied Mechanics and Engineering*. To appear.

Fleming, M., Y. Chu, B. Moran, and T. Belytschko (1997). Enriched element-free Galerkin methods for crack tip fields. *International Journal for Numerical Methods in Engineering 40*, 1483–1504.

Gallego, R. and J. Dominguez (1992). Dynamic crack propagation analysis by moving singular boundary elements. *ASME, Journal of Applied Mechanics 59*, S158–S162.

Gifford, Jr., L. N. and P. D. Hilton (1978). Stress intensity factors by enriched finite elements. *Engineering Fracture Mechanics 10*, 485–496.

Gingold, R. A. and J. J. Monaghan (1982). Kernel estimates as a basis for general particle methods in hydrodynamics. *Journal of Computational Physics 46*, 429–453.

Hegen, D. (1997). *An element-free Galerkin method for crack propagation in brittle materials*. Ph. D. thesis, Eindhoven University of Technology.

Henshell, R. D. and K. G. Shaw (1975). Crack tip finite elements are unnecessary. *International Journal for Numerical Methods in Engineering 9*, 495–507.

Hughes, T. J. R. (1987). *The Finite Element Method*. Englewood Cliffs, New Jersey: Prentice-Hall.

Krongauz, Y. and T. Belytschko (1996). Enforcement of essential boundary conditions in meshless approximations using finite elements. *Computer Methods in Applied Mechanics and Engineering 131*, 133–145.

Krongauz, Y. and T. Belytschko (1997a). Consistent pseudo-derivatives in meshless methods. *Computer Methods in Applied Mechanics and Engineering*. Accepted.

Krongauz, Y. and T. Belytschko (1997b). EFG approximation with discontinuous derivatives. *International Journal for Numerical Methods in Engineering*. Accepted.

Krysl, P. and T. Belytschko (1996). Element-free Galerkin: Convergence of the continuous and discontinuous shape functions. *Computer Methods in Applied Mechanics and Engineering*. Submitted.

Lancaster, P. and K. Salkauskas (1981). Surfaces generated by moving least squares methods. *Mathematics of Computation 37*, 141–158.

Libersky, L. D. and A. G. Petschek (1991). Smoothed particle hydrodynamics with strength of materials. In H. Trease, J. Fritts, and W. Crowley (Eds.), *The Next Free Lagrange Conference*, pp. 248–257.

Liszka, T. and J. Orkisz (1980). The finite difference method at arbitrary irregular grids and its application in applied mechanics. *Computers and Structures 11*, 83–95.

Liu, W. K., S. Jun, and Y. F. Zhang (1995). Reproducing kernel particle methods. *International Journal for Numerical Methods in Engineering 20*, 1081–1106.

Liu, W. K., S. Li, and T. Belytschko (1996). Moving least square reproducing kernel methods (I) methodology and convergence. *Computer Methods in Applied Mechanics and Engineering*. accepted.

Lu, Y. Y., T. Belytschko, and L. Gu (1994). A new implementation of the element free Galerkin method. *Computer Methods in Applied Mechanics and Engineering 113*, 397–414.

Lu, Y. Y., T. Belytschko, and M. Tabbara (1995). Element-free Galerkin methods for wave propagation and dynamic fracture. *Computer Methods in Applied Mechanics and Engineering 126*, 131–153.

Lucy, L. B. (1977). A numerical approach to the testing of the fission hypothesis. *The Astronomical Journal 82*(12), 1013–1024.

Malluck, J. F. and W. W. King (1980). Fast fracture simulated by conventional finite elements: A comparison of two energy-release algorithms. In G. T. Hahn and M. F. Kanninen (Eds.), *Crack Arrest Methodology and Applications*, ASTM STP 711, pp. 38–53. American Society for Testing and Materials.

Melenk, J. M. and I. Babuška (1996). The partition of unity finite element method: Basic theory and applications. *Computer Methods in Applied Mechanics and Engineering*.

Melin, S. (1983). Why do cracks avoid each other? *International Journal of Fracture 23*, 37–45.

Monaghan, J. J. (1982). Why particle methods work. *SIAM Journal of Scientific and Statistical Computing 3*(4), 422–.

Moran, B. and C. F. Shih (1987). Crack tip and associated domain integrals from momentum and energy balance. *Engineering Fracture Mechanics 27*(6), 615–641.

Nayroles, B., G. Touzot, and P. Villon (1992). Generalizing the finite element method: diffuse approximation and diffuse elements. *Computational Mechanics 10*, 307–318.

Oñate, E., S. Idelsohn, O. C. Zienkiewicz, R. L. Taylor, and C. Sacco (1996). A stabilized finite point method for analysis of fluid mechanics problems. Submitted.

Organ, D. J. (1996). *Numerical Solutions to Dynamic Fracture Problems Using the Element-Free Galerkin Method.* Ph. D. thesis, Northwestern University.

Organ, D. J., M. Fleming, and T. Belytschko (1996). Continuous meshless approximations for nonconvex bodies by diffraction and transparency. *Computational Mechanics 18*, 225–235.

Schlangen, E. and J. G. M. Mier (1992). Experimental and numerical analysis of micromechanisms of fracture of cement-based composites. *Cement & Concrete Composites 14*, 105–118.

Sedgewick, R. (1988). *Algorithms* (2nd ed.)., pp. 349–351. Reading, MA: Addison-Wesley Publishing Company.

Strang, G. and G. Fix (1973). *An Analysis of the Finite Element Method.* Englewood Cliffs, N.J.: Prentice-Hall.

Sulsky, D., S. J. Zhou, and H. L. Schreyer (1995). Application of a particle-in-cell method to solid mechanics. *Comput. Phys. Comm. 87*, 236–252.

Sumi, Y. (1985). Computational crack path prediction. *Theoretical and applied fracture mechanics 4*, 149–156.

Sumi, Y., S. Nemat-Nasser, and L. M. Keer (1985). On crack path stability in a finite body. *Engineering Fracture Mechanics 22*, 759–771.

Sumi, Y., C. Yang, and Z. N. Wang (1995). Morphological aspects of fatigue crack propagation part ii - effects of stress biaxiality and welding residual stress. Submitted.

Swegle, J. W., D. L. Hicks, and S. W. Attaway (1995). Smoothed particle hydrodynamics stability analysis. *Journal of Computational Physics 116*, 123–134.

Swenson, D. V. and A. R. Ingraffea (1988). Modeling mixed-mode dynamic crack propagation using finite elements: Theory and applications. *Computational Mechanics 3*, 381–397.

Terry, T. G. (1994). Fatigue crack propagation modeling using the element free Galerkin method. Master's thesis, Northwestern University.

Timoshenko, S. P. and J. N. Goodier (1970). *Theory of Elasticity* (Third ed.). New York: McGraw Hill.

Williams, M. L. (1957). On the stress distribution at the base of a stationary crack. *Journal of Applied Mechanics 24*, 109–114.

Wilson, W. K. (1969). *Combined-Mode Fracture Mechanics.* Ph. D. thesis, University of Pittsburgh.